THE UNIVERSITY
of EDINBURGH

This thesis has been submitted in fulfilment of the requirements for a postgraduate degree (e.g. PhD, MPhil, DClinPsychol) at the University of Edinburgh. Please note the following terms and conditions of use:

This work is protected by copyright and other intellectual property rights, which are retained by the thesis author, unless otherwise stated.
A copy can be downloaded for personal non-commercial research or study, without prior permission or charge.
This thesis cannot be reproduced or quoted extensively from without first obtaining permission in writing from the author.
The content must not be changed in any way or sold commercially in any format or medium without the formal permission of the author.
When referring to this work, full bibliographic details including the author, title, awarding institution and date of the thesis must be given.

Microwave System Development for Wireless Communications and Liquid Level Determination Inside Metallic Pipes for Oil and Gas Wells

Konstantinos Kossenas

Supervised By: Symon K. Podilchak

Thesis submitted for the degree of Doctor of Philosophy

Institute for Digital Communications (IDCOM)
The School of Engineering
The University of Edinburgh

2022

Abstract

A classic wireless propagation system between a transmitter and a receiver is well defined in the literature. One propagation scenario not very well researched is within enclosed environments such as pipes, tunnels, or mines. To explore such topics, the research in this thesis examined the theoretical modelling, design, implementation, and test of two different RF/microwave systems for applications within oil and gas wells. In particular, one system developed communications within a circular metallic pipeline, and the other was the liquid level determination of the crude by considering electromagnetic propagation within coaxial pipelines. The transceivers for those systems were placed into conventional circular and coaxial metallic pipes prevalent within real-world oil and gas well systems. Project work collaborated with The Oil and Gas Innovation Centre (OGIC) and Innerpath Technologies Ltd., both situated within Aberdeen, UK.

An original feasibility study was first developed where the well was modelled as a circular aluminium pipe and then considered an overmoded pipeline when treated like a microwave waveguide for the communication system. This is not conventional as typical microwave waveguide systems try to ensure unimodal operation over the required frequency range. Regardless, pipe testing was completed by considering commercially available oil and gas well pipelines, and as the transceivers, half-wave dipoles operating at 2.5 GHz were employed. Due to this excitation technique and the enclosed environment, parameters such as the propagating mode, the directivity, and the realized effective gain of the antennas also needed to be studied for this scenario. This brought new findings to the antennas and propagation research communities. Additionally, a numerical transmission path loss (TPL) model was developed and verified using full-wave simulations and lab measurements. Sensory data, including temperature and pressure within the pipe, were then transmitted using N210 universal software radio peripheral (USRP) modems by National Instruments and coded using orthogonal frequency-division multiplexing (OFDM). Since this initial study was experimentally verified and successful, a more advanced transceiver and mechanical antenna housing was designed and measured, which is even more realistic for industrial oil and gas well pipelines. In particular, compact PCB-based end-fire antennas were designed for signal propagation within a circular pipeline considering corroded carbon steel. A specific link budget was also developed for this S-band transmission system and measured successfully using a 36 meter carbon steel pipeline, which could have been easily extended to more than 150 meters. Also, based on the measured system data, the receiver sensitivity was -77 dBm and 15 dB in terms of the signal-to-noise ratio (SNR). Additionally, some digitized images and live videos were successfully transmitted and monitored in real-time using the N210 USRP modems. The employed antenna and its protective RF-

mechanical housing were also designed to be positioned within a mandrel for protection from possible gaseous flow and the filling material within the pipeline. Such a system could be adopted for industry-standard oil and gas wells. In terms of the RF/microwave liquid level determination system, the position of the crude was determined by measuring the time delay between the original signal and the reflected one from the liquid layer positioned at the bottom of the well. To conform to standard pipeline dimensions, the propagating mode was selected as a superposition of the TE_{21} and the TE_{31} modes, which again is not standard. Theory, full-wave simulations, and measurements verified the wave velocity for the generator signal and the propagation within the guide. Then, the transmission signals were selected as Gaussian and rectangular pulses. A dedicated link budget was also developed for the 2.4 GHz microwave system and measured successfully in the lab using a carbon steel pipeline. Based on these initial experiments, the maximum investigation depth for the proposed system can be 250 meters when the stimulating power is 1 kW. All these electromagnetic transmission studies realizing antenna-driven propagation were supported by theory, full-wave simulations, as well as system-level measurements, which approached high levels of technical readiness.

Lay Summary

The history of the oil and gas industry reflects local and global political events, economic constraints, and the personal endeavours of individual petroleum geoscientists as much as it does the development of technologies and the underlying geology. Because of the importance of the oil and gas industry, many companies and researchers are studying and developing new communication and sensor technologies. The problems to be resolved are the real-time and continuous monitoring of the pipeline condition, seismic activity, any corrosion, possible gas leak detection, and other similar issues. The most widespread technologies dealing with these issues include the development of new wireless sensor networks for the internet of things and other applications. However, the systems in place today for sensory information collection and data exchange within an oil and gas pipelines, do not traditionally employ antennas, and, such antenna-driven systems do not exist. Additionally, the technologies for monitoring and determining the condition of fluids found in subsurface oil and gas wells is not modernized despite their importance. Their modernization of the liquid level determination could assist in the productivity of well operations and identify the well flow rate capacity, for example.

The existing literature for establishing radio frequency applications for oil and gas wells has not examined the complete microwave systems as were discussed in this thesis. In particular, this thesis includes studying the pipe's relevant properties, which confines the signal, the antenna selection, and the design to ensure directed propagation while integrating a housing for protection from oil and gas product flow. Moreover, it includes a complete system simulation, testing, and analysis while considering commercially sized pipelines, the adoption of the most modernized standard wireless communication protocols, the definition of the system limitations in terms of required transmit powers, and the field experimental testing at the industrial, scientific and medical frequency band.

These studies and experimental works can be a basis for the implementation of high-speed wireless for real-time communications methods and the modernization of the liquid level determination method for deployment inside oil and gas well pipelines at microwave frequencies.

Declaration of Originality

I hereby declare that the research conducted in this thesis and the thesis itself has been composed solely by myself at the Institute for Digital Communications in the School of Engineering, The University of Edinburgh. The thesis has not been submitted, either in whole or in part, in any previous application for a degree. Except where otherwise acknowledged, the work presented is entirely my own. The included publications are my own work, except where indicated in the thesis.

Konstantinos Kossenas
23 March 2022

Acknowledgments

First and foremost, I would like to thank my Ph.D. research supervisor Dr. Symon K. Podilchak, with whom help this research has been possible. Also, I would like to thank him because of his technical and mental support over all these years, especially during the pandemic. I would like to mention his kindness and positive attitude in life. I am sure that if there were more people like Symon, our world would be a better place.

As I am now at the end of my student life, I would like to thank my friends, with whom we have shared all these years, for every feeling of joy, excitement, frustration, fatigue, and relief they have given us. Above all, however, I want to thank them for their faith in me. I would like to give special thanks to Penny as we spent together all those years.

I would like to dedicate this thesis to Prof. Dimitrios Chrissoulidis, supervisor of my master's degree, as he made me love research work and he taught me its fundamentals, and I hope he will be proud of me.

Last but not least, I wholeheartedly thank my family for the universal support of my efforts and choices and the opportunities they have constantly provided my brother and me since we were kids.

Contents

Abstract i

Lay Summary iii

Declaration of Originality iv

Acknowledgments v

Table of Contents vi

List of Figures ix

List of Tables xii

List of Symbols xiv

Acronyms and Abbreviations xvii

1 Introduction 1
- 1.1 Brief Historical Overview . . . 1
- 1.2 Thesis Motivation and Main Contributions . . . 2
- 1.3 Safety Standards . . . 4
- 1.4 Thesis Overview . . . 5

2 Background 7
- 2.1 Communications within Oil and Gas Well Pipelines . . . 7
- 2.2 Liquid Level Determination Method for Oil and Gas Pipelines . . . 9
- 2.3 Communication Scenarios within Enclosed Environments . . . 11
- 2.4 Filling Material . . . 12
- 2.5 Technical Background . . . 14
  - 2.5.1 Radio Frequency Telecommunication Systems . . . 14
  - 2.5.2 Principals of Waveguides . . . 15
  - 2.5.3 Digital Transmission and Modulation . . . 20
- 2.6 Full-Wave EM Modelling . . . 21
  - 2.6.1 Antennas . . . 22
  - 2.6.2 Pipelines as Waveguides . . . 22
  - 2.6.3 Coaxial Waveguide Terminated by Liquid . . . 22
  - 2.6.4 Antenna Propagation into the Circular Waveguides . . . 23
  - 2.6.5 Mandrels . . . 25

2.7 Summary . . . 26

3 Wireless Propagation in a Metallic Pipe Using Half-Wave Dipoles 28
3.1 Introduction . . . 28
3.2 Circular Waveguide Theory Applied on the Inner Core of the Pipeline . 28
3.2.1 Inner Core Characteristics . . . 29
3.2.2 Mode Analysis and Conductor Losses . . . 29
3.2.3 Electric and Magnetic Field . . . 31
3.2.4 Power Flow . . . 33
3.3 Half-Wave Dipole into the Circular Pipe . . . 35
3.3.1 Operation in Free Space and into the Pipe . . . 36
3.3.2 Effective Directivity . . . 37
3.3.3 Propagated Mode and Power Flow . . . 39
3.3.4 Transmission Path Loss . . . 40
3.3.5 Impulse Response and Effective Gain . . . 43
3.4 Sensory Data Transmission Through the Pipe . . . 44
3.4.1 Structure of the System . . . 45
3.4.2 Sensory Data Transmission . . . 46
3.5 Summary . . . 47

4 Controlled Propagation within Oil and Gas Pipelines using Directive Antennas 48
4.1 Introduction . . . 48
4.2 Pipeline Selection and Characteristics . . . 50
4.2.1 Mode Analysis and Conductor Losses . . . 51
4.3 PCB Yagi-Uda Antenna into the Circular Waveguide . . . 53
4.3.1 Antenna Selection . . . 54
4.3.2 Power Flow, Path Loss, & Testing . . . 56
4.3.3 Directivity, Gain, & Impulse Response . . . 59
4.3.4 Gap Between the Pipe Sections . . . 61
4.3.5 Link Budget Analysis when Pipes A, B, & C are Combined . . . 61
4.4 PCB Yagi-Uda Antenna and Housing Placement . . . 62
4.4.1 Radome Housing . . . 63
4.4.2 Field Routing Within the Pipe . . . 64
4.4.3 Path Loss & Testing . . . 66
4.4.4 Effective Gain & Impulse Response . . . 68
4.5 Communication Testing . . . 69
4.5.1 PCB Yagi-Uda Antenna into the Circular Waveguide . . . 69
4.5.2 PCB Yagi-Uda Antenna into the Housing . . . 71
4.5.3 Minimum Power Level Studies for Maximum Range Estimation . 71
4.5.4 Experiments with Additive White Noise . . . 72
4.6 Summary . . . 72

5 Microwave Liquid Level Determination for Oil and Gas Pipelines 74
5.1 Introduction . . . 74
5.2 Pipeline System and Modeling . . . 75
5.2.1 Selected Pipeline Characteristics and Filling Material . . . 76

5.2.2 Mode Analysis & Conductor Losses & Group Velocity 77
5.2.3 Power Loss & Power Flow 82
5.3 Liquid Level Determination Considering the Dominant TEM Mode . . . 85
5.3.1 Testing System & the Liquid Properties 86
5.3.2 Travelling Time of the Signal & Link Budget Equation 87
5.4 Propagation Modeling 88
5.4.1 Antenna Selection and Radome Housing 89
5.4.2 Field Routing Within the Pipe 91
5.4.3 Impulse Response of the System & Antenna Effective Gain . . . 92
5.5 Liquid Level Determination Testing 93
5.5.1 Excited Signals, Calibrations, & the Reflectometry System 94
5.5.2 Experimental Results for Liquid Level Determination 96
5.5.3 Link Budget Analysis 99
5.6 Conclusion 101

6 Conclusions and Future Work **103**
6.1 Conclusions 103
6.1.1 Communications within Oil and Gas Well Pipelines 103
6.1.2 Liquid Level Determination Method for Oil and Gas Pipelines . . 104
6.2 Future Work 105
6.2.1 Communications within Oil and Gas Well Pipelines 105
6.2.2 Liquid Level Determination Method for Oil and Gas Pipelines . . 106

Appendix **107**

A List of Publications **107**
A.1 Journal Papers 107
A.2 Conference Papers 107

Bibliography **109**

List of Figures

1.1 Schematic of the coaxial metallic pipe with its inner core. 3

2.1 Example of metallic waveguides in an air-traffic control radar [54]. . . . 15
2.2 Rectangular Waveguide Structures and Geometry. 16
2.3 Circular Waveguide Structures and Geometry. 18
2.4 Coaxial Waveguide Structures & Geometry. 20
2.5 Constellation diagram for PSK with Gray coding. 21

3.1 Inner core radius, $r = 69.85$ mm and wall thickness, $t = 10$ mm. 29
3.2 Electromagnetic field plot of the TE_{11} mode. 31
3.3 Electromagnetic field plot of the TM_{01} mode. 31
3.4 Electromagnetic field plot of the TE_{21} mode. 31
3.5 Numerically calculated percentage power flow for each mode with respect to frequency. 33
3.6 Half-Wave dipole structure. 36
3.7 Cross-section of the circular aluminium pipe which is representative of an oil and gas well pipeline. 36
3.8 Simulated and measured reflection coefficient of the half-wave dipole when it is placed (a) in the free space and (b) into the pipe. 37
3.9 Simulated directivity of the half-wave dipole, operating at 2.5 GHz with respect to the radius of the circular waveguide. 38
3.10 Simulated directivity of the half-wave dipole, operating at 2.5 GHz versus length, for various circular waveguides radius. 38
3.11 Setup for the wireless system showing the cross-section of the circular aluminium pipe, which is representative of an oil and gas well pipeline. . 39
3.12 Electric field lines in the inner core. 40
3.13 Simulated power flow lines for the TE_{11} mode within the circular metallic waveguide. 40
3.14 Transmission path loss (TPL) model. 41
3.15 Effective gain of the transceivers based on the measured impulse response of the dipoles which were placed inside the aluminium pipe. 42
3.16 Measured impulse response of the dipoles which were placed inside the aluminium pipe in 700 mm distance. 42
3.17 Graphical user interface (GUI). 44
3.18 Flow diagram of transmission and reception system using OFDM and BPSK modulation schemes. 45
3.19 Experimental and block diagram setup of the channel. 46

3.20 Tabulated initial and final temperature and pressure data, which were transmitted through the pipe. 47

4.1 Full length of the inner core set up. 49
4.2 Attenuation constant of the TE_{11} mode as compared to different values for the relative permeability. 53
4.3 Microstrip based end-fire Yagi-Uda antenna structure. 54
4.4 Simulated and measured reflection coefficient of the PCB Yagi-Uda antenna. 55
4.5 Realized gain of the antenna as a function of the azimuthal angle. 56
4.6 Experimental and schematic setup where the Yagi-Uda antennas were placed at the edges inside the circular metallic pipe. 57
4.7 Measured S-Parameters for the system when the PCB Yagi-Uda antennas were placed inside the pipe sections. 58
4.8 Measured and numerically calculated TPL for the two PCB Yagi-Uda antenna transceiver systems when placed at the edge of each pipe section. 58
4.9 Simulated directivity for the PCB Yagi-Uda antenna, operating at 2.4 GHz in terms of the circular metallic waveguide radius. 59
4.10 Measured gain for the transmitter and the receiver antennas using the impulse response. 60
4.11 Time-domain impulse response of the system as described in Fig. 4.6. . 61
4.12 Aluminium mechanical housing 1-meter long (radome) of the antenna. . 62
4.13 Experimental and schematic setup where the Yagi-Uda antennas were placed into the housing. 63
4.14 Simulated power flows show the smooth injection through the sheet. . . 63
4.15 Electric field lines in the inner core, when the excitation occurs from the PCB Yagi-Uda antenna which is placed into the mechanical housing. . . 65
4.16 Simulated power flow lines within the circular metallic waveguide generated by the PCB Yagi-Uda antenna, placed into the mechanical housing. 65
4.17 Measured S-Parameters for the system when the PCB Yagi-Uda antennas of each mandrel were is joint on the edges of each pipe section. 66
4.18 Measured and numerically calculated TPL for the two PCB Yagi-Uda transceiver antennas of each mandrel where is joint the edges of each pipe section. 67
4.19 Time-domain impulse response of the system: Mandrel - Pipe A - Mandrel. 67
4.20 Measured gain for the transmitter and the receiver antennas into the mandrels using the impulse response. 68
4.21 Block diagram of the setup for the experimental testing of the propagation system. 70
4.22 Transmitting directly through the circular pipe to test the limitations of the system as it is illustrated in Fig. 4.21. 70
4.23 Block diagram of the setup for the experimental testing of the propagation system, including the mandrels. 71

5.1 System schematic and experimental test setup for proof-of-concept of the proposed microwave ranging system. 76
5.2 Attenuation constant of the TEM mode due to the conductivity of the metallic walls. 79

5.3 Simulated setup for liquid level determination considering single mode operation for the pipe. 86
5.4 Excited and reflected pulses by water, seawater, and oil. 87
5.5 Reflection coefficient (| S_{11} |) of the waveguide port when the three different liquids are considered. 88
5.6 PCB Yagi-Uda antenna placed into the housing (or radome) which is installed on the top of a 2 m carbon steel 1010 section. 89
5.7 Simulated longitudinal plane (y-z plane) of the electric field lines in the coaxial waveguide pipeline. 90
5.8 Simulated transverse plane (x-y plane) of the electric field lines in the coaxial waveguide pipeline. 90
5.9 Experimental setup for the measurement of the S - parameters reported in Fig. 5.10. 91
5.10 Measured S-Parameters for the system depicted in Fig. 5.9. 91
5.11 Measured impulse response of the end-to-end system (see Fig. 5.9). . . . 92
5.12 Measured gain for the transmitter and the receiver antennas using the impulse response. 93
5.13 Bench-top photograph of the experimental setup for the reflectometry studies. 94
5.14 Schematic of the developed reflectometry system (circuits and instrumentation). 94
5.15 Measurements of the transmitted Gaussian signal in the frequency domain. Spans: (a) 2.35 to 2.45 GHz and (b) 2.3997 to 2.4003 GHz. 96
5.16 Measurements of the transmitted rectangular pulse signal in the frequency domain. Spans: (a) 2.3 to 2.4 GHz and (b) 2.3999 to 2.4001 GHz. 97
5.17 Measurements of the transmitted and reflected signals for the reflectometry system. 98
5.18 The transmitted and reflected signal measurements for the proposed system as reported in Fig. 5.1a. 99
5.19 Reflection coefficient for the antenna and system as reported as is reported in Fig. 5.1a. 100

List of Tables

2.1 Comparison to the other oil & gas wells communication systems 9
2.2 Liquid level determination methods comparisons 11
2.3 CST Studio Suite EM Field simulations parameters about the antenna models 22
2.4 CST Studio Suite EM Field simulations parameters about the circular aluminium waveguide models. 23
2.5 CST Studio Suite EM Field simulations parameters about the circular carbon steel 1010 waveguide models. 23
2.6 CST Studio Suite EM Field simulations parameters about the coaxial aluminium waveguide models. 24
2.7 CST Studio Suite EM Field simulations parameters about the coaxial carbon steel 1010 waveguide models. 24
2.8 CST Studio Suite EM Field simulations parameters about the coaxial waveguide terminated by liquid model. 24
2.9 CST Studio Suite EM Field simulations parameters about the half-wave dipole when placed inside a circular aluminium waveguide model. 25
2.10 CST Studio Suite EM Field simulations parameters about the PCB Yagi-Uda antenna when placed inside a circular carbon steel 1010 waveguide model. 26
2.11 CST Studio Suite EM Field simulations parameters about the circular and coaxial mandrels when are terminated by waveguide port model. . . 26

3.1 Cut-off frequencies of the propagated TE & TM modes in GHz for the circular waveguide 30
3.2 Cut-off frequencies for the circular waveguide with radius 69.85 mm, until 3 GHz 32

4.1 Chemical composition of the AISI 1010 carbon steel [65] 50
4.2 Electromagnetic properties of ferrous ferric oxide 51
4.3 $r = 69.85$ mm, $\epsilon_r = 1$ 51
4.4 $r = 69.85$ mm, $\epsilon_r = 1.5$ 51
4.5 $r = 69.85$ mm, $\epsilon_r = 2$ 51
4.6 $r = 57.15$ mm, $\epsilon_r = 1$ 52
4.7 $r = 57.15$ mm, $\epsilon_r = 1.5$ 52
4.8 $r = 57.15$ mm, $\epsilon_r = 2$ 52
4.9 Conductor losses for the propagating modes of the circular waveguide . . 53

4.10 Transmission coefficient at 2.4 GHz for two antennas placed at either end of the corroded pipe 56
4.11 Extra loss due to controlled gaps between pipes A & B 61
4.12 Simulated transmission coefficient for determining the coupling into each mode at 2.4 GHz 64
4.13 Transmission coefficient (| S_{21} |) at 2.4 GHz for the antennas when each mandrel is joint the edges of each pipe section 66

5.1 r_1 = 136.525 mm, r_2 = 69.85 mm - ϵ_r = 1 79
5.2 r_1 = 122.2375 mm, r_2 = 57.15 mm - ϵ_r = 1 80
5.3 r_1 = 136.525 mm, r_2 = 69.85 mm - ϵ_r = 1.5 80
5.4 r_1 = 122.2375 mm, r_2 = 57.15 mm - ϵ_r = 1.5 81
5.5 r_1 = 136.525 mm, r_2 = 69.85 mm - ϵ_r = 2 81
5.6 r_1 = 122.2375 mm, r_2 = 57.15 mm - ϵ_r = 2 82
5.7 Group velocities for the possible modes of the selected coaxial waveguide 82
5.8 Electric properties of the testing liquid, as well as, the volume losses (L_{Liquid}). The reflection coefficient of the waveguide port is also reported 87
5.9 Simulated transmission coefficient (| S_{21} |) for determining the coupling into each mode at 2.4 GHz 89

List of Symbols

A	boundary condition constant/constant
B	boundary condition constant
b	waveguide dimension
C	boundary condition constant
D	boundary condition constant
c	speed of light
D	density
D	directivity
D_0	maximum directivity
d	distance/depth
$\mathbf{E}$	electric field vector
f_c	cutoff frequency
g	gravity
G	antenna gain
G_0	maximum antenna gain
G_{eff}	antenna effective gain
$G(x)$	Gaussian pulse function
G_{eff_r}	effective gain of the receiver antenna
G_{eff_t}	effective gain of the transmitter antenna
$\mathbf{H}$	magnetic field vector
$H_N(\omega)$	Fourier transform of the normalised impulse response
$h(t)$	normalised impulse response
j	imaginary unit
J_m	first kind Bessel function of order m
J'_m	derivative of first kind Bessel function of order m
$\mathbf{J}_s$	surface current
k	wavenumber
k_c	cutoff wavenumber of waveguide
L	waveguide length
L_{Liquid}	volume loss in liquid
L_{ref}	loss in the reflectrometer
m	integer constant
n	integer constant
$\mathbb{N}_0$	natural numbers including 0
$\mathbb{N}^\star$	natural numbers non-including 0
P	pressure

P	constant
P_0	power flow down a waveguide
P_ℓ	power loss per unit length
P_{Rx}	received power
P_{stim}	stimulated power
P_{Tx}	transmitted power
r	circular waveguide radius
R_s	characteristic resistance of the metal walls
$\mathbf{S}$	Poynting Vector
S	salinity
T	temperature
T	period
t	waveguide wall thickness
$\tan\delta$	loss tangent
V_0	voltage
x	axial coordinate in cylindrical coordinates
y	axial coordinate in cylindrical coordinates
Y_m	second kind Bessel function of order m
Y'_m	derivative of second kind Bessel function of order m
z	axial coordinate in Cartesian/cylindrical coordinates
Z_0	characteristic impedance of a coaxial line
Z_m	Bessel-Neumann combination function of order m
Z'_m	derivative Bessel-Neumann combination function of order m
α	waveguide dimension
$\boldsymbol{\alpha}$	attenuation constant
$\boldsymbol{\alpha}_c$	attenuation constant due to finite conductivity of the guide walls
$\boldsymbol{\alpha}_r$	attenuation constant due to rust
$\boldsymbol{\alpha}_s$	attenuation constant due to surface roughness
β	phase constant
Δt	time difference
ε	complex relative permittivity
ε'	real part of the complex relative permittivity
ε''	imaginary part of the complex relative permittivity
ϵ	electric permittivity
ϵ_0	free space electric permittivity $\left(\approx 8.854 \cdot 10^{-12}\mathrm{F/m}\right)$
ϵ_r	relative electric permittivity
ε_R	total radiation efficiency of an antenna
ζ	intrinsic impedance of the medium
η	intrinsic admittance of the medium
λ_0	free space wavelength
λ_c	cutoff wavelength
λ_g	wavelength
μ_0	free space magnetic permeability $\left(\approx 4\pi \cdot 10^{-7}\mathrm{H/m}\right)$
μ	magnetic permeability/mean of distribution
μ_r	relative magnetic permeability
ρ	axial distance in cylindrical coordinates

σ	electrical conductivity/standard deviation
v_g	group velocity
ϕ	azimuth in cylindrical coordinates
χ_{mn}	root of the Bessel Function/Bessel-Neumann combination function
χ'_{mn}	root of the derivative of the Bessel Function
ω	angular frequency

Acronyms and Abbreviations

4G	Fourth Generation
5G	Fifth Generation
Bandwidth	(BW)
Baseefa	British Approvals Service for Electrical Equipment in Flammable Atmospheres
BER	Bit Error Rate
BPSK	Binary Phase-Shift-Keying
CWT	Continuous Wave Telemetry
DC	Direct Current
EIRP	Effective Isotropic Radiated Power
EM	Electromagnetic
EMT	Electromagnetic Telemetry
Ex	Explosion Protected
FMCW	Frequency Modulated Continuous Waveform
HSE	Health and Safety Executive
IMU	Inertial Measurement Unit
IoT	Internet of Things
ISI	Inter-Symbol Interference
ISM	Industrial, Scientific and Medical frequency band
LNA	Low Noise Amplifier
MIMO	Multiple-Input Multiple-Output
MPT	Mud Pulse Telemetry
No.	Number
OBW	Occupied Bandwidth
OFDM	Orthogonal Frequency Division Multiplexing
OLSR	Optimized Link State Routing
PCB	Printed Circuit Board
PLE	Path Loss Exponent
PSK	Phase-Shift-Keying
PVT	Pressure - Volume - Temperature
QAM	Quadrature Amplitude Modulation
QPSK	Quadrature Phase-Shift-Keying
RF	Radio Frequency
SIW	Substrate Integrated Waveguide
SMA	SubMiniature version A
SNR	Signal to Noise Ratio
SL	System Losses

TEM	Transverse Electromagnetic Mode
TE_{mn}	mnth transverse electric mode
TM_{mn}	mnth transverse magnetic mode
TPL	Transmission Path Loss
UK	United Kingdom
USRP	Universal Software Radio Peripheral
VNA	Vector Network Analyzer
VPE	Vector Parabolic Equation

Chapter 1

Introduction

This introduction lays out a brief discussion of the history of oil and gas wells and the importance of human activity, which is the motivation for developing RF systems in this thesis. Also, it provides key points about the contribution of the work in the RF field. Then, the thesis structure and content are highlighted.

1.1 Brief Historical Overview

The people in the Far East were the first to drill wells, in around 2000 BC, using the cable tool percussion method to produce brine. A chisel on bamboo rods was lowered into the well on cables 1-4 cm thick and woven from Indian reed [1]. From the Iron Age until the 1850s, oil was limited, and oil was obtained almost exclusively from surface seeps and mines workings. The use of oil increased in the 1860s with new technologies in both production and refining.

The history of the European oil and gas industry reflects local and global political events, economic constraints, and the personal endeavours of individual petroleum geoscientists as much as it does the development of technologies and the underlying geology. In Britain, the first 'accidental' discovery of gas was made in 1875 in the Weald Basin which is south of London, England. Still, it was not until 1919 that Britain's first oil field was discovered at Hardstoft, in Derbyshire (North England), as a result of a government-funded exploration drilling campaign triggered by the need to find indigenous supplies of oil during World War I [2].

The 1914–18 and 1939–45 World Wars were significant drivers in the exploration for and exploitation of Europe's oil resources and the development of technologies to produce synthetic fuels from the liquefaction of bituminous coal; a process that generated a liquid from solid coal [3]. The combination of carbon monoxide and hydrogen as the Allied and Axis governments struggled to maintain adequate fuel supplies for their war efforts. That period played a disproportionately large role in developing the modern global oil and gas industry. Also, these drilling technologies further developed during Britain's first oil boom and the extrapolation of crude near the East Midlands oil fields and the Dutch gas fields.

All these activities led to the discovery of the vast oil and gas resources beneath the North Sea in the 1960s and 1970s, which enabled Britain, Norway, Denmark, and The Netherlands to be largely self-sufficient in oil and gas from the late 1970s until production began to decline rapidly in the early 2000s [2]. Currently, the world's deepest well is in Russia - OP-11 (12.345 km). The drilling of the world's deepest hole was completed in

January 2011 [1]. Also, OP-11 is in the Odoptu oilfield in Sakhalin and the horizontal length of the wellbore is 11.475 km.

All this massive progress in the oil and gas wells has resulted in the development of every technical aspect of this industry. In particular, little progress has been made for real-time monitoring of the drilling parameters and the condition for wells to maintain safe production and operations. Unique electromagnetic (EM) challenges can also arise when overcoming the environmental and geological conditions for critical high-speed data communications within oil and gas wells. For example, the transmission of real-time data on well health, crude output, liquid level determination, and potential seismic activity is essential for safe operations [4].

1.2 Thesis Motivation and Main Contributions

Many companies and researchers are studying and developing new technologies because of the importance of the oil and gas industry [4]–[30]. The problems to be resolved are the real-time and continuous monitoring of the pipeline condition, seismic activity, any corrosion, possible gas leak detection, and other similar issues. Additional relative problems concern the hydraulic horsepower required to lift fluid, the efficacy of packer placement (an isolation device placed into the wellbore), the overall monitoring of the changing reservoir conditions, and, the pressure-flow relations over the production life-cycle [7]. The most widespread technologies which are dealing with these issues include the development of new wireless sensor networks for the internet of things (IoT) and other applications [8]. However, there does not exist today a fully demonstrated RF system, driven by directive antennas, which was able to offer microwave propagation within an oil and gas pipeline.

One available medium, which has not been exploited previously, is the pipeline in the inside region, which acts like an enclosed metallic waveguide. This is in stark contrast to other modern wireless systems such as 4G, 5G, and Wi-Fi, where data communications are based on radiating antennas and free-space propagation [4]. This research work expands on these previous achievements. It focuses on RF/applying microwave technology to monitor data such as temperature, pressure, and digitized images and videos and determine the condition of fluids found in subsurface oil and gas wells. Two RF wireless systems considering propagation within a coaxial pipeline configuration and its enclosed circular (inner core) was developed to implement those technologies.

In the Fig. 1.1 the metallic pipe configurations are illustrated. In oil production wells it is often required to lower the fluid density by injecting gas down into the well via the annulus, this then enters the central production tubing via a gas lift valve and allows lifting of the heavier hydrocarbon fluid mixture. This arrangement conveniently lends itself to a coaxial pipe in pipe arrangement which is investigated for this study [31]. These pipe regions have been considered a wireless communication medium and treated as metallic circular (inner core) and coaxial waveguides. The transceivers are placed inside the pipeline under particular characteristics and conditions that introduce some practicalities that degrade the signal quality. This scenario makes for a challenging electromagnetic engineering problem, defining propagation within a multi-moded waveguide. The waveguide diameter is not chosen at the outset but instead selected

from commercially available standard pipes. This can help ensure better mechanical mating with the many available diameters typically used by the oil and gas industry. This contrasts with more conventional guided-wave or metallic waveguide configurations for high-power radar or satellite communication systems, for example, where the bandwidth (BW) of the dominant mode is typically employed to achieve unimodal propagation [32].

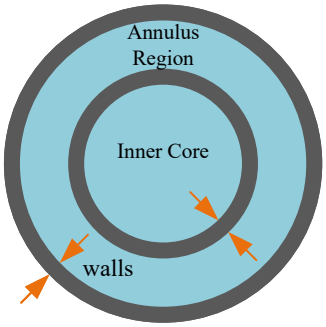

Figure 1.1: Schematic of the coaxial metallic pipe with its inner core. These pipe regions have been considered as the propagation medium and treated as metallic waveguides.

The present work achieves the following scientific research goals and engineering contributions:

- Contributing to the development of future digital-based oil fields. Some key principles were set out in the thesis for enhancing oilfield monitoring and are focused on evolving the digitalization of information.
- Expanding antenna generated controlled propagation scenarios for communications in enclosed environments such as caves, mines, tunnels, and pipelines. There is this common motivation to develop systems where the propagation occurs inside the enclosed environments. It allows monitoring variables like received signal strength, signal attenuation, or environment temperature.
- Assessing and modelling the physical pipeline architectures and electromagnetic environment for the application of wireless RF communications and data collection, as well as a liquid level determination system. This research aims to model and develop those systems in a shallow sub-surface well environment, which uses antennas and RF components.
- The analysis, design, and optimization of antennas and RF components and the system modelling, design, and implementation. The developed RF wireless system is implemented in the pipeline defining the excitation and receiving techniques, the propagation, and the limitations.
- Assisting in the productivity of well operations and identifying the well flow rate capacity by measuring the fluid level in the pipeline. Furthermore, this solution

would accommodate the identification of the location of faulty flow valves in gas-lift operations and the optimization of speed, size, and location of the submersible pump [7].

- Verifying full-wave EM simulated modelling with the numerical and mathematical modelling work. This will serve the purpose of offering a more complete exposition of the simulating models reducing the time and the volume of the work that relates to the modelling aspect to the future reader.aspects. This can save engineering time in the future, in that the developed numerical models are a good starting point in the design process.

The resulting configurations also differ from more classical waveguide excitation techniques, which are typically vertical probe and loop feeds [32]. The systems are chosen to effectively operate at the ISM frequency bands within the enclosed overmoded metallic pipes. The selection of the proper antenna for directive field propagation inside the pipeline is essential for the operation of the proposed transmission system. A compact planar Yagi-Uda printed circuit board (PCB) based antenna was designed and optimized using a commercial full-wave simulation tool (CST Studio Suite EM Field Simulation Software) for the aforesaid reasons.

An alternative version of the designed PCB antenna was used for the implementation of another RF system developed by the candidate to achieve remote microwave sterilization of the coronavirus [33]–[35]. This research was undertaken in parallel with the presented works of this thesis on oil gas well RF systems, as a hobby, mainly, due to the importance of the sterilization work which helped to circumvent the pandemic. It should also be mentioned that due to these activities, the candidate was the recipient of the COVID-19 "Above and Beyond" Medal for leading this research by the School of Engineering, The University of Edinburgh. Also, he was awarded the URSI GASS 2021 Young Scientist Award and received an Honourable Mention in the AP-S Student Paper Competition. All in all, it should be mentioned that some findings and techniques (such as the end-fire Yagi-Uda antenna) developed in the current thesis were also used in the microwave remote sterilization project. Therefore, the candidate refers to this project in the central contribution section, despite the sterilization work itself, seeming somewhat irrelevant to the oil and gas/microwave systems, as outlined in the following, which is the core focus of this thesis. Also, the references to the published work about microwave remote sterilization research are outlined in Appendix A.

1.3 Safety Standards

In this section, some guidance and regulations relative to the filling material and the RF equipment and devices are outlined since the operational zone of oil and gas sites can be considered restricted and potentially hazardous areas to the general public [36]. The main focus of this thesis study, as already mentioned, concerns the advancement of sensing technologies for the oil and gas industry. This sector has a dangerous area classification by the United Kingdom (UK) government agency Health and Safety Executive (HSE) [36]. Additionally, RF equipment, wireless networks, and devices such as antennas were required for use in this research. The devices used in, around, or near hazardous areas must satisfy various criteria. These criteria are about explosion proof standards and legal regulations [37].

In the IEC 60079-0 document, which includes the electrical apparatus for explosive gas atmospheres international standard, the RF limits of the equipment for all hazardous areas can be found. Based on the hazardous area classifications and protections, methane and natural gas, which are the gases that the system is designed for (see 2.4), belong to IIA group [38]. This group has a threshold Effective Isotropic Radiated Power (EIRP) level of 6 Watts [38]. The RF power for each device developed for such systems must be below the acceptable limits for these specific hazardous areas. Also, to prevent the risk of ignition from sparks, electrical faults, or hot surfaces, the chosen RF devices must have suitable Explosion Protected (Ex) approvals. More specifically, the equipment ought to either be Ex-approved or to be installed in an enclosed system that provides the Ex-protection [39]. The equipment used in the hazardous must also have a certification by the British Approvals Service for Electrical Equipment in Flammable Atmospheres (Baseefa), otherwise cannot be used.

Following these standards, the candidate should highlight that the research and measurements for this thesis have not been carried out in any hazardous areas since the filling material used for the pipelines was air, and experiments were carried out in a simple laboratory setting. In the future, when measurements are made where methane or natural gas will be used to extend the practice of the research, it is imperative to comply with all regulations and provisions regarding the involvement of any RF equipment in hazardous areas and materials. Baseefa guidance should be followed.

1.4 Thesis Overview

The remainder of this thesis is organized as follows:

Chapter 2

An overview of the relevant technologies as applied in oil and gas wells and other enclosed environments is discussed in this chapter. In particular, classical and more recent techniques and methods in data communications within oil and gas wells and liquid level determination are outlined. Moreover, the advantages of the proposed systems are presented in comparison to the other methods. In addition, some challenging electromagnetic environments (such as trains, tunnels, and airplanes) that could adopt this thesis's findings are highlighted.

Chapter 3

This chapter examines the feasibility of a wireless system for propagation inside an oil and gas well pipeline. The well is modeled as a circular aluminium pipe treated like a metallic microwave waveguide. Also, the circular waveguide theory as applied to the inner core of the pipeline is discussed. As the transceivers, half-wave dipoles operating at 2.5 GHz were employed. Due to this excitation technique and the enclosed environment parameters such as the propagating mode, the antennas' directivity and realized effective gain also needed to be studied for this scenario. A numerical transmission path loss (TPL) model was developed and verified using full-wave simulations and lab measurements. The transmission and the continuous monitoring of sensory data such as temperature and pressure were then tested. This study and experimental work was a

starting point for the implementation of higher-speed wireless communications inside oil and gas well pipelines for real-time data transmission at microwave frequencies, using more directive antennas, which is presented in Chapter 4.

Chapter 4

The modeling and design of a communication system are examined in this chapter, where the signal propagates within a circular metallic pipeline using directive PCB-based antennas. The propagating mode, the TPL, the directivity, and the impulse response are also all defined. Moreover, a manufactured antenna housing is reported for protection of the antenna itself (as well as the supporting electronic circuits) from oil and gas product flow and the potentially high temperatures, and pressures [40]. In addition, an EM power link budget equation is developed at 2.4 GHz using a 36-meter carbon steel pipeline which can be applied for any pipe length. The transmission and monitoring in real-time of sensory data such as temperature/pressure, digital images and videos are outlined in this chapter. Finally, the limitations of the system in terms of parameters, such as the minimum received power for data communications, are reported.

Chapter 5

This chapter describes the modeling and design of a complete wireless microwave liquid level determination system within an overmoded coaxial metallic pipeline. The first part defines the coaxial waveguide characteristics and provides an overview of the relevant microwave theory applied to the coaxial pipeline. Also, parameters such as the excited modes, the conductor losses, and the group velocity are documented in the chapter. Also, a simulated liquid level determination for three different liquids (water, seawater, and oil) is presented, and a fundamental link budget equation is given based on the reflection coefficient of the waveguide source. The operation of a 2-meter carbon steel pipeline at 2.4 GHz is also studied when an end-fire microstrip-based planar antenna is positioned into a housing acting as the source of the system. Testing of this proposed microwave system for the liquid level determination is presented, using a reflectometry system and two different kinds of exciting pulses. The results of this test were used to develop a link budget equation to calculate the maximum depth that can be achieved for the system.

Chapter 6

This chapter concludes this thesis and provides possible future research directions.

Chapter 2

Background

This chapter reviews the communications and the liquid level determination methods within oil and gas well pipelines. Also, a communication system inside some enclosed environments is presented, with similar architecture to the oil and gas wells. The employed filling material within the studied oil and gas pipelines is analysed and explained. The chapter also provides some technical background on the basic principles of telecommunication systems and microwave waveguides.

2.1 Communications within Oil and Gas Well Pipelines

The history of the oil and gas industry reflects local and global political events, economic constraints, and the personal endeavours of individual petroleum geoscientists, as much as it does the development of technologies and the underlying geology [2]. Because of the importance of the oil and gas industry, many companies and researchers are studying and developing new communication and sensor technologies [6], [8], [11], [13]. The problems to be resolved are the real-time and continuous monitoring of the pipeline condition, seismic activity, corrosion, possible gas leak detection, and other similar issues. The most widespread technologies which are dealing with these issues include the development of new wireless sensor networks for the internet of things (IoT) and other applications [8]. However, the fully demonstrated propagation system, driven by directive antennas, has not existed previously as outlined in this thesis. As discussed, such a system can offer the exchange of sensory data information within oil and gas well pipelines.

Several attempts have been made to achieve communications within a pipeline for the oil and gas sector at low frequencies, i.e. below 30 Hz and in the low kHz range (see Table 2.1). In [41], for example, the characteristics for radio wave propagation in a lossy circular waveguide, which can be used in boreholes, such as the possible propagating modes and the relevant attenuation contestants, were presented. The study was focused only on the electromagnetic propagation inside the waveguides, and it managed to define the exciting modes and their attenuation constants for specific scenarios. However, it did not establish any communication system while observing signal attenuation losses of about 1.2 dB/meter for a pipe length of 5 meters.

The goal in [9] was to investigate the application of a gas pipeline, firstly as a waveguide and secondly as a conductor, to identify and repair pipeline problems. The results were promising and showed that the signal could be transmitted through the pipe at frequencies of a few GHz. The authors in [10] proposed a system implemented by wireless inertial measurement unit (IMU) modules placed in series along the downhole,

receiving data with a sampling rate of 5 Hz. A 30-meter drill pipe test suggested that data transmission was possible. However, in that study [10], the system was not well defined, nor was the type of pipe, the EM characteristics of the setup, or any details on the completed experimental testing.

More recent attention has focused on increasing the data communications rate within oil and gas wells [11]. The authors used two piezoelectric actuators to double the transmission rate in a 3-meter pipeline. Each actuator transmitted from 2 to 6 kHz, and the signal transmission was implemented using orthogonal frequency division multiplexing (OFDM). The results showed that the system had a good performance and that using more actuators could improve the data transmission. The research focused on calculating the signal-to-noise ratio (SNR) and bit error rate (BER) in various scenarios than on measuring the actual data rate itself.

In [12] and [13], the authors performed three wireless telemetry methods within oil and gas wells: EM telemetry (EMT), mud pulse telemetry (MPT), and continuous wave telemetry (CWT). These three systems are considered the most modern systems for oil-field drilling operations. The techniques operate in a very low frequency ($<$ 100 Hz for EMT and MPT and $<$ 2 kHz for CWT) [12], [13], and they can transmit data for tremendous depths above 12 km for MPT, 3 km for EMT and 8 km for CWT. EMT has the advantage of bi-directional communications, and it does not demand the existence of drilling fluid but has a minimum data rate. MPT is reliable as it has been vastly developed throughout the years [13]. However, it has the disadvantage that its attenuation constant is dependent on the fluid within the pipeline. These three telemetry methods suffer from high signal attenuation and additionally offer limited data rates [12]. For improving their performance, enhanced signal processing methods (such as noise cancellation and equalization) were studied and applied to MPT using phase-shift-keying (PSK) [12] - [13]. More specifically, spatial diversity and dynamic models for signal processing, and algorithms for noise cancellation were used to improve the data transfer quality.

It is important to mention that the proposed application and borehole fluid, for the microwave wireless system as reported in this thesis, is different for EMT, MPT, and CWT. This is because the specific evaluation of fluid composition within the pipeline can help define the carrier frequency more accurately for data exchange. The proposed transmission method of this thesis offers higher data transmission rates than those employing lower frequency methods and successfully demonstrated an alternative modulation scheme in contrast to [12] - [13], providing a potential advancement for communications within oil and gas wells. An important differentiator is that the proposed pipeline-based communications system can be used simultaneously during the production process when the composition is mainly dry gas; i.e. methane) [42], to obtain the transmission of essential sensory information, such as temperature and pressure data within the interior of the pipe.

All the aforementioned studies [41] - [13] for establishing communication links for oil and gas wells have not examined the complete EM system, as examined in Chapters 3 and 4 of this thesis, by reporting the following: (i) a study of the relevant properties of the pipe which confines the signal, (ii) antenna selection and design to ensure directed propagation while integrating a housing for protection from oil and gas product flow, (iii) complete system simulation, testing, and analysis while considering commercially sized pipelines, (iv) the adoption of IEEE standard wireless communication protocols, (v)

Reference	Testing Frequencies	Pipe Type	Propagation Environment	Data Modulation Scheme	Signal Transmission Depth	Signal Attenuation Max Constant
[41]	0.1 - 10 GHz	Circular by Soil Walls	-	-	5 m	1.91 dB/m
[9]	1 kHz - 6 GHz	-	-	Optimized Link State Routing (OLSR)	3.5 m	1
[10]	RF	-	IEEE 802.15.4	30 m	-	
[11]	2 - 6 kHz	Circular by Steel	-	OFDM	3 m	-
EMT [12], [13]	< 100 Hz	-	Borehole Fluid	-	3 km	[1]High
MPT [12], [13]	< 30 Hz	-	Borehole Fluid	-	12 km	[1]High
CWT [12]	0.1 - 2 kHz	-	Borehole Fluid	-	8 km	[1]High
Proposed System	2.2 - 2.6 GHz	Circular by Carbon Steel 1010	OFDM	[2]36.03 m / ≈150 m	0.4 dB/m	

No values were reported or metrics described for '-'.

[1] Exact values were not reported but were stated as *High*.

[2] The values of 36.03 meters and ≈150 meters were respectively measured with physical metallic pipeline (see Fig. 4.1) and experimentally determined using attenuators.

Table 2.1: Comparison to the other oil & gas wells communication systems

definition of the system limitations in terms of required transmit powers and SNR while employing in-house programmed universal software radio peripherals (USRP) modems, and, (vi) in the field experimental testing at the ISM band. A complete analytical treatment (vii) is also newly developed, defining the power flow in the circular pipe, which has never been reported previously to the best knowledge of the candidate.

2.2 Liquid Level Determination Method for Oil and Gas Pipelines

The first attempts to measure the subsurface conditions of oil and gas wells were conducted around the early 1920s. This was followed by advances that led to evaluations of the hydrocarbon fluid composition and liquid levels, and some of these studies included wired pressure gauges which ran to the bottom of oil wells [18], [19]. It should be mentioned that these electrically connected methods for acquiring well data and installing the pressure control safety equipment are historically expensive and operationally time consuming [18], [19].

To overcome these challenges, oilfield operators have further developed many different measurement tools and techniques to obtain specific well production data. This has also allowed for gathering more accurate measurements for liquid level determinations. Some of these early advancements led to the development of acoustic sensor measurements and echo-meters [18] which record the liquid level by using pressure waves that are generated by a compressed gas source and operate in the acoustic frequency range. These acoustic based methods provide the basis for calculating the liquid level, inferred from the travel time of the returning sound waves transmitted from the wellhead to the liquid interface. These measurement approaches, therefore, make use of the acoustic-wave velocity [18], [20], and the time of flight within such systems.

Different approaches developed into sonic metering systems, relying on acoustic waves. In general, the application of acoustical methods at the kHz range of frequencies

to determine the liquid levels in oil and gas wells has been the most widely deployed technique [21]–[23]. The disadvantage of these systems is that they can be bulky to deploy and generally require operators to be on-site to install the temporary equipment and manage the safety of the pressure controls at the wellhead. Some issues in using acoustic measurement systems are the high measurement errors due to the mechanical noise inside the annulus region and the variations in signal velocity. Parameters such as the vibrations of the tubing string, acoustic noise interference of the pump, and disturbances in the annular casing structure can also cause unwanted noise at the receiver [24]. For these reasons, the acoustic methods, have continuously evolved and generally require advanced signal processing procedures for the interpretation of reliable liquid level determination [21]–[30]. To overcome some of these issues, the authors in [25] managed to improve the signal to noise ratio (SNR) by using some signal processing algorithms and fiber-optics, which included high-pass filtering and short-Fourier transforms applied to the reflected acoustic signals. However, when implementing these fiber-optics based sensor systems [29], [30], the expensive cabling required to be installed downhole, can further complicate the essential production measurements during standard crude extraction operations.

Additionally, other signal processing methods which have been presented in the bibliography have employed some autocorrelation methods [26] and genetic algorithms [27] to the acoustic signal at the receiver side. The autocorrelation method improves the measurement accuracy, and noise immunity of the weak reflected acoustic signals [26]. The genetic algorithm approach helps to provide some precision in the received signal thus providing more confidence in the results. In general, the conventional acoustic-based measurement methods present additional wellsite hazards as they require personnel to work with charged pressure cylinders and electrical tools close to the wellhead to conduct the measurement operations [28].

It should also be mentioned that a common phenomenon that can occur in oil and gas wells, is that a volume of gas can create a foam section above the liquid level. The length of the foam section can be hundreds of meters long, and as it has low acoustic wave reflection capability, the sound is absorbed into this gas column. It is not easy in this case to measure the depth of the liquid level. The authors in [29] proposed a system implemented by a sensor that combines an auxiliary heating element with an optical fiber. This system can identify the levels of liquid and foam sections segregated within the well. Further distributed sensor measurements in [30] are presented as an alternative method for the determination of the liquid level using multi-mode optical fiber and a pressure sensor. However, this method for the real-time monitoring of the liquid level requires the use of a pressure sensor and fiber optic cabling to be installed downhole, making the system more complicated and expensive.

A few more methods are used for liquid level determination, but there are not widely used, the thermomanometric and dynamometry or wattmeter methods. In the thermomanometric method, pressure and temperature sensors are used along the wellbore, making the cost for this system to be very high. On the other hand, the wattmeter cards have a complex interpretation process, making this method, not ideal [24].

In Table 2.2 the widely used liquid level determination methods are compared with the proposed system with some qualitative characteristics such as performance, complexity, and safety. As it was already mentioned, the performance of the acoustic methods without the use of the applied signal processing techniques is low as there is a significant

System	Operational Frequencies	Performance	Complexity	Safety
Acoustic [21] - [30]	$\backsim$ kHz Acoustical	Medium	High	Medium
Proposed	2.4 GHz ISM	High	Medium	Medium/High

Table 2.2: Liquid level determination methods comparisons

level of mechanical noise in the annulus region, and the range depth error is high [24]. On the other hand, the estimated error is around 0.5% (see Subsection 5.5). Moreover, the proposed system in this thesis allows for a more simplified wellhead installation by the implementation of the novel mechanical antenna housing, which can eliminate the complexity and cost of the acoustical and cable-based (i.e. fiber optics, etc.) measurement systems, which can be time and labour intensive with the additional personnel required to be on-site [20]–[22].

In terms of safety, both the acoustic and the proposed methods have to consider the associated operational risk exposure closely. The acoustic based ranging methods generally use compressed gas cylinders as a pressure source, and the proposed system uses an RF amplifier as the power source; therefore, due consideration must be employed with specific procedures when operating in hazardous areas [36]. To overcome these challenges, this thesis proposes an alternative and wireless method for liquid depth determination using microwave and antenna engineering principles as well as the supporting signal processing (see Chapter 5).

2.3 Communication Scenarios within Enclosed Environments

Findings from this thesis are closely applicable to other communication scenarios within enclosed environments, which include, metallic air-ducts, airplanes [43], tunnels [44]–[47], trains [48], [49] and mines or caves [50]. In principle, any other challenging and internal electromagnetic environment [43]-[50] requires wireless signal propagation and demands innovative solutions for data exchange.

Data collection for applications such as aeronautical, transportation, and space sectors are presented in [43] through a smart cable system and its elements. The system includes active and programmable RF switches which control the radiation at specific nodes or hotspots. It was proven that the system performance estimations for a real corridor satisfy typical sensor sensitivity requirements [43].

In terms of the radio wave propagation in tunnels [44], there have been some studies like the training of models to recognize the path loss exponent (PLE). In those studies, a training model called "electromagnetic vision" was developed. This model can give the propagation characteristics of a channel based on defined input information that carries the channel's geometric properties. The data was exported from a real tunnel, with its structure being empirically known. The training covers a 4km range, and the frequency is 450 MHz [44]. In addition, except for the prediction of the PLE, significant steps have been made to analyse a complete wireless communication system in closed interior

environments. A transceiver system has been managed to measure signal strength, noise, and intermodulation for the up and downlink signal paths, using distributed antenna networks, filters, and multiple couplers. It was achieved in a complete functional system for all the protocols, and the required margins [45].

Following these developments, the authors in [46] presented a propagation modeling technique, which combines the vector parabolic equation (VPE) and some rectangular waveguide mode theory for communication in tunnels. The analytical computation of fields (generated using VPE) over arbitrarily long distances was extracted using a rectangular waveguide model for the tunnel. Furthermore, the authors added more realistic scenarios to their study, taking into account the surface roughness, parameterized it using a Karhunen-Loève expansion, and then embedded it into the VPE [47].

The investigation of wireless propagation has been examined under specific circumstances, such as the roughness of the surface in caves and mines. Mainly examined was the behaviour of radio wave propagation in these conditions. Also, ray tracing techniques can be considered in the modelling and the scattering effects from any possible rough surfaces. In a ray-tracing technique, the electromagnetic waves behave as propagation rays that tolerate the impediments that may exist due to reflection, attenuation, and diffuse scattering. The signal strength was described in terms of the transmitter-receiver distance at 2.4 GHz [50]. Also, a study in the open-air sections of the London Underground for the evaluation of the performance of a communications-based train control system was presented in [48]. As outlined in the paper, the developed hybrid model was noted to improve accuracy and computation time.

2.4 Filling Material

This subsection describes some typical well flow conditions that exist in an oil and gas well, i.e. the filling material of the pipeline. The variety of the well flow is wide, and the following short study documented the possible well flow conditions that were assumed for this thesis.

Essentially the well flow conditions contain multi-phase mixtures in general (Gas, Oil, and Water). The full range of possible chemical components is too broad to describe for all production situations. Therefore it was chosen in this project to define a simplified model that will represent certain well type conditions for the current project. While there is oil- or gas-only types of wells, the well-stream will often consist of a full range of hydrocarbons from gas (methane, butane, propane, and more) and condensates (medium density hydrocarbons) to crude oil [31], [51]. For the research outlined in the thesis, it is also acknowledged that any water content may absorb or partially reflect the microwave signal; therefore, it is chosen to mainly assess the RF propagation under typical dry gas scenarios in certain well types and then consider the detrimental effect of other liquid crude mixtures [31], [51].

The actual chemical composition is defined by the in-situ downhole temperature and pressure of the hydrocarbon mixture, which is considered methane (C_2H_4). The in-situ pressure and temperature in the wells can be approximated from the following rules [42].

- Temperature increases with depth at a rate of about 1.3° F per 100 ft on average.
- Approximating bottom hole temp can be determined by taking the rate 1.3° F/100

multiplying by the depth plus the average ground temperature.

- The pressure in the well at a given depth can be calculated using the hydro-static equation,

$$\begin{aligned} \mathrm{P} &= \mathrm{D} \times g \times d, \end{aligned} \tag{2.1}$$

where P is the pressure, D is the density of the liquid, g is gravity (9.8 $\mathrm{m/s^2}$) and d is the depth (or height) of the liquid.

A depth of 2000 meters is considered propagation down the well, typical for shallow sub-surface well depth. So, this is the standard depth considered in every analysis of this work. For a depth of 2000 meters (6561.68 feet), the temperature becomes,

$$\begin{aligned} \mathrm{T} &= 1.3^{\circ}\mathrm{F} \cdot 6561.68/100 \\ &= 85.3^{\circ}\ \mathrm{F}, \end{aligned} \tag{2.2}$$

adding the ground temperature, which is $74^{\circ}F$,

$$\begin{aligned} \mathrm{T} &= 159.3^{\circ}\mathrm{F} \\ &\approx 344\ \mathrm{K}. \end{aligned} \tag{2.3}$$

This temperature can be considered room temperature, so it is assumed that the density of methane is 0.717 $\mathrm{kg/m^3}$. For the same depth (2000 m), based on (2.1), the pressure is equal to

$$\begin{aligned} \mathrm{P} &= \mathrm{D} \times g \times d \\ &= 0.717 \times 9.8 \times 2000 \\ &= 11\ \mathrm{kPa}. \end{aligned} \tag{2.4}$$

Regardless of these calculations, methane is naturally a gas and can form a liquid when it goes below 188 K or above 4600 kPa; for the experimental research model and given these calculations, the pipe was considered to only contain methane in gaseous form. Thus, this study is assumed that methane will always be contained in a gas phase. Based on these assumptions, the gas could be considered the electric properties of a vacuum for the RF propagation model. In real conditions, if the well bottom-hole pressure drops below the dew-point pressure, then condensate (liquid) drops can develop from the gas phase, forming a region of liquid in the well. This multi-phase flow scenario was not considered for the current studies; only dry gas wells were considered. This, therefore, allowed the gas properties to be modeled with approximations, acting similar to air or a loss-less dielectric.

The actual gas composition and pressure gradient acting on depth in the well is a function of the Pressure-Volume-Temperature relationship (PVT). However, to simplify the gas calculations for the EM study, a simple approximation was used for the project rather than using a PVT analysis which can be pretty complex based on all the hydrodynamic variables to consider in the well [42]. In addition, the following are some assumptions considered for the project. To keep the information of the pipe contents broadly consistent with the experimental work to date, these scenarios were considered [42], considering the typical configuration of the pipeline (see Fig. 1.1).

- Inside Pipe: methane mixture C_2H_4 (natural gas), i.e., production fluids coming from inside the well to the surface assumes that the crude fluid is in its gaseous phase for oil and gas well pressure and temperature conditions.
- Outer pipe (annulus): a methane (natural gas) mixture of C_2H_4 in the gaseous phase is injected into the well to form a gas lift surface compressor.
- Electrical properties: the electrical properties of the natural gas (methane) can be approximated as an air medium (having a relative dielectric constant of 1) or vacuum.

Based on these assumptions, the inner and outer pipe contents can be considered liquid and gas hydrocarbon mixtures under typical oil well pressure and temperature conditions. Also, within the actual conditions found in the well when it flows (maybe 10% of the time), it is expected to encounter a great variety of unwanted particulates, such as e.g. water, carbon dioxide, salts, sulphur, and sand; this should be acknowledged and will cause significant reflections, but this is beyond the scope of the current RF communications system development, and electromagnetic analysis [42]. So, the filling material is considered the air for the theoretical calculations, simulations, and measurements.

2.5 Technical Background

This section outlines some technical background about the basic principles of the developed telecommunication systems, the waveguides, and the digital communications.

2.5.1 Radio Frequency Telecommunication Systems

A classic telecommunication system can be split into three parts, the transmitter, the medium (guided, enclosed, free space), and the receiver [5]. The operation of the system is the transfer of information or power from the transmitter to the receiver [6]. An RF telecommunication system describes the propagation of radio waves with a frequency spectrum ranging from 20 kHz to around 300 GHz [52]. That means radio wave distances can be short, such as a few meters, or as long as kilometers. In radio engineering, an antenna is used with a transmitter and receiver, and it is the interface between radio waves propagating through the medium which enables said communications. Each antenna can be used with a transmitter and receiver and has some characteristics like gain and efficiency [53]. Also, the transmitted signal can be attenuated based on the system's environment. Based on all these parameters, the power balance or the link budget, which is essential for every system [5] can be defined,

$$\text{Received Power} \quad = \quad \text{Transmitted Power} + \text{Gains} - \text{Losses}.$$

As concerns the physical medium for data communications, the transmission path is where the signal propagates [32]. For electromagnetic waves, propagation may occur in a vacuum as well as in a material medium [32]. Other wave types cannot propagate through a vacuum and need a transmission medium to exist, like a waveguide which is a guided medium [32].

Figure 2.1: Example of metallic waveguides in an air-traffic control radar [54].

2.5.2 Principals of Waveguides

A widespread enclosed guided medium is the metallic waveguide. The coaxial metallic pipe with its inner core can be modeled as two metallic waveguides, the coaxial and the circular pipe. A structure that guides waves, such as electromagnetic waves or sound, is called a waveguide in the literature. Since the first waveguide structure appeared in the late 19th century, there have been many useful applications nowadays.

Waveguides are widely used in the following [55]:

- Optical fibre communication.
- Photonic integrated circuits.
- Maintaining high optical intensities in non-linear devices.
- As mode cleaners.
- Optical interferometers.
- High-power radar systems.

The basic principle of a waveguide is that the wave propagates in one dimension, and due to total reflection at the walls, waves are confined to the interior of a waveguide due to the boundary conditions. The basic propagation within each waveguide type is related to the propagated modes. The modes are the solution of the wave equation. Due to boundary conditions, a limited number of frequencies and waveforms can propagate in the waveguide. The mode with the lowest propagated frequency is the fundamental mode of the waveguide, and it carries the majority of the power.

The modes can be split into three types [32]:

- TE mode: transverse electric waves are defined by the fact that the electric field vector ($\mathbf{E}$) is always perpendicular to the direction of propagation.
- TM mode: transverse magnetic waves are defined by the fact that the magnetic field vector ($\mathbf{H}$) is always perpendicular to the direction of propagation.

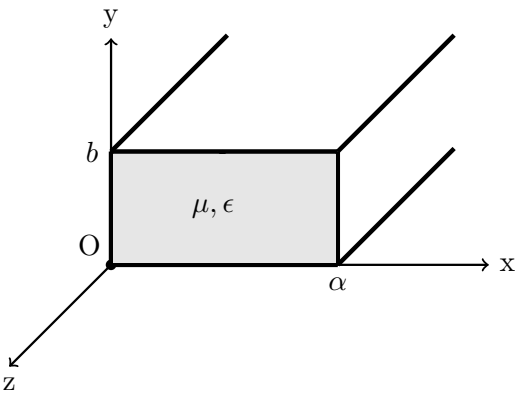

Figure 2.2: Rectangular Waveguide Structures and Geometry.

- TEM mode: transverse electromagnetic waves are used within coaxial and open wire feeders; also, it is defined by the fact that both the electric vector (**E**) and the magnetic vector (**H**) are perpendicular to the direction of propagation.

The following discussions provide an analysis of some basic types of waveguides. Further information can be found in the classic books by D.M. Pozar [32] and N. Marvuvitz [56].

Rectangular Waveguides

The most well-known waveguide used in many applications is the rectangular metallic waveguide. They were the first used as transmission lines to transport microwave signals. The wide bandwidth that they can offer has led to the fabrication of many rectangular waveguide components like couplers and attenuators, all of which are commercially available. Nowadays, due to the tendency for smaller transmission lines, which is related to the fact that higher frequencies are exploited, which can offer higher data rates, some applications also include high-power radar systems and satellite communications.

TM and TE modes can propagate in a rectangular waveguide, not TEM waves since only one conductor is available for current flow. Based on the geometry of Fig. 2.2 the components of the electromagnetic field for TE modes are defined as [32],

$$E_{\mathrm{x}} = \frac{j\omega\mu n\pi}{k_c^2 b} A\cos\frac{m\pi \mathrm{x}}{\alpha}\sin\frac{n\pi \mathrm{y}}{b}e^{-j\beta \mathrm{z}}, \tag{2.5}$$

$$E_{\mathrm{y}} = \frac{-j\omega\mu m\pi}{k_c^2 \alpha} A\sin\frac{m\pi \mathrm{x}}{\alpha}\cos\frac{n\pi \mathrm{y}}{b}e^{-j\beta \mathrm{z}}, \tag{2.6}$$

$$E_{\mathrm{z}} = 0 \tag{2.7}$$

and

$$H_{\mathrm{x}} = \frac{j\beta m\pi}{k_c^2 \alpha} A\sin\frac{m\pi \mathrm{x}}{\alpha}\cos\frac{n\pi \mathrm{y}}{b}e^{-j\beta \mathrm{z}}, \tag{2.8}$$

$$H_{\mathrm{y}} = \frac{j\beta n\pi}{k_c^2 b} A\cos\frac{m\pi \mathrm{x}}{\alpha}\sin\frac{n\pi \mathrm{y}}{b}e^{-j\beta \mathrm{z}}, \tag{2.9}$$

$$H_{\mathrm{z}} = A\cos\frac{m\pi \mathrm{x}}{\alpha}\cos\frac{n\pi \mathrm{y}}{b}e^{-j\beta \mathrm{z}}, \tag{2.10}$$

where $m, n \in \mathbb{N}_0$, where $\mathbb{N}_0$ are the natural numbers including 0, but they cannot be 0 at the same time; i.e., there is no a TE_{00} mode.

Respectively, components of the electromagnetic field for TM modes are defined as,

$$E_x = \frac{-j\beta m\pi}{k_c^2 \alpha} B \cos\frac{m\pi x}{\alpha} \sin\frac{n\pi y}{b} e^{-j\beta z}, \tag{2.11}$$

$$E_y = \frac{-j\beta n\pi}{k_c^2 b} B \sin\frac{m\pi x}{\alpha} \cos\frac{n\pi y}{b} e^{-j\beta z}, \tag{2.12}$$

$$E_z = B \sin\frac{m\pi x}{\alpha} \sin\frac{n\pi y}{b} e^{-j\beta z} \tag{2.13}$$

and TE

$$H_x = \frac{j\omega n\pi}{k_c^2 b} B \sin\frac{m\pi x}{\alpha} \cos\frac{n\pi y}{b} e^{-j\beta z}, \tag{2.14}$$

$$H_y = \frac{-j\omega \epsilon m\pi}{k_c^2 \alpha} B \cos\frac{m\pi x}{\alpha} \sin\frac{n\pi y}{b} e^{-j\beta z}, \tag{2.15}$$

$$H_z = 0, \tag{2.16}$$

where $m, n \in \mathbb{N}^*$. The μ and ϵ are the filling material's permeability and permittivity. The wavenumber is defined as k, and subtracting its square and the square of the phase propagation constant, which is symbolized as β, has the result for the cutoff wavenumber (k_c). Namely,

$$k_c = k^2 - \beta^2. \tag{2.17}$$

The constants A, and B are defined from the boundaries conditions of the solution of the Helmholtz wave equation,

$$\left(\nabla^2 + k^2\right)\psi = 0, \tag{2.18}$$

where ψ is a scalar function.

The cutoff frequency (f_c) for the TE_{mn} and TM_{mn} modes is given by

$$\begin{aligned} f_{c_{mn}} &= \frac{k_c}{2\pi\sqrt{\mu\epsilon}} \\ &= \frac{1}{2\pi\sqrt{\mu\epsilon}} \sqrt{\left(\frac{m\pi}{\alpha}\right)^2 + \left(\frac{n\pi}{b}\right)^2}. \end{aligned} \tag{2.19}$$

The dominant mode is the one that has the lowest cutoff frequency. In the case of the rectangular waveguide, it is the TE_{10} ($m = 1$, $n = 0$) mode, with a cutoff frequency

$$f_{c_{10}} = \frac{1}{2\pi\alpha\sqrt{\mu\epsilon}}. \tag{2.20}$$

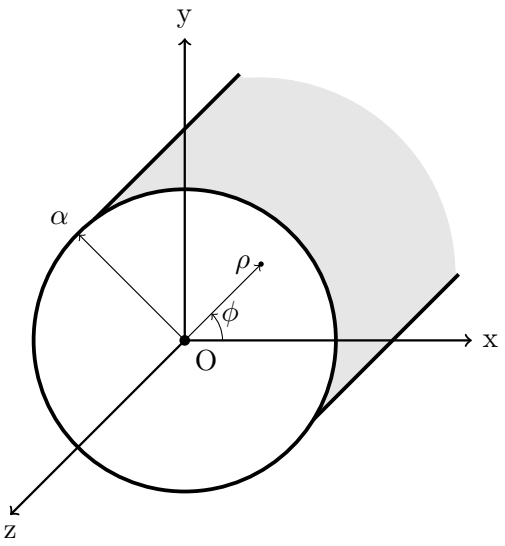

Figure 2.3: Circular Waveguide Structures and Geometry.

Circular Waveguides

A circular waveguide is a metal cavity that supports TE and TM modes. Fig. 2.3 shows the geometry of a circular waveguide with radius α. For simplicity, because of its geometry, cylindrical coordinates are employed.

The analytical expressions for the electromagnetic field for the TE_{mn} modes are given by [32], [56]:

$$E_\rho = \frac{-j\omega\mu m}{k_c^2\rho}\left(A\mathrm{cos}m\phi - B\mathrm{sin}m\phi\right) J_m(k_c\rho)e^{-j\beta \mathrm{z}}, \tag{2.21}$$

$$E_\phi = \frac{j\omega\mu}{k_c}\left(A\mathrm{sin}m\phi + B\mathrm{cos}m\phi\right) J'_m(k_c\rho)e^{-j\beta \mathrm{z}}, \tag{2.22}$$

$$E_\mathrm{z} = 0, \tag{2.23}$$

$$H_\rho = \frac{-j\beta}{k_c}\left(A\mathrm{sin}m\phi + B\mathrm{cos}m\phi\right) J'_m(k_c\rho)e^{-j\beta \mathrm{z}}, \tag{2.24}$$

$$H_\phi = \frac{-j\beta m}{k_c^2\rho}\left(A\mathrm{cos}m\phi - B\mathrm{sin}m\phi\right) J_m(k_c\rho)e^{-j\beta \mathrm{z}}, \tag{2.25}$$

$$H_\mathrm{z} = \left(A\mathrm{sin}m\phi + B\mathrm{cos}m\phi\right) J_m(k_c\rho)e^{-j\beta \mathrm{z}}. \tag{2.26}$$

On the other hand, the electromagnetic field for TM_{mn} modes is defined as,

$$E_\rho = \frac{-j\beta}{k_c}\left(A\mathrm{sin}m\phi + B\mathrm{cos}m\phi\right) J'_m(k_c\rho)e^{-j\beta \mathrm{z}}, \tag{2.27}$$

$$E_\phi = \frac{-j\beta m}{k_c^2\rho}\left(A\mathrm{cos}m\phi - B\mathrm{sin}m\phi\right) J_m(k_c\rho)e^{-j\beta \mathrm{z}}, \tag{2.28}$$

$$E_\mathrm{z} = \left(A\mathrm{sin}m\phi + B\mathrm{cos}m\phi\right) J_m(k_c\rho)e^{-j\beta \mathrm{z}}, \tag{2.29}$$

$$H_\rho = \frac{j\omega\epsilon m}{k_c^2\rho}\left(A\cos m\phi - B\sin m\phi\right) J_m(k_c\rho)e^{-j\beta z}, \tag{2.30}$$

$$H_\phi = \frac{-j\omega\epsilon}{k_c}\left(A\sin m\phi + B\cos m\phi\right) J'_m(k_c\rho)e^{-j\beta z}, \tag{2.31}$$

$$H_z = 0, \tag{2.32}$$

where $m \in \mathbb{N}_0$, and $n \in \mathbb{N}^\star$, for both types of modes. The term J_m is the mth-order Bessel Function and J'_m is its derivative. The constants A and B are defined from the boundary conditions of the solution of the Helmholtz wave equation in cylindrical coordinates. Thus, the cutoff wavenumber, in this case, is equal to

$$k_c = \frac{\chi'_{mn}}{\alpha}, \tag{2.33}$$

for TE_{mn} modes and

$$k_c = \frac{\chi_{mn}}{\alpha}, \tag{2.34}$$

for TM_{mn} modes. The χ_{mn} is the nth nonvanishing root of the mth-order Bessel Function, $J_m(\chi)$ and χ'_{mn} is the nth nonvanishing root of the derivative of the mth-order Bessel Function, $J'_m(\chi')$. That is the reason why the n cannot be 0.

The cutoff frequency ($f_{c_{mn}}$) for the TE_{mn} is given by

$$f_{c_{mn}} = \frac{1}{2\pi\alpha\sqrt{\mu\epsilon}}\chi'_{mn} \tag{2.35}$$

and for the TM_{mn} modes,

$$f_{c_{mn}} = \frac{1}{2\pi\alpha\sqrt{\mu\epsilon}}\chi_{mn}. \tag{2.36}$$

The dominant mode in a circular waveguide, which has the lowest cutoff frequency is the TE_{11} ($m = 1$, $n = 1$) mode,

$$f_{c_{11}} = \frac{1}{2\pi\alpha\sqrt{\mu\epsilon}}\chi'_{11}. \tag{2.37}$$

Coaxial Waveguide

The coaxial line can support TE and TM waveguide modes and the TEM mode. This transverse electromagnetic or TEM mode is the dominant mode in a coaxial guide. Its cutoff wavelength (λ_c) is infinite, and hence $\lambda_g = \lambda_0$ for the dominant mode (here λ_g is defined as the guided wavelength). The below figure shows the geometry of a coaxial line. The inner core's radius equals α, and the outer one is b. The cutoff frequency of the higher order modes are [56]

$$f_c = \frac{1}{2\pi\left(\alpha + b\right)\sqrt{\mu\epsilon}}\left(\frac{\alpha}{b} + 1\right)\chi'_{m1}, \tag{2.38}$$

for TE_{m1} modes,

$$f_c = \frac{1}{2\pi\left(\alpha - b\right)\sqrt{\mu\epsilon}}\left(\frac{\alpha}{b} - 1\right)\chi'_{mn}, \tag{2.39}$$

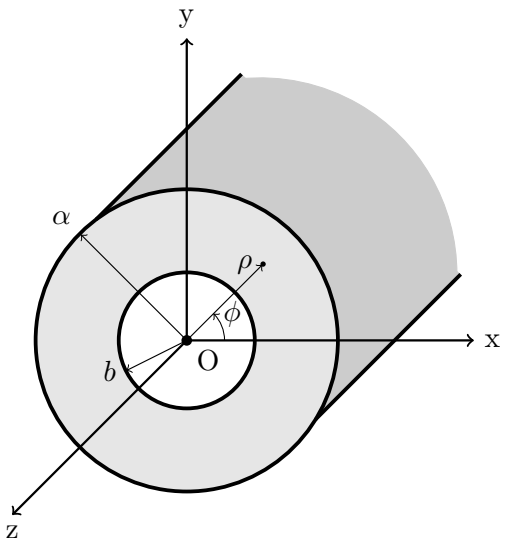

Figure 2.4: Coaxial Waveguide Structures & Geometry.

for TE_{mn} modes, when $n > 1$ and

$$f_c = \frac{1}{2\pi\left(\alpha - b\right)\sqrt{\mu\epsilon}}\left(\frac{\alpha}{b} - 1\right)\chi_{mn}, \tag{2.40}$$

for TM_{mn} modes. As χ_{mn} is symbolized by the n^{st} non-vanishing root of the m^{th}-order Bessel-Neumann Combination Function, $Z_m\left(\frac{\alpha}{b}\chi_{mn}\right)$, and as χ'_{mn} for the n^{st} non-vanishing root of the derivative of the m^{th}-order Bessel-Neumann Combination Function, $Z'_m\left(\frac{\alpha}{b}\chi'_{mn}\right)$.

2.5.3 Digital Transmission and Modulation

In telecommunications, digital transmission and modulation schemes are essential as they improve the quality of the communication channel and signal. The fundamental digital modulation techniques are based on keying such as PSK, and quadrature amplitude modulation (QAM). One of the most common PSK digital modulations is Binary PSK (BPSK), and Quadrature PSK (QPSK) [57].

BPSK is the simplest form of PSK, as it uses two phases which are separated by 180° (see Fig. 2.5a). Therefore, it handles the highest noise level or distortion before the demodulator reaches an incorrect decision and for this reason, it is the most robust of all the PSKs. It is, however, only able to modulate at 1 bit/symbol and so is unsuitable for high data-rate applications. On the other hand, QPSK uses four points on the constellation diagram, equispaced around a circle. With four phases, QPSK can encode two bits per symbol to minimize the BER (see Fig. 2.5b) [57].

OFDM is included among the popular schemes for modern wireless systems such as 4G, 5G, and Wi-Fi, where data communications are based on radiating antennas and free-space propagation [4]. In particular, OFDM is a process where time spaced samples are transformed to the frequency domain and separated into different subcarriers with spacing equal to the reciprocal of the symbol time. The spacing is to ensure that the subcarriers are orthogonal and do not interfere, allowing for more data subcarriers

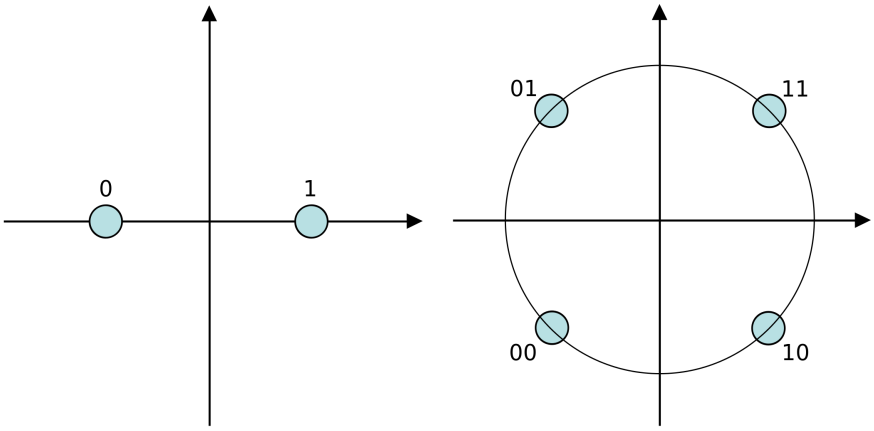

(a) BPSK Constellation Diagram (b) QPSK Constellation Diagram

Figure 2.5: Constellation diagram for BPSK and QPSK with Gray coding. Each adjacent symbol only differs by one bit in the QPSK [57].

without the inter-carrier guard bands necessary in FDM. Other subcarriers (pilot carriers, Direct Current or DC null subcarriers, side guard bands, cyclic prefix, and cyclic suffix) can still be used to try and improve the performance of OFDM. These additions whilst generally improving performance can however cause some issues. Firstly, the cyclic prefix copies the end of an OFDM symbol to the start of it to provide a guard interval between OFDM symbols to maintain orthogonality. It does however increase the size of an OFDM symbol and increases the overhead. It can also cause spectral regrowth (spreading of the bandwidth). Secondly, to combat the spectral regrowth issue raised cosine windowing (cyclic suffix) can be used to smooth the transition between OFDM symbols. This, however, can cause multipath fading in a communications system. OFDM also has the drawback of being very sensitive to frequency offsets and phase noise which can distort the received data [58].

2.6 Full-Wave EM Modelling

The commercial full-wave simulation tool used for this research was the CST Studio Suite EM Field Simulation Software. In this software were modelled all the major parts of the project, such as the oil and gas pipeline configurations including the modifications and the extensions, the antennas, and oil and gas liquids. The simulated models are compared to the well-known EM theory such as the cut-off frequency of the waveguides, and then to the actual measured mechanical and RF configurations for verifying the results, also at three different verification stages, i.e. numerical models to apply theory, full-wave CST simulations, and measurements for experimental validation.

This section is devoted to the details of the full-wave electromagnetic modelling work. In particular, the domain solver, the frequency/time range, the boundaries, any potential symmetry, the excitation ports with the signal type, mesh size, the total simulation time, and the potential limitations of the software are discussed for each model. For all the simulated models the modelled background into the software was having the EM properties of the vacuum. This serves the purpose of offering a more

Model	Domain Solver	Frequency Range	Boundaries	Excitation Port	Mesh Size (Tetrahedrons)	Total Simulation Time
Half-Wave Dipole	Frequency	2-3 GHz	(x,y,z): Open(add space)	Discrete Face (50 Ω Impedance)	10,954	67 s
PCB Yagi-Uda	Frequency	2-3 GHz	(x,y,z): Open(add space)	[1]Waveguide	237,844	1106 s

[1] The waveguide port was applied on the input of a SubMiniature version A (SMA) coaxial connector exciting the TEM mode. The reference impedance was 50 Ω.

Table 2.3: CST Studio Suite EM Field simulations parameters about the antenna models

complete exposition of the volume of work that relates to the modelling work.

2.6.1 Antennas

The antennas that were modelled in the CST Studio Suite EM Field Simulation Software for a half-wave dipole (see Fig. 3.6) and a compact planar Yagi-Uda printed circuit board (PCB) (see Fig. 4.3), both operating at 2.4 GHz. In the Table 2.3 the parameters and the details from the CST EM Field simulation software suite modelling of those antennas is shown.

2.6.2 Pipelines as Waveguides

The pipeline configuration that was modelled in CST Studio Suite EM Field Simulation Software was treated like waveguides. In particular, the circular and the coaxial waveguides were modelled by implementing two different materials (aluminium and carbon steel 1010). The length of the modelled waveguide was 50 mm. The thickness of the wall was 10 mm, for the circular waveguide and the outer pipe of the coaxial waveguide. In the Tables 2.4 - 2.7 are presented all the models that were simulated with their parameters and details based on CST.

The parameters that were simulated regarded the cut-off frequencies, the attenuation constant due to the conductivity of the walls, and the group velocity for each of the excited modes. Additional to those parameters, the attenuation constant of the dominant mode for each case with the relative permeability of the carbon steel 1010 was simulated. The range of the values of the μ_r is from 1 to 100. In the circular carbon steel 1010 model a layer of rust (Ferrous Ferric Oxide - Fe_3O_4) was applied in the interior of the circular waveguide, for the calculation of the attenuation constant due to the rust (α_r). All these results were compared with the theory of the literature. This theory was programmed in the MATLAB (available from Mathworks) software during the research and engineering work. In the Tables 2.4 - 2.7 are shown the total time for the MATLAB software to numerically calculate the results of all these parameters when compared with the corresponding CST simulation time. The analytical results from the simulations and the theoretical calculations are presented in Sections 4.2 and 5.2.

2.6.3 Coaxial Waveguide Terminated by Liquid

A simulation model was developed considering a coaxial carbon steel 1010 waveguide with radii 69.85 mm and 136.525 mm for unimodal propagation, while being terminated by liguid, in Section 5.3. The total length of the waveguide was set at 1 m and the liquid occupies 10% of the pipe, i.e. 1 cm. The modelled liquids were water, seawater, and lubricating oil. The EM properties of the liquids are discussed in the Section 5.3.

Model	Domain Solver	Frequency Range	Boundaries	Excitation Port	Mesh Size (Tetrahedrons)	Total Simulation Time	Total Calculation Time
[1]r = 69.85 mm [2]ϵ_r = 1	Frequency	2-2.8 GHz	(x,y): Open(add space) [3](z): Open	Waveguide (12 modes)	5,990	141 s	0.009308 s
r = 69.85 mm ϵ_r = 1.5	Frequency	2-2.8 GHz	(x,y): Open(add space) (z): Open	Waveguide (12 modes)	5,861	165 s	0.008858 s
r = 69.85 mm ϵ_r = 2	Frequency	2-2.8 GHz	(x,y): Open(add space) (z): Open	Waveguide (20 modes)	6,117	297 s	0.002894 s
r = 57.15 mm ϵ_r = 1	Frequency	2-2.8 GHz	(x,y): Open(add space) (z): Open	Waveguide (6 modes)	6,313	135 s	0.00371 s
r = 57.15 mm ϵ_r = 1.5	Frequency	2-2.8 GHz	(x,y): Open(add space) (z): Open	Waveguide (8 modes)	6,239	113 s	0.001662 s
r = 57.15 mm ϵ_r = 2	Frequency	2-2.8 GHz	(x,y): Open(add space) (z): Open	Waveguide (16 modes)	6,152	246 s	0.001926 s

[1] Circular waveguide radius. [2] Dielectric constant (ϵ_r) of the filling material.
[3] The open boundary condition simulates the absorbers of an actual system.

Table 2.4: CST Studio Suite EM Field simulations parameters about the circular aluminium waveguide models.

Model	Domain Solver	Frequency Range	Boundaries	Excitation Port	Mesh Size (Tetrahedrons)	Total Simulation Time	Total Calculation Time
r = 69.85 mm ϵ_r = 1	Frequency	2-2.8 GHz	(x,y): Open(add space) (z): Open	Waveguide (9 modes)	36,238	331 s	0.00167 s
r = 69.85 mm ϵ_r = 1.5	Frequency	2-2.8 GHz	(x,y): Open(add space) (z): Open	Waveguide (9 modes)	33,956	410 s	0.002252 s
r = 69.85 mm ϵ_r = 2	Frequency	2-2.8 GHz	(x,y): Open(add space) (z): Open	Waveguide (16 modes)	33,402	382 s	0.001342 s
r = 57.15 mm ϵ_r = 1	Frequency	2-2.8 GHz	(x,y): Open(add space) (z): Open	Waveguide (9 modes)	30,376	360 s	0.012378 s
r = 57.15 mm ϵ_r = 1.5	Frequency	2-2.8 GHz	(x,y): Open(add space) (z): Open	Waveguide (9 modes)	28,459	325 s	0.001092 s
r = 57.15 mm ϵ_r = 2	Frequency	2-2.8 GHz	(x,y): Open(add space) (z): Open	Waveguide (16 modes)	27,966	269 s	0.001598 s
[1] α_r of Fe_3O_4	Frequency	2-2.8 GHz	(x,y): Open(add space) (z): Open	Waveguide (9 mode)	40,349	367 s	0.001502 s
[2]α_c in function with the μ_r	Frequency	2-2.8 GHz	(x,y): Open(add space) (z): Open	Waveguide (1 mode)	5,990-36,238	32-331 s	0.00157

[1] Attenuation constant due to the rust (α_r).
The radius was set at 69.85 mm and the dielectric constant of the filling material was 1.
[2] Attenuation constant due to the conductivity of the wall (α_c) in function with the relative permeability (μ_r) for the TE_{11} mode.
The radius was 69.85 mm and the dielectric constant of the filling material was 1.

Table 2.5: CST Studio Suite EM Field simulations parameters about the circular carbon steel 1010 waveguide models.

In the Table 2.8 the details of the models for the aforementioned systems for each liquid are discussed.

2.6.4 Antenna Propagation into the Circular Waveguides

Several models about the half-wave dipole when placed inside a circular aluminium waveguide were developed and presented in Section 3.3. Firstly, the half-wave dipole, operating at 2.5 GHz, was placed inside a circular aluminium waveguide with a length of 50 mm. The starting radius of the modelled waveguide was 50 mm and gradually increased this radial parameter up to 1.5 m, which was the upper limit that the CST Studio Suite EM Field simulation software could solve. The mesh size was more than 1,000,000 tetrahedrons in most cases. In the second modelled system, the half-wave dipole was placed at the edge of the circular aluminium waveguide as the length of the waveguide varied from 0 to 1 m and radius 70 mm, 150 mm, and 250 mm. Also, the system was modelled for waveguide radius of 500 m and increasing its length from 0 to

Model	Domain Solver	Frequency Range	Boundaries	Excitation Port	Mesh Size (Tetrahedrons)	Total Simulation Time	Total Calculation Time
[1]$r_1 = 136.525$ mm $r_2 = 69.85$ mm $\epsilon_r = 1$	Frequency	2-2.8 GHz	(x,y): Open(add space) (z): Open	Waveguide (24 modes)	7,886	178 s	0.074544 s
$r_1 = 136.525$ mm $r_2 = 69.85$ mm $\epsilon_r = 1.5$	Frequency	2-2.8 GHz	(x,y): Open(add space) (z): Open	Waveguide (45 modes)	9,226	451 s	0.07511 s
$r_1 = 136.525$ mm $r_2 = 69.85$ mm $\epsilon_r = 2$	Frequency	2-2.8 GHz	(x,y): Open(add space) (z): Open	Waveguide (49 modes)	12,898	355 s	0.065744 s
$r_1 = 122.2375$ mm $r_2 = 57.15$ mm $\epsilon_r = 1$	Frequency	2-2.8 GHz	(x,y): Open(add space) (z): Open	Waveguide (20 modes)	6,301	110 s	0.06351 s
$r_1 = 122.2375$ mm $r_2 = 57.15$ mm $\epsilon_r = 1.5$	Frequency	2-2.8 GHz	(x,y): Open(add space) (z): Open	Waveguide (40 modes)	7,550	306 s	0.061826 s
$r_1 = 122.2375$ mm $r_2 = 57.15$ mm $\epsilon_r = 1.5$	Frequency	2-2.8 GHz	(x,y): Open(add space) (z): Open	Waveguide (45 modes)	9,942	425 s	0.065962 s

[1] Coaxial waveguide radii. r_1: outer pipe radius, r_2: inner core radius.

Table 2.6: CST Studio Suite EM Field simulations parameters about the coaxial aluminium waveguide models.

Model	Domain Solver	Frequency Range	Boundaries	Excitation Port	Mesh Size (Tetrahedrons)	Total Simulation Time	Total Calculation Time
$r_1 = 136.525$ mm $r_2 = 69.85$ mm $\epsilon_r = 1$	Frequency	2-2.8 GHz	(x,y): Open(add space) (z): Open	Waveguide (23 modes)	136,265	316 s	0.067056 s
$r_1 = 136.525$ mm $r_2 = 69.85$ mm $\epsilon_r = 1.5$	Frequency	2-2.8 GHz	(x,y): Open(add space) (z): Open	Waveguide (45 modes)	138,324	696 s	0.069914 s
$r_1 = 136.525$ mm $r_2 = 69.85$ mm $\epsilon_r = 2$	Frequency	2-2.8 GHz	(x,y): Open(add space) (z): Open	Waveguide (50 modes)	138,041	755 s	0.062472 s
$r_1 = 122.2375$ mm $r_2 = 57.15$ mm $\epsilon_r = 1$	Frequency	2-2.8 GHz	(x,y): Open(add space) (z): Open	Waveguide (22 modes)	119,818	285 s	0.074544 s
$r_1 = 122.2375$ mm $r_2 = 57.15$ mm $\epsilon_r = 1.5$	Frequency	2-2.8 GHz	(x,y): Open(add space) (z): Open	Waveguide (40 modes)	117,161	564 s	0.061958 s
$r_1 = 122.2375$ mm $r_2 = 57.15$ mm $\epsilon_r = 1.5$	Frequency	2-2.8 GHz	(x,y): Open(add space) (z): Open	Waveguide (45 modes)	118,138	597 s	0.064916 s
[3]α_c in function with the μ_r	Frequency	2-2.8 GHz	(x,y): Open(add space) (z): Open	Waveguide (1 mode)	7,823-136,265	27-82 s	0.068002 s

[1] Attenuation constant due to the conductivity of the wall (α_c) in function with the relative permeability (μ_r) for the TEM mode. The radii were 69.85 mm and 136.525 mm and the dielectric constant of the filling material was 1.

Table 2.7: CST Studio Suite EM Field simulations parameters about the coaxial carbon steel 1010 waveguide models.

[1]Model	Domain Solver	Frequency Range	Boundaries	Symmetries	Excitation Port	Mesh Size (Tetrahedrons)	Total Simulation Time
Water	Time	0-0.4 GHz	(x,y): Open(add space) (z): Open	(YZ, XZ): $H_t = 0$	Waveguide (1 mode)	50,688	133 s
Seawater	Time	0-0.4 GHz	(x,y): Open(add space) (z): Open	(YZ, XZ): $H_t = 0$	Waveguide (1 mode)	21,037	108 s
Oil	Time	0-0.4 GHz	(x,y): Open(add space) (z): Open	(YZ, XZ): $H_t = 0$	Waveguide (1 mode)	18,900	100 s

[1] The model includes the coaxial carbon steel 1010 waveguide with radii 69.85 mm and 136.525 mm and the liquid.

Table 2.8: CST Studio Suite EM Field simulations parameters about the coaxial waveguide terminated by liquid model.

0.8 m. Beyond this point, i.e for a radius of 500 mm and a length of 0.8 m, the software

Model	Domain Solver	Frequency Range	Boundaries	Excitation Port	Mesh Size (Tetrahedrons)	Total Simulation Time	Total Calculation Time
[1]Radius Testing	Frequency	2-3 GHz	(x,y): Open(add space) (z): Open	Discrete Face (50 Ω Impedance)	10,954 - 991,824	27-19854 s	-
[2]Length Testing	Frequency	2-3 GHz	(x,y): Open(add space) (z): Open	Discrete Face (50 Ω Impedance)	9,413 - 996,251	30-19702 s	-
[3]Transceiver System	Frequency	2-3 GHz	(x,y): Open(add space) (z): Open	Discrete Face (50 Ω Impedance)	130,693 - 176,164	1056-1395 s	0.54862 s

[1] The model includes the half-wave dipole which is placed inside a circular aluminium waveguide with a length of m.
The radius varied from 50 mm to 1.5m.
[2] The model includes the half-wave dipole which is placed inside a circular aluminium waveguide.
Its length was varied from 0 to 1 m and radius of 70 mm, 150 mm, and 250 mm, and from 0 to 0.8 m, with a radius of 500 mm.
[3] The model includes a circular aluminium waveguide with radius 69.85 mm, wall thickness 10 mm, and length 1 m.
A transmitter and a receiver dipole, placed at the two edges inside the waveguide.
The receiver dipole was moving from 0.86 m to 1 m distance from the transmitter dipole.

Table 2.9: CST Studio Suite EM Field simulations parameters about the half-wave dipole when placed inside a circular aluminium waveguide model.

was not able to simulate the model. The mesh size was more than 1,000,000 tetrahedrons. For all the simulated models the wall thickness was 10 mm. The purpose of the simulations for those models was to characterize the effective directivity see Subsection 3.3.2.

An aluminium waveguide of radius 69.85 mm, wall thickness 10 mm, and length 1 m was modelled for further simulations and testing. At the same time, the transmitter and the receiver dipoles were placed into the waveguide as illustrated in Fig. 3.11. The system was simulated by stimulating the dipole transmitter, while the receiver dipole was moving from 0.86 m to a 1 m distance from the transmitter dipole. The purpose of the simulation of this model was to characterize the dominant propagating mode, E-field, and the power flow along the waveguide, as well as, the development of the Transmission Path Loss (TPL) numerical model. The details of the simulations of the half-wave dipole when placed inside a circular aluminium waveguide and are presented in Table 2.9.

The PCB Yagi-Uda antenna, operating at 2.4 GHz, was modelled when placed inside a circular carbon steel 1010 waveguide with a radius of 69.85 mm, a wall thickness of 10 mm, and a length of 2 m. The starting radius of the modelled waveguide was 30 mm and gradually increased this radial parameter up to 1 m, which was the upper limit that the CST Studio Suite EM Field simulation software could solve. The mesh size was more than 1,000,000 tetrahedrons. The purpose of the simulation for this model was to characterize the effective directivity, see Subsection 4.4.4.

Furthermore, the same circular waveguide was modelled with a transmitter and a receiver PCB Yagi-Uda antenna was placed into the waveguide as illustrated in Fig. 4.6b. The purpose of the simulation of this model was to characterize the dominant propagated mode, E-field, and the power flow along the waveguide. The details of the simulations of the PCB Yagi-Uda antenna when placed inside a circular carbon steel 1010 waveguide are presented in Table 2.10.

2.6.5 Mandrels

The modelled mandrel includes a circular or coaxial carbon steel 1010 ($\mu_r = 1$) waveguide with a length of 2 m which on top, has an aluminium mechanical housing (radome) for the PCB Yagi-Uda antenna. Basically this housing can protect the antenna from gas

Model	Domain Solver	Frequency Range	Boundaries	Excitation Port	Mesh Size (Tetrahedrons)	Total Simulation Time
[1]Radius Testing	Frequency	2-3 GHz	(x,y): Open(add space) (z): Open	Waveguide (1 mode)	105,954 - 997,540	305-20103 s
[2]Transceiver System	Frequency	2-3 GHz	(x,y): Open(add space) (z): Open	Waveguide (1 mode)	237,067	1944 s

[1] The model includes the PCB Yagi-Uda antenna which is placed inside a circular carbon steel 1010 waveguide with a length of 2 m. The radius varied from 30 mm to 1 m.
[2] The model includes a 2 m circular carbon steel 1010 waveguide of radius 69.85 mm, wall thickness 10 mm. A transmitter and a receiver PCB Yagi-Uda antennas were placed at the two edges inside the waveguide.

Table 2.10: CST Studio Suite EM Field simulations parameters about the PCB Yagi-Uda antenna when placed inside a circular carbon steel 1010 waveguide model.

Model	Domain Solver	Frequency Range	Boundaries	Excitation Port	Mesh Size (Tetrahedrons)	Total Simulation Time
[1]Circular Mandrel	Frequency	2-2.8 GHz	(x,y): Open(add space) (z): Open	[2]Waveguide (1 mode) [3]Waveguide (5 modes)	251,226	13016 s
[4]Coaxial Mandrel	Frequency	2-2.8 GHz	(x,y): Open(add space) (z): Open	Waveguide (1 mode) Waveguide (23 modes)	284,074	25689 s

[1] The model includes a mandrel, consisting of a 2 m length circular carbon steel 1010 waveguide. On its top has an aluminium mechanical housing 1 m long (radome) for the PCB Yagi-Uda antenna. Between the housing and the waveguide, there is an acrylic sheet. The mandrel is terminated by a waveguide port.
[2] Port applied on the SMA coaxial connector exciting the TEM mode. [3] Port applied on the end of the mandrels.
[4] The model includes a mandrel, consisting of a 2 m length coaxial carbon steel 1010 waveguide. On its top has an aluminium mechanical housing 1.2 meters long (radome) for the PCB Yagi-Uda antenna. Between the housing and the waveguide, there is an acrylic sheet. The mandrel is terminated by a waveguide port.

Table 2.11: CST Studio Suite EM Field simulations parameters about the circular and coaxial mandrels when are terminated by waveguide port model.

flow. Between the housing and the waveguide there is an acrylic sheet (see Figs. 4.12, 4.13, 5.1, and 5.6). The housing on the circular mandrel was a 1-meter length, while on the coaxial mandrel was a 1.2 m length. Also, the mandrels were terminated by a waveguide port. The purpose of the simulation for those models was to characterize the coupling modes, the field routing, and the power flow along the mandrel. The details of the simulations of the circular and the coaxial mandrels when terminated by waveguide ports are shown in Table 2.11.

It should be mentioned that there were many efforts to model different mandrel configurations. In particular, some circular and coaxial mandrels where developed where the antennas would act as transceiver (see Figs. 4.13b, 5.9), and a coaxial mandrel would be terminated by liquid (see Fig. 5.1a). However, there was a limitation by the CST Studio Suite EM Field simulation software and the aforementioned models were not able to be solved. The mesh size of those models was overpassing the 1,000,000 tetrahedrons.

2.7 Summary

An overview of the relevant technologies applied in oil and gas wells and other enclosed environments was discussed in this chapter. In particular, classical and more recent techniques and methods in data communications within oil and gas wells and liquid level determination were outlined. Moreover, the advantages of the proposed systems are presented in comparison to the other methods. In addition, some challenging electromagnetic environments (such as trains, tunnels, and airplanes) that could adopt this thesis's findings are highlighted.

The employed filling material within the studied oil and gas pipelines was also explained. The inner and outer pipe content materials are assessed as liquid and gas hydrocarbon mixtures under typical oil well pressure and temperature conditions based on these assumptions. So for the theoretical calculations, simulations, and measurements, the filling material is considered to be air. Moreover, a brief technical background was presented about the basic principles of telecommunication systems, the supporting waveguides, and some principles for the adopted digital communications. Terms and parameters such as the link budget equation, TE modes, and, TM modes are widely used in the thesis, some background information was provided. Also, the three main waveguide structures were presented with their electromagnetic, and their cut-off frequency expressions were demonstrated. The adopted modulation scheme in the project was OFDM using BPSK and QPSK modulation techniques. For this reason, some principles on these topics were presented.

Furthermore, some background details of the full-wave electromagnetic modelling work were discussed. In the CST all major parts of the research work were modelled, such as the oil and gas pipeline configurations including the modifications and the extensions, the antennas, and oil and gas liquids. The simulated models are compared to the well-known EM theory such as the cut-off frequency of the waveguides, and then to the actual measured mechanical and RF configurations for verifying the results, in three different engineering perspectives, i.e. theory, simulations, and measurements.

Chapter 3

Wireless Propagation in a Metallic Pipe Using Half-Wave Dipoles

3.1 Introduction

This chapter introduces a feasibility investigation of a wireless communication system using microwave frequencies for high-speed real-time data transmission inside a circular aluminium pipeline over a one-meter distance. The circular metallic pipeline (defined as the inner core) is enclosed in a coaxial pipeline configuration. This concentric metallic pipe configuration is typical for oil and gas wells, thus ensuring mechanical mating with commercially available pipeline diameters. The inner core is treated like a metallic microwave waveguide. This is important because the circular waveguide theory can apply to the circular metallic waveguide. More specifically, the exciting modes are studied. The conductor losses, the EM fields, and the power flow along the pipeline are verified by numerical calculations and the CST Studio Suite EM simulation software.

The system operates at the ISM band is further defined and studied using two half-wave dipoles, which direct EM waves into the inner core and explain the transceivers (Fig. 3.11). Therefore the transmission medium can be considered as the inside of a metallic circular waveguide with an excitation technique that differs from the typical vertical probe and loop feeds [32]. Due to this excitation technique and the enclosed environment, parameters such as the propagating mode, the directivity, and the realized effective gain of the antennas also needed to be studied for this scenario. A numerical transmission path loss (TPL) model was developed and verified using the CST Studio Suite EM simulation software. and lab measurements for this specific case. The transmission and the continuous monitoring of sensory data such as temperature and pressure were then tested using N210 universal software radio peripheral (USRP) modems by National Instruments and coded using orthogonal frequency division multiplexing (OFDM).

3.2 Circular Waveguide Theory Applied on the Inner Core of the Pipeline

In this section, it is described how the inner core of an oil and gas well pipeline can be treated as a circular metallic waveguide. The propagating environment is defined by the dimensions, the structure, the materials, and the conditions under which the waveguide operates. Thus, it is analyzed by the possible modes, the conductor losses, the electro-

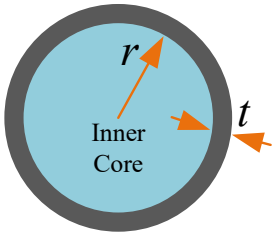

Figure 3.1: Inner core radius, $r = 69.85$ mm and wall thickness, $t = 10$ mm.

magnetic field, and the power flow through the waveguides at the operational frequency, set to 2.4 GHz. This is because there is an abundance of low-cost commercially available RF devices that operate at around 2.4 GHz, which will inherently reduce system implementation costs. This is also because the 2.4 GHz ISM band is typically employed for WiFi communications when adopting OFDM, as in this work, while abiding by the relevant IEEE 802.11 protocol.

3.2.1 Inner Core Characteristics

The selected inner core belongs to the typical pipelines for a commercial downhole well. The radius (r) of the chosen inner core is 69.85 mm (or $0.525\lambda_0$ at 2.4 GHz) and wall thickness $t = 10$ mm (or $0.08\lambda_0$ at 2.4 GHz), and where λ_0 represents the free space wavelength. Fig. 3.1 illustrates the structure of the waveguides and the critical dimensions. The grey color represents the metallic walls, and the turquoise represents the filling material.

3.2.2 Mode Analysis and Conductor Losses

The operational frequency has already been identified at 2.4 GHz, so every mode which has its cut-off frequency over this threshold does not propagate. Furthermore, based on [56], the cut-off frequencies for the propagating TE and TM modes are respectively,

$$f_{c_{\mathrm{TE}_{mn}}} = \frac{1}{2\pi r\sqrt{\mu_r\mu_0\epsilon_r\epsilon_0}}\chi'_{mn}, \tag{3.1}$$

$$f_{c_{\mathrm{TM}_{mn}}} = \frac{1}{2\pi r\sqrt{\mu_r\mu_0\epsilon_r\epsilon_0}}\chi_{mn}, \tag{3.2}$$

and calculations for the defined circular waveguide pipe are outlined in Table 3.1.

Here $m \in \mathbb{N}_0$, and $n \in \mathbb{N}^\star$, for both types of modes, and μ_0 and ϵ_0 are the magnetic permeability and the electric permittivity of the free space, respectively. The terms χ_{mn} and χ'_{mn} for each pair of mn are the roots of the first kind Bessel function and its derivative, respectively. That is the reason why the n cannot be 0.

Mode	Cut-off Frequency (GHz)	α_c (dB/m) due to Aluminium
TE_{11}	1.258	0.0043
TE_{21}	2.086	0.0073
TM_{01}	1.643	0.0164

Table 3.1: Cut-off frequencies of the propagated TE & TM modes in GHz for the circular waveguide

The relative magnetic permeability is symbolized as μ_r (being unitless) and is defined as the ratio between the permeability of the material and that of free space; i.e., $\mu_r = \frac{\mu}{mu_0}$. The relative electric permittivity is defined and symbolized respectively [32].

The walls of the waveguides are metallic, as already discussed. That means they are imperfect conductors, and thus there is power loss during signal propagation down the pipe. Conductor losses can be computed by the attenuation constant, α_c. This constant is the ratio of power loss per unit length by considering the power flow, and its units are in Np/m [32]. For the considered circular waveguide, each mode has its attenuation constant, and they are given by [56]:

$$\alpha_c = \frac{R_s}{\zeta r}\left[\frac{m^2}{\chi'^2_{mn} - m^2} + \left(\frac{\lambda_0}{\lambda_c}\right)^2\right]\frac{1}{\sqrt{1-\left(\frac{\lambda_0}{\lambda_c}\right)^2}}, \tag{3.3}$$

for TE modes and

$$\alpha_c = \frac{R_s}{\zeta r}\frac{1}{\sqrt{1-\left(\frac{\lambda_0}{\lambda_c}\right)^2}}, \tag{3.4}$$

for TM modes, where λ_c is the cut-off wavelength. Also, R_s, is the characteristic resistance of the metal walls and it is defined by [32], $R_s = \sqrt{\frac{\omega\mu}{2\sigma}}$ where ω is the angular frequency. Also, ζ is defined as the intrinsic impedance of the medium, and it is equal to $\sqrt{\frac{\mu}{\epsilon}}$. The σ symbolizes the electrical conductivity of the material, with units Siemens per meter, (S/m).

In this feasibility study, aluminium pipelines were chosen as long as aluminium has high electrical conductivity ($\sigma = 3.56 \times 10^7$ S/m) properties and it does not have magnetic properties [32]. Additionally, as described in 2.4 the medium within the pipe has the EM properties of vacuum (or air). Given these conditions, the attenuation constants for all the possible modes at 2.4 GHz; i.e., the TE_{11}, TM_{01} and the TE_{21} modes are reported in Table 3.1. The investigated pipeline is typically employed in the oil and gas industry. However, there are also a variety of other pipes with different radii used in practice and with varying properties of the material. Subsection 4.2.1 reports some more numerical calculations for the cut-off frequencies and the conductor losses for a carbon steel 1010 (material which will further be described in Subsection 4.2) pipe with as well as for aluminium pipes having radii of 57.15 mm and 69.85 mm. All these are typical pipes employed within the oil and gas industry. Also, more results are reported when the filling material is not similar to air but a crude methane vaporous mixture and the relative electric permittivity ranges from 1 to 2 [42]. Results are verified with the CST Studio Suite EM simulation software.

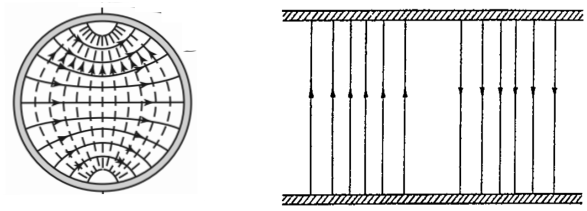

(a) (b)

Figure 3.2: Field plot illustrating electric (continuous lines) and magnetic field (dashed lines) of the dominant mode in the circular waveguide (TE_{11}). (a) The transverse plane from Pozar [32] and (b) Longitudinal plane from Marcuvitz [56].

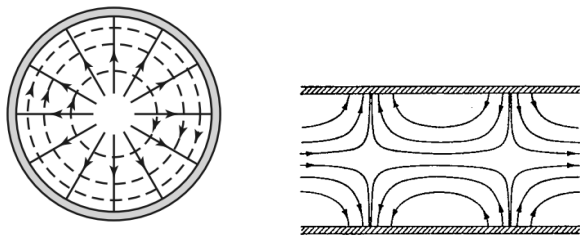

(a) (b)

Figure 3.3: Field plot illustrating electric (continuous lines) and magnetic field (dashed lines) of the mode TM_{01} in the circular waveguide. (a) The transverse plane from Pozar [32] and (b) Longitudinal plane from Marcuvitz [56].

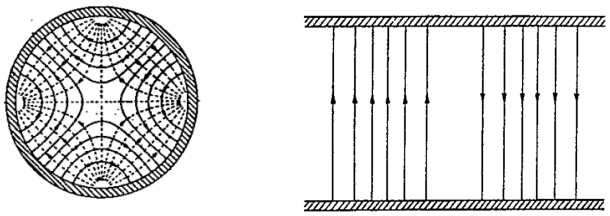

(a) (b)

Figure 3.4: Field plot of the illustrating electric (continuous lines) and magnetic field (dashed lines) of the TE_{21} mode in the circular waveguide from Marcuvitz [56]. (a) Tranverse plane and (b) Longitudinal plane.

3.2.3 Electric and Magnetic Field

The analytical expressions for the electromagnetic field for the TE_{mn} modes of a circular waveguide are given by [32], [56],

$$\begin{cases} E_\rho = \frac{-j\omega\mu m}{k_c^2\rho}\left(A\cos m\phi - B\sin m\phi\right) J_m(k_c\rho)e^{-j\beta z}, \\ E_\phi = \frac{j\omega\mu}{k_c}\left(A\sin m\phi + B\cos m\phi\right) J'_m(k_c\rho)e^{-j\beta z}, \\ E_z = 0, \end{cases} \tag{3.5}$$

Mode	Cut-off Frequency (GHz)
TE_{11}	1.26
TM_{01}	1.64
TE_{21}	2.09
TE_{01}	2.62
TM_{11}	2.62
TE_{31}	2.87

Table 3.2: Cut-off frequencies for the circular waveguide with radius 69.85 mm, until 3 GHz

$$\begin{cases} H_\rho = \frac{-j\beta}{k_c}\left(A\mathrm{sin}m\phi + B\mathrm{cos}m\phi\right) J'_m(k_c\rho)e^{-j\beta \mathrm{z}}, \\ H_\phi = \frac{-j\beta m}{k_c^2\rho}\left(A\mathrm{cos}m\phi - B\mathrm{sin}m\phi\right) J_m(k_c\rho)e^{-j\beta \mathrm{z}}, \\ H_\mathrm{z} = \left(A\mathrm{sin}m\phi + B\mathrm{cos}m\phi\right) J_m(k_c\rho)e^{-j\beta \mathrm{z}}. \end{cases} \tag{3.6}$$

On the other hand, the EM field components for the TM_{mn} modes are defined as,

$$\begin{cases} E_\rho = \frac{-j\beta}{k_c}\left(A\mathrm{sin}m\phi + B\mathrm{cos}m\phi\right) J'_m(k_c\rho)e^{-j\beta \mathrm{z}}, \\ E_\phi = \frac{-j\beta m}{k_c^2\rho}\left(A\mathrm{cos}m\phi - B\mathrm{sin}m\phi\right) J_m(k_c\rho)e^{-j\beta \mathrm{z}}, \\ E_\mathrm{z} = \left(A\mathrm{sin}m\phi + B\mathrm{cos}m\phi\right) J_m(k_c\rho)e^{-j\beta \mathrm{z}}, \end{cases} \tag{3.7}$$

$$\begin{cases} H_\rho = \frac{j\omega\epsilon m}{k_c^2\rho}\left(A\mathrm{cos}m\phi - B\mathrm{sin}m\phi\right) J_m(k_c\rho)e^{-j\beta \mathrm{z}}, \\ H_\phi = \frac{-j\omega\epsilon}{k_c}\left(A\mathrm{sin}m\phi + B\mathrm{cos}m\phi\right) J'_m(k_c\rho)e^{-j\beta \mathrm{z}}, \\ H_\mathrm{z} = 0. \end{cases} \tag{3.8}$$

Also, β is the phase propagation constant for the relevant mode. The constants A and B are defined from the boundary conditions of the solution of the Helmholtz wave equation in cylindrical coordinates. Thus, the cut-off wavenumber, in this case, is equal to

$$k_c = \frac{\chi'_{mn}}{r}, \tag{3.9}$$

for TE_{mn} modes and

$$k_c = \frac{\chi_{mn}}{r}, \tag{3.10}$$

for TM_{mn} modes.

The electric and the magnetic field lines of the three propagating modes TE_{11} (dominant), TM_{01}, and TE_{21} are illustrated in Fig. 3.2, 3.3, and 3.4, respectively, based on the bibliography [32], [56]. The plots can be described by the (3.5)-(3.8) which are referred in the circular waveguide. The knowledge of the electromagnetic field lines will help identify and define the propagated modes of the developed electromagnetic system of this study.

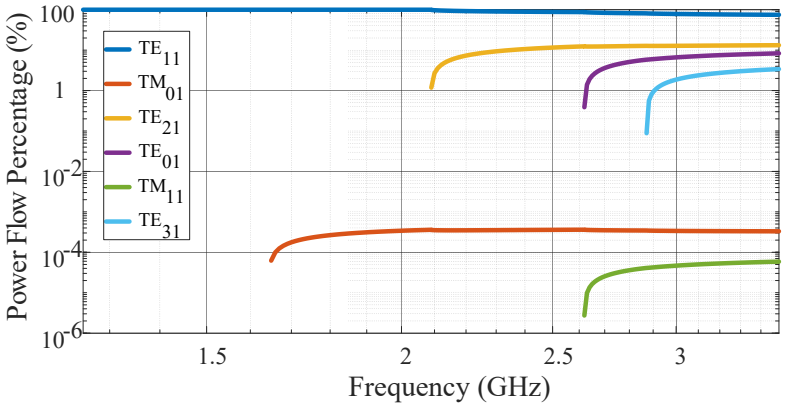

Figure 3.5: Numerically calculated percentage power flow for each mode with respect to frequency considering a pipeline having a radius of 69.85 mm.

3.2.4 Power Flow

The Poynting vector [32], $\mathbf{S} = \mathbf{E} \times \mathbf{H}^{\star}$, is used for the calculation of the power flow along the z-direction for the circular waveguide and it can be expressed as [32],

$$\begin{aligned} P_0 &= \frac{1}{2}\mathrm{Re}\int_{\rho=0}^{r}\int_{\phi=0}^{2\pi} \mathbf{E}\times\mathbf{H}^{\star}\cdot\hat{z}\rho\mathrm{d}\phi\mathrm{d}\rho \\ &= \frac{1}{2}\mathrm{Re}\int_{\rho=0}^{r}\int_{\phi=0}^{2\pi} \left(E_\rho H_\phi^{\star} - E_\phi H_\rho^{\star}\right)\rho\mathrm{d}\phi\mathrm{d}\rho, \end{aligned} \tag{3.11}$$

for each propagating mode. This parameter is essential to characterize the relative powers accepted by the pipeline at 2.4 GHz for the TE_{11}, TM_{01}, and TE_{21} modes. In particular, the power flow for the TE modes is given by

$$P_{0_{\mathrm{TE}}} = \frac{\pi\omega\mu\left(A^2+B^2\right)\mathrm{Re}(\beta)\chi_{mn}'^2\left(1-\frac{m^2}{\chi_{mn}'^2}\right)J_m^2(k_c r)}{4k_c^4}. \tag{3.12}$$

The power flow for the TM modes is also given by

$$P_{0_{\mathrm{TM}}} = \frac{\pi\omega\epsilon\left(A^2+B^2\right)\mathrm{Re}(\beta)}{2k_c^4}\left[\frac{\chi_{mn}^2}{2}J_m'^2(k_c r)\right]. \tag{3.13}$$

The derivations for (3.12) and (3.13) are following. General modal equations are defined for the circular waveguide starting from the analytical expressions for the possible electric field components within a circular metallic waveguide. In particular, [32] and [56] are expanding by introducing the complete sinusoidal components by the introduction of both boundary condition constants A and B. This treatment provides a complete analytical study for the power flow equations defining propagation within circular metallic pipes.

The power flow is defined as a function of the Poynting vector ($\mathbf{S}$) by the general expression $P_0 = \oint_{\mathbf{S}} \mathbf{S}\cdot\mathrm{d}\mathbf{s} = \oint_{\mathbf{S}} \mathbf{E}\times\mathbf{H}^{\star}\cdot\mathrm{d}\mathbf{s}$. For the circular waveguide, cylindrical

coordinates are adopted, and the power flow along the pipeline (z-direction) is given by (3.11). As already mentioned, the analytic expressions of the power flow for the TE and TM modes are given in (3.12) and in (3.13). The derivation of these equations follows.

Using the electromagnetic field expressions, (3.5) and (3.6), for the TE modes, and (3.7) and (3.8), for the TM modes, the power flow integrals for each case can be derived. The development of the power flow starts with the integral in (3.16) considering TE modes, and after some simplifications (3.17) is the result. In the derivation, the following trigonometric properties are employed:

$$\begin{cases} \sin 4\pi m = 0, \\ \cos 4\pi m = 1, \end{cases} \tag{3.14}$$

when, $m \in \mathbb{N}^*$ making the integral in (3.17) simplifying to (3.18). Then for solving the integral in (3.18), the following Bessel function integral property was used [32]:

$$\int_0^{\chi'_{mn}} \left[J'^2_m(x) + \frac{m^2}{x^2} J^2_m(x) \right] x \mathrm{d}x \;=\; \frac{\chi'^2_{mn}}{2} \left(1 - \frac{m^2}{\chi'^2_{mn}} \right) J^2_m(\chi'_{mn}), \tag{3.15}$$

finally ending with the power flow expression in (3.19) for each TE mode.

$$P_{0_{\mathrm{TE}_{mn}}} = \frac{1}{2}\mathrm{Re} \int_{\rho=0}^{r} \int_{\phi=0}^{2\pi} \left(E_\rho H^\star_\phi - E_\phi H^\star_\rho \right) \rho \mathrm{d}\phi \mathrm{d}\rho \tag{3.16}$$

$$= \frac{\omega\mu \mathrm{Re}(\beta)}{2k_c^4} \int_0^r \int_0^{2\pi} \left((A\cos m\phi - B\sin m\phi)^2 \frac{m^2}{\rho^2} J^2_m(k_c\rho) + k_c^2 (A\sin m\phi + B\cos m\phi)^2 J'^2_m(k_c\rho) \right) \rho \mathrm{d}\phi \mathrm{d}\rho$$

$$= \frac{\omega\mu \mathrm{Re}(\beta)}{2k_c^4} \left[\frac{4\pi m \left(A^2 + B^2\right) - 2AB + \left(A^2 - B^2\right) \sin 4\pi m + 2AB \cos 4\pi m}{4m} \int_0^r \frac{m^2}{\rho^2} J^2_m(k_c\rho) \rho \mathrm{d}\rho \right.$$

$$\left. + \frac{4\pi m \left(A^2 + B^2\right) + 2AB - \left(A^2 - B^2\right) \sin 4\pi m - 2AB \cos 4\pi m}{4m} \int_0^r k_c^2 J'^2_m(k_c\rho) \rho \mathrm{d}\rho \right] \tag{3.17}$$

$$= \frac{\pi\omega\mu \left(A^2 + B^2\right) \mathrm{Re}(\beta)}{2k_c^4} \int_0^r \left[\frac{m^2}{\rho^2} J^2_m(k_c\rho) + k_c^2 J'^2_m(k_c\rho) \right] \rho \mathrm{d}\rho \tag{3.18}$$

$$= \frac{\pi\omega\mu \left(A^2 + B^2\right) \mathrm{Re}(\beta)}{2k_c^4} \left[\frac{\chi'^2_{mn}}{2} \left(1 - \frac{m^2}{\chi'^2_{mn}} \right) J^2_m(k_c r) \right]. \tag{3.19}$$

On the other hand, the development of (3.21) for the TM modes uses the same procedure as outlined for the TE modes and concludes with (3.22). Also, for the solution of the integral in (3.22), the following Bessel function integral property was employed [32]:

$$\int_0^{\chi_{mn}} \left[J'^2_m(x) + \frac{m^2}{x^2} J^2_m(x) \right] x \mathrm{d}x \;=\; \frac{\chi^2_{mn}}{2} J^2_m(\chi'_{mn}), \tag{3.20}$$

finally arriving at the power flow expression in (3.23) for each TM mode.

$$P_{0_{\mathrm{TM}_{mn}}} = \frac{1}{2}\mathrm{Re} \int_{\rho=0}^{r} \int_{\phi=0}^{2\pi} \left(E_\rho H^\star_\phi - E_\phi H^\star_\rho \right) \rho \mathrm{d}\phi \mathrm{d}\rho \tag{3.21}$$

$$= \frac{\omega\epsilon \mathrm{Re}(\beta)}{2k_c^4} \pi \left(A^2 + B^2\right) \int_0^r \left[\frac{m^2}{\rho^2} J^2_m(k_c\rho) + k_c^2 J'^2_m(k_c\rho) \right] \rho \mathrm{d}\rho \tag{3.22}$$

$$= \frac{\pi\omega\epsilon \left(A^2 + B^2\right) \mathrm{Re}(\beta)}{2k_c^4} \left[\frac{\chi^2_{mn}}{2} J'^2_m(k_c\alpha) \right]. \tag{3.23}$$

The percentage power flow for each mode can also be calculated, knowing the radius of the circular waveguide and the number of excited modes. All possible cut-off frequencies are reported in Table 3.2 based on the numerical calculations until 3 GHz. Also, in Fig. 3.5, the analytically determined percentage power flow for each mode is reported with respect to frequency. It can be observed that the TE_{11} mode, which is the dominant mode, has the majority of the power for all the spectrum. Furthermore, the TE modes have much greater power flow than the TM modes. This happens because of the dependence of the TE and TM modes on the magnetic permeability and the electric permittivity, respectively, mainly because for the TE case, the value for the magnetic permeability is much lower than that of the electric permittivity.

Considering that the operational frequency for the proposed system is 2.4 GHz and that only three modes can be excited, percentage power flow ratios can be calculated as follows:

$$\begin{aligned} P_{0_{\mathrm{TE}_{11}}}\% &= \frac{P_{0_{\mathrm{TE}_{11}}}}{P_{0_{\mathrm{TE}_{11}}}+P_{0_{\mathrm{TM}_{01}}}+P_{0_{\mathrm{TE}_{21}}}}100\% \\ &= \frac{\frac{\pi\omega\mu\left(A^2+B^2\right)\mathrm{Re}(\beta_{11})}{2k_{c_{11}}^4}\left[\frac{\chi_{11}'^2}{2}\left(1-\frac{1}{\chi_{11}'^2}\right)J_1^2(\chi_{11}')\right]}{\frac{\pi\omega\left(A^2+B^2\right)}{2}\left[\frac{\mu\mathrm{Re}(\beta_{11})}{k_{c_{11}}^4}\frac{\chi_{11}'^2}{2}\left(1-\frac{1}{\chi_{11}'^2}\right)J_1^2(\chi_{11}')+\frac{\epsilon\mathrm{Re}(\beta_{01})}{k_{c_{01}}^4}\frac{\chi_{01}^2}{2}J_0'^2(\chi_{01})+\frac{\mu\mathrm{Re}(\beta_{21})}{k_{c_{21}}^4}\frac{\chi_{21}'^2}{2}\left(1-\frac{4}{\chi_{21}'^2}\right)J_2^2(\chi_{21}')\right]}100\% \\ &= 89.35\% \end{aligned} \tag{3.24}$$

$$\begin{aligned} P_{0_{\mathrm{TM}_{01}}}\% &= \frac{P_{0_{\mathrm{TM}_{01}}}}{P_{0_{\mathrm{TE}_{11}}}+P_{0_{\mathrm{TM}_{01}}}+P_{0_{\mathrm{TE}_{21}}}}100\% \\ &= \frac{\frac{\epsilon\mathrm{Re}(\beta_{01})}{k_{c_{01}}^4}\chi_{01}^2J_0'^2(\chi_{01})}{\frac{\mu\mathrm{Re}(\beta_{11})}{k_{c_{11}}^4}\chi_{11}'^2\left(1-\frac{1}{\chi_{11}'^2}\right)J_1^2(\chi_{11}')+\frac{\epsilon\mathrm{Re}(\beta_{01})}{k_{c_{01}}^4}\chi_{01}^2J_0'^2(\chi_{01})+\frac{\mu\mathrm{Re}(\beta_{21})}{k_{c_{21}}^4}\chi_{21}'^2\left(1-\frac{4}{\chi_{21}'^2}\right)J_2^2(\chi_{21}')}100\% \\ &\approx 0\% \end{aligned} \tag{3.25}$$

$$\begin{aligned} P_{0_{\mathrm{TE}_{21}}}\% &= \frac{P_{0_{\mathrm{TE}_{21}}}}{P_{0_{\mathrm{TE}_{11}}}+P_{0_{\mathrm{TM}_{01}}}+P_{0_{\mathrm{TE}_{21}}}}100\% \\ &= \frac{\frac{\mu\mathrm{Re}(\beta_{21})}{k_{c_{21}}^4}\chi_{21}'^2\left(1-\frac{4}{\chi_{21}'^2}\right)J_2^2(\chi_{21}')}{\frac{\mu\mathrm{Re}(\beta_{11})}{k_{c_{11}}^4}\chi_{11}'^2\left(1-\frac{1}{\chi_{11}'^2}\right)J_1^2(\chi_{11}')+\frac{\epsilon\mathrm{Re}(\beta_{01})}{k_{c_{01}}^4}\chi_{01}^2J_0'^2(\chi_{01})+\frac{\mu\mathrm{Re}(\beta_{21})}{k_{c_{21}}^4}\chi_{21}'^2\left(1-\frac{4}{\chi_{21}'^2}\right)J_2^2(\chi_{21}')}100\% \\ &= 10.65\% \end{aligned} \tag{3.26}$$

3.3 Half-Wave Dipole into the Circular Pipe

In the previous subsection presented how the classic waveguide theory applies to the selected circular pipe. However, it differs from the excitation method as it uses a half-wave dipole which is placed inside the waveguide (Fig. 3.11). An antenna is used instead of a vertical probe or loop feed because of the challenging environment of the oil and

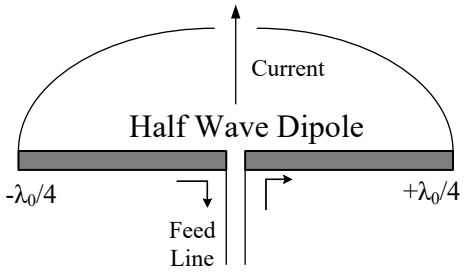

Figure 3.6: Half-Wave dipole structure. It consists of two conductors of equal length oriented end-to-end with the feedline connected between them [59].

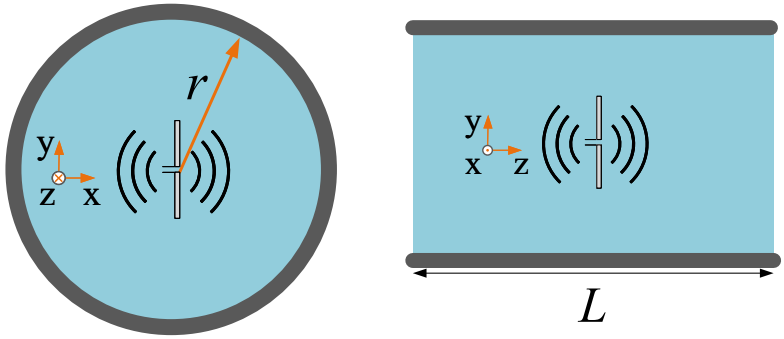

(a) (b)

Figure 3.7: Cross-section of the circular aluminium pipe which is representative of an oil and gas well pipeline. The half-wave dipole is illustrated and is placed vertically in the middle of the pipe enforcing signal propagation in the z-direction. a) Transverse plane (x-y plane). b) Longitudinal plane side view (y-z plane) as they are extracted by the simulated circular metallic waveguide.

gas pipe. For instance, antennas are employed in the proposed system because they can offer transceiver gains which route more power to the desired direction even in the enclosed pipeline environment. This excitation causes some complexity, and therefore, parameters such as the dipole effective gain and the transmission path loss (TPL) need to be carefully considered. Also, as further described herein, an antenna is more able to keep the waveguide/pipeline characteristics stable by enforcing excitation of the dominant mode (only) for propagation within the pipe. Also, the product which flows within the representative oil/gas well pipeline is assumed to be a typical methane mixture (in its dry gaseous phase) which has the electrical properties of air (see Subsection 2.4) [42].

3.3.1 Operation in Free Space and into the Pipe

The half-wave antenna consists of two parts, and each of them has a quarter-wavelength conductor (Fig. 3.6). In the operational frequency of 2.4 GHz, the dipole's total length is 60 mm ($\lambda_0/2$), and copper defines it.

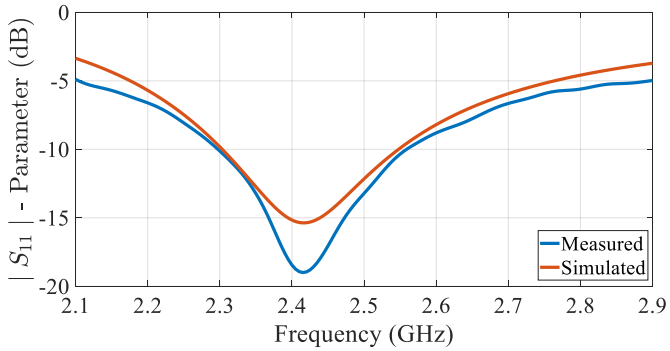

(a)

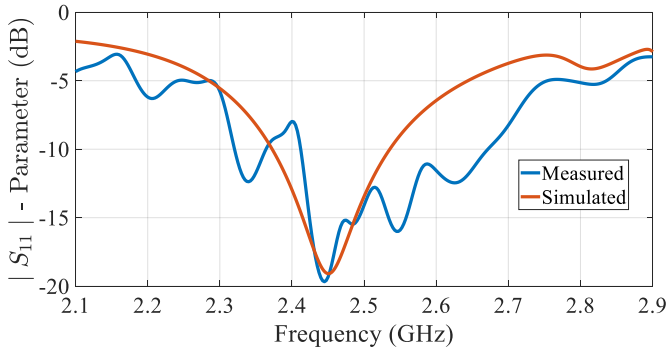

(b)

Figure 3.8: Simulated and measured reflection coefficient of the half-wave dipole when it is placed (a) in the free space and (b) into the pipe.

The reflection coefficient of the simulated and of the measured, manufactured dipole when it is placed in the free space is shown in Fig. 3.8a. It can be observed can the dipole operated efficiently from 2.3 GHz to 2.55 GHz. However, when the same dipole is placed inside the waveguide/pipeline (see Fig. 3.7), the reflection coefficient is shifted, and the dipoles are operated more efficiently around 2.5 GHz (see Fig. 3.8b). Because of this, the operational frequency is considered to be 2.5 GHz for the rest of the study. In theory, this does not change anything as the excited modes remain the same, plus their cut-off frequencies and attenuation constants differ insignificantly.

3.3.2 Effective Directivity

The directivity of the half-wave dipole in free space is 2.15 dB [59]; however, when placed in a circular metallic environment, the near radiating fields are apparent, altering the classic definition of transceiver gain. The antenna directivity is the effective antenna directivity because it cannot be directly described in the same way as the free-space directivity. Therefore, the effective directivity, which is also demonstrated in Figs. 3.9 and 3.10, is the directivity in which the CST Studio Suite EM simulation software provided findings in the +z-direction. This is defined as the forward path for signal propagation, i.e., along the pipeline. This is important when determining a link budget.

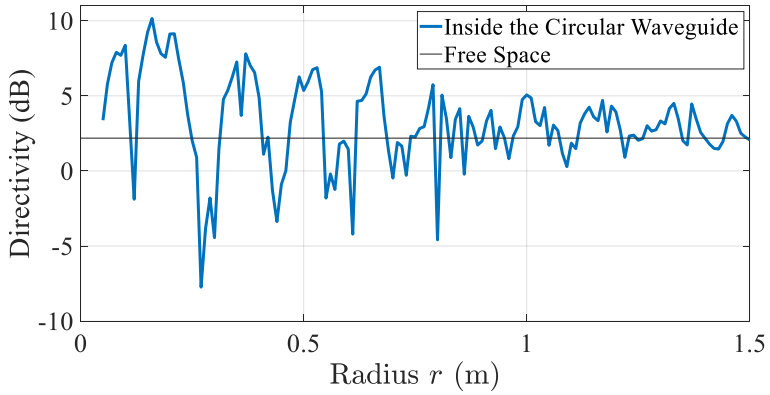

Figure 3.9: Simulated directivity of the half-wave dipole in the +z-direction, operating at 2.5 GHz with respect to the radius (r) of the circular aluminium waveguide, where it is operating within. A pipe length of a few wavelengths was employed whilst ensuring this length was representative of the conventional far-field range for the dipole. A comparison is also shown with the free-space directivity value (maximum); i.e. the 2.15 dB horizontal line.

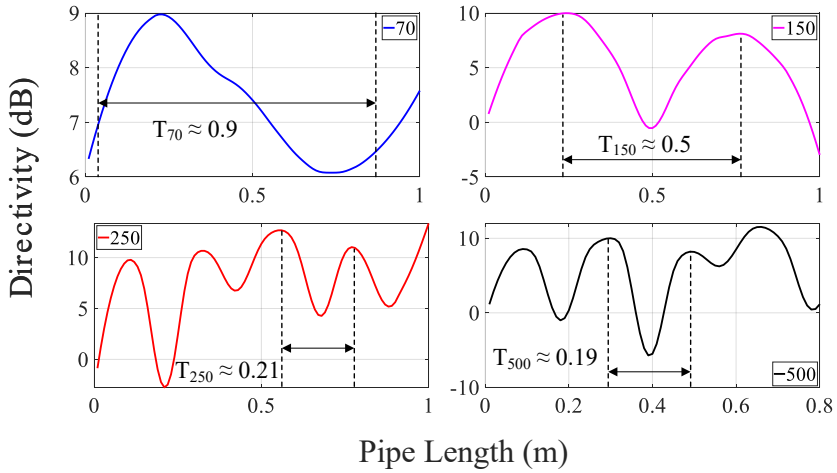

Figure 3.10: Simulated directivity of the half-wave dipole, operating at 2.5 GHz versus length, for various circular waveguides with radius 70, 150, 250, 500 mm. The observed period T is identified for each case.

Following this, the directivity of the half-wave dipole when placed inside a circular aluminium pipe (see Fig. 3.7a) was simulated, and the results are presented in Fig. 3.9. Starting with a radius (r) for the pipe of 50 mm, and gradually increasing this radial parameter (until it reached the far-field region), the directivity was recorded. As the radius of the pipe becomes more significant, the directivity approaches the free-space value of 2.15 dB.

More simulations were completed comparing the directivity of the half-wave dipole with respect to the length of the waveguide (L) and for various radii of the waveguide

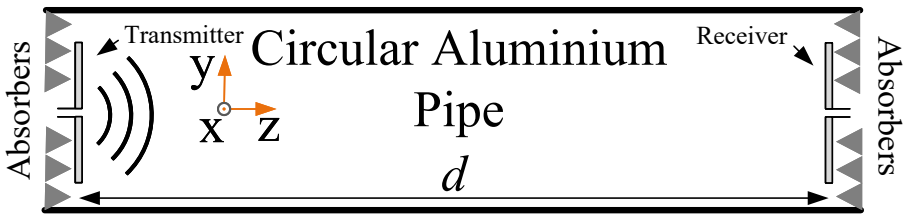

Figure 3.11: Setup for the wireless system showing the cross-section of the circular aluminium pipe, which is representative of an oil and gas well pipeline. The transceiver half-wave dipoles are illustrated, separated by a distance d, and placed vertically in the middle of the pipe, enforcing signal propagation in the +z-direction when the transmitter dipole is driven.

(Fig. 3.10). The half-wave dipole was placed at the edge of the waveguide as the length of the pipe was varied from 0 to 1 m. The directivity of the dipole was recorded for each of those lengths. Results suggest that the directivity is related to a periodic function linked to the dipole's omnidirectional-like radiation pattern. According to the results in Fig. 3.10 the value for the period T, which defines this periodic function, decreases as the radius of the waveguide increases. For example, as observed in Fig. 3.10 the period is about 900 mm and 190 mm for pipe diameters of 70 mm and 500 mm, respectively. On the other hand, the amplitude range of this function increases as the radius of the waveguide increases. The amplitudes are about 1.9, 5.5, 8.2, and 10.6 dB when the radius is 70, 150, 250, and 500 mm.

Considering all these investigations, it can be observed that the effective directivity, and therefore the effective gain of the half-wave dipole (when placed into a circular waveguide) is a function of the pipe radius and its length, i.e., $G_{eff}(r, L)$. This function cannot be easily defined in an exact form, as simulations have shown it relates to the pipe length and radius, L and r, respectively. For this reason, a simulation and measurement study follows, using the typical pipe dimensions as employed for commercial oil and gas wells.

3.3.3 Propagated Mode and Power Flow

An aluminium pipe of radius 69.85 mm (or $r \approx 0.6\lambda_0$) and wall thickness 10 mm ($t = 0.06\lambda_0$, at 2.5 GHz) was selected for further simulations and experimental testing. At the same time, the transmitter and the receiver dipoles were placed into the pipe as illustrated in Fig. 3.11. Based on waveguide theory (see 3.2.2), the dominant mode in a circular waveguide is the TE_{11} mode, while the TM_{01}, TE_{21} modes can be excited for propagation at 2.5 GHz [32] for the employed pipeline dimensions. This defines a multi-moded waveguide that is unwanted. The system was simulating by stimulating the dipole transmitter (see Fig. 3.11) with the pipe air-filled under lab conditions; the extracted electric field is that of the TE_{11} mode as reported in Fig. 3.12.

The power flow was extracted, also showing that the propagation is mainly routed in the z-direction (Fig. 3.13) while maintaining a maximum along the middle of the pipe. These simulation results are significant and identify that directive TE_{11} mode

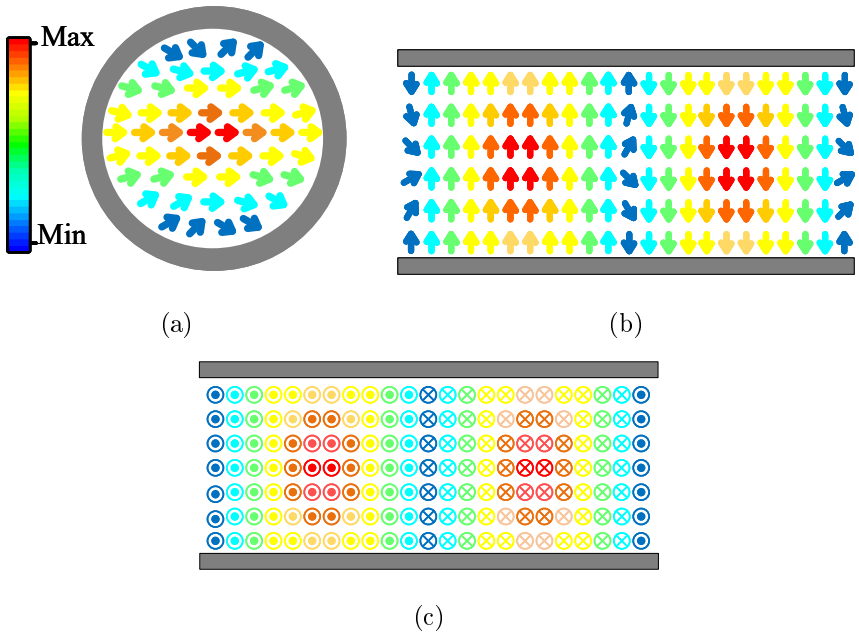

Figure 3.12: Electric field lines in the inner core. It can be observed that the propagating mode is the TE_{11} mode. (a) Transverse plane (x-y plane). (b) Longitudinal plane top view (x-z plane). c) Longitudinal plane side view (y-z plane) as they are extracted by the simulated circular metallic waveguide.

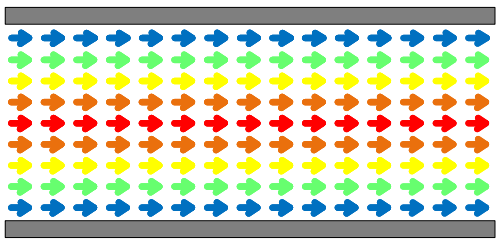

Figure 3.13: Simulated power flow lines for the TE_{11} mode within the circular metallic waveguide generated by the employed half-wave dipole source. The longitudinal plane or side view is shown; i.e. the y-z plane.

propagation is achieved for the experimental setup.

3.3.4 Transmission Path Loss

The transmission path loss TPL is defined in this work by studying the simulation and measurements of the system, and this path loss will be described in detail next. Specifically, maintaining a steady position for the transmitter dipole, the receiver dipole was gradually moved along the pipe, and the transmission loss was sampled at each position (see Fig. 3.11). The range of the distance (d) moved was from 700 mm to 860 mm. At each edge of the waveguide pipe, absorbing boundary conditions were imposed in the simulator so that no power was radiated outside the model. Similarly, during the

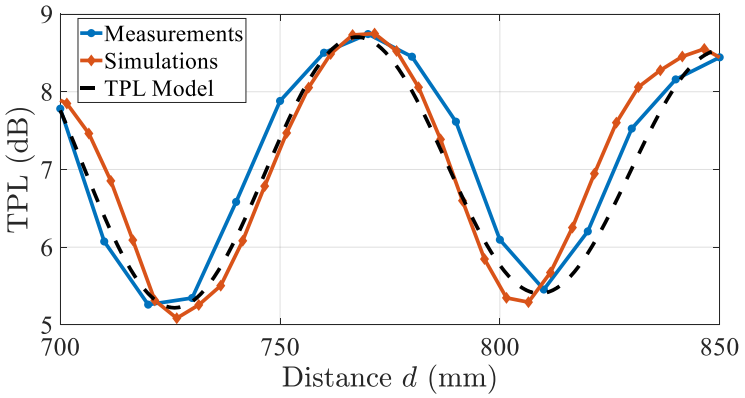

(a)

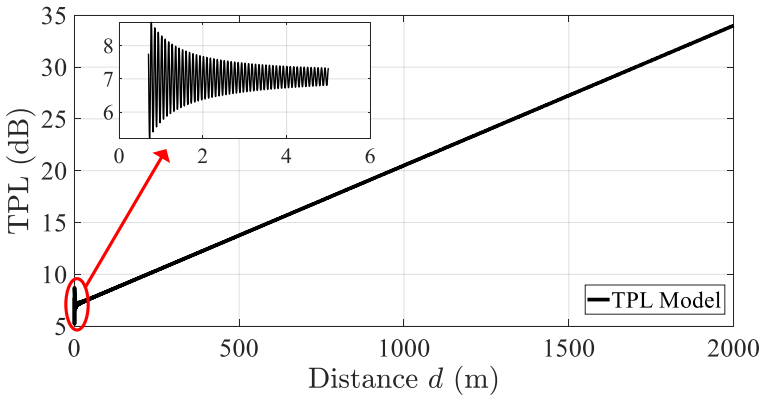

(b)

Figure 3.14: Transmission path loss (TPL) model. (a) Simulated, measured, and calculated TPL for the two dipole transceiver system when they are placed inside the waveguide. (b) Projection of the TPL model up to 2000 m. The inset focuses on distances up to 5 m.

measurements, a practical microwave absorber was positioned at the pipe edges, being well in the far-field zone of the antennas while following standard definitions.

The practical microwave absorbers had a dual purpose, as mentioned above. The first was to ensure that no power was diverted outside the pipes during the experiments and resemble the simulation model. Secondly, adding a microwave absorber helped emulate a more natural oil and gas scenario where the pipeline is longer. This enabled no reflections at the pipe edges. Also, the practical measurements and simulation studies made sure that the position of the microwave absorber and the appropriate absorbing boundary condition (in the simulator) as well in the far-field zone, ensuring minimal interaction between the absorber and antennas.

As observed in Fig. 3.14a there is a good agreement between the CST Studio Suite EM simulation software and the measurements. A numerical model was then developed and plotted (see Fig. 3.14b) as described by (3.27) and is a function of the sys-

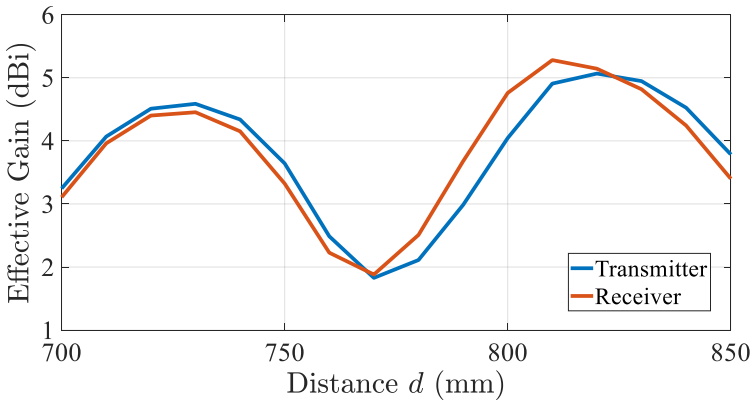

Figure 3.15: Effective gain of the transceivers based on the measured impulse response of the dipoles which were placed inside the aluminium pipe.

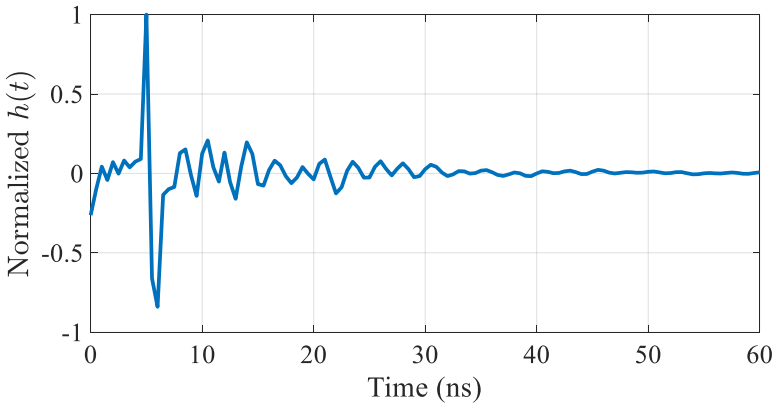

Figure 3.16: Measured impulse response of the dipoles which were placed inside the aluminium pipe in 700 mm distance.

tem losses (SL) and the realized effective gain of the transmitter and receiver antennas (G_{eff_t}, G_{eff_r}). The SL includes the power directed in the backward direction, power loss at the antenna receiver, and the loss due to the conductivity of the pipeline walls. Given these conditions, the TPL can be defined in dB:

$$\text{TPL} \quad = \quad \text{SL}(r, L) + G_{eff_t}(r, L) + G_{eff_r}(r, L). \tag{3.27}$$

From the measurements and the simulations, it can also be extracted that the sum of the SL and the effective dipole gains and, therefore, the TPL is given by

$$\text{TPL} \quad = \quad P + \alpha \times d + \frac{A}{d} \sin\left(\frac{2\pi d}{T}\right) \text{ dB}. \tag{3.28}$$

The radius, in this case, is steady, and the constant values P and α are dependent on the radius. Moreover, by inspection of the simulations and measurements in Fig.

3.14 the values of the constants P and α are 7 and 0.013505, respectively. The constant A is referred the amplitude of the periodic function, and its value is 1.8 dB, while the period is about 80 mm for this specific pipe diameter.

The oscillation in the TPL model for the dipole sources can be explained by the near fields generated by the dipole with respect to the driven waveguide. The periodic function and thus the oscillation declines as long as the distance between the dipoles increases. Thus the TPL model has a more linear form, as is demonstrated in Fig. 3.14b about the TPL projection for distances up to 2000 meters.

After some further investigations in the simulator, it was found that the aforementioned periodic function, $\frac{A}{d}\sin\left(\frac{2\pi}{T}d\right)$, is related to the omnidirectional-like radiation pattern of the half-wave dipole. This was realized because in other simulation and measurement studies, with a more directive end-fire antenna placed at the pipe edges, the power was more simply injected into the waveguide, and this periodic function did not appear (see Subsection 4.4.4).

3.3.5 Impulse Response and Effective Gain

This investigation mentioned above helps further understand the effective gains of the half-wave dipoles when placed inside the pipe. Also, an analytical expression to characterize the realized effective gain can be provided through the impulse response $h(t)$. Connecting the transceiver antennas to the 2-Port vector network analyzer (VNA), the complex transmission coefficients S_{21} and S_{12} were measured. The 50 Ohm 2-port, 20 kHz to 4.8 GHz S5048 VNA by Copper Mountain Technologies with a noise floor of -125 dBm/Hz was used for the measurements. The Fourier transform of the normalised impulse response ($H_N(\omega)$) using transmission coefficients [60] is

$$H_N(\omega) = \sqrt{\frac{d\, v_g}{j\omega} S_{21}(\omega) e^{j\omega\frac{d}{v_g}}}, \tag{3.29}$$

where v_g is the group velocity of the propagated mode. Also, the relation between the gain of the transmitter and the impulse response of the antenna is given by [61]

$$G_t(\omega) = \frac{4\pi}{\lambda_g^2} \mid H_N(\omega) \mid^2, \tag{3.30}$$

where λ_g is the wavelength of the propagated mode. Respectively, the gain of the receiver is given by the use of $S_{12}(\omega)$ instead of $S_{21}(\omega)$. It should also be mentioned that (3.29) and (3.30) have been recast from [60] and [61] considering the group velocity v_g and the guided wavelength λ_g, respectively, instead of the speed of light c and the free-space wavelength λ_0. The group velocity and the wavelength of the TE_{11} mode in the circular pipe with a 69.85 mm radius at 2.5 GHz are 2.59×10^8 m/s and 0.139 m, respectively.

The S-parameters were measured when reviewing the measurements with the aluminium pipe (having a 69.85 mm radius) and placing the two half-wave dipoles at both ends of the pipeline. Therefore, based on (3.30), the gains of the transmitter and the receiver dipoles inside the circular waveguide were calculated as reported in Fig. 3.15 with respect to the distance at 2.5 GHz. Also, the impulse response of the system when

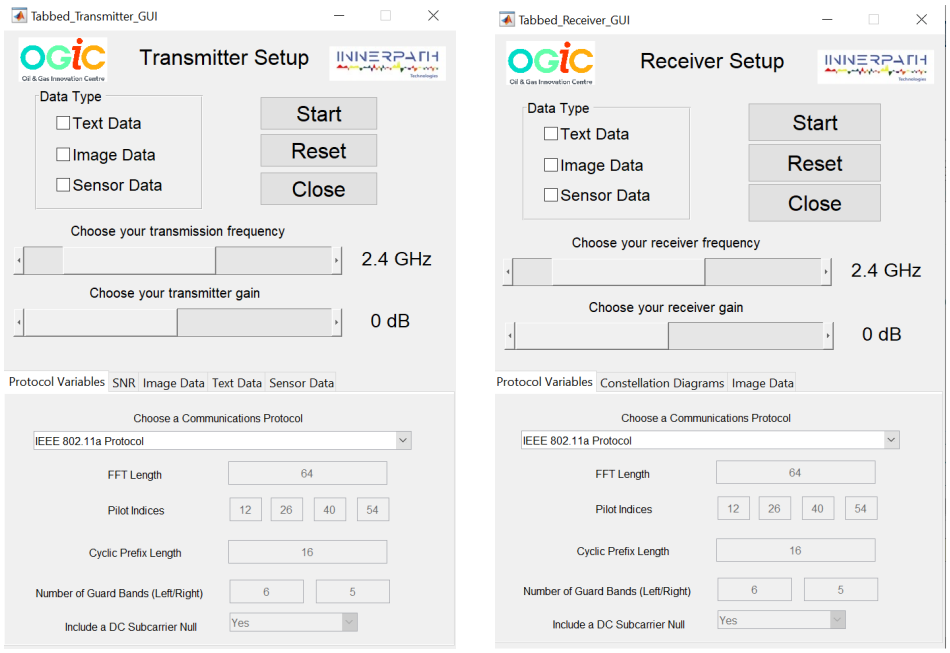

Figure 3.17: Graphical user interface (GUI) of the data communication system showing the available configuration settings for the receiver USRP. Transmitter (left) and receiver (right) tabs.

the distance was 700 mm, is shown in Fig. 3.16. It can be observed that the values of those gains (determined using the impulse response) follow a periodic function. This means that when the gains increase, the losses decrease. These findings also provide some justification that the noted periodicity, as well as the dipole directivity and effective gain, are related to fields generated for a particular pipe radius and length, i.e., $G_{eff}(r, L)$ as previously discussed.

3.4 Sensory Data Transmission Through the Pipe

An RF wireless system from an electromagnetic point of view was studied in the previous sections. Furthermore, this setup was used to establish the data communication system. This system includes two N210 universal software radio peripherals (USRP) modems by National Instruments, defining the transmitter and receiver hardware for data communications, a barometric pressure/temperature (BMP180) sensor by Bosch, and an Arduino (ATmega328P) microcontroller board. The default transmitted power of the USRP is -25 dBm which can be re-programmed for a possible total power increase of about 30 dB. Also, the noise floor of the USRP was measured at -90 dBm.

A graphical user interface (GUI) was built in Simulink and Matlab to control those parameters better. Fig. 3.17 illustrates this GUI and shows the choices of the user. The communications system was programmed by OFDM modulation to send data continuously or as a single transmission test for real-time monitoring. Also, the BPSK

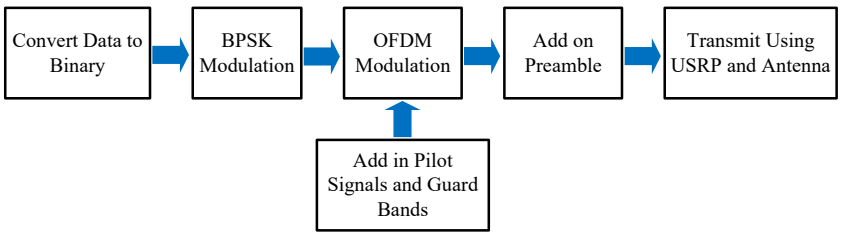

(a) Transmitter Flow Diagram

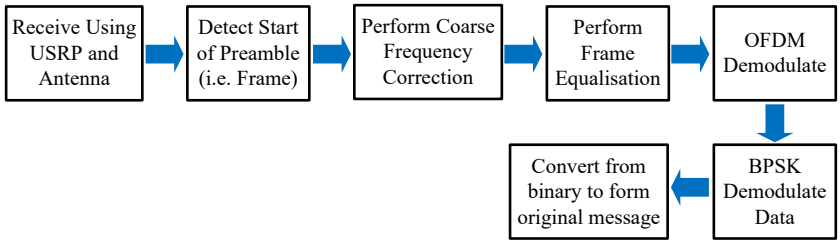

(b) Receiver Flow Diagram

Figure 3.18: Flow diagram of the Simulink data transmission and reception system using OFDM and BPSK modulation schemes.

modulation technique was used. A summary of those schemes has been given in the Section 2.5.3. In the GUI the user can choose the standards for the OFDM protocol (see Fig. 3.17). In the Fig. 3.18 the flow diagram for the Simulink data transmission and reception systems, using the aforementioned modulation schemes, is shown.

Additionally, the user can change the gains of the USRPs and the transmitting data (image, pressure, and temperature). Furthermore, during the transmission, the user is able to watch the constellation diagram on the monitor of the receiver side. The system was programmed in such a way that the data was re-sent repeatedly until the user decided to stop the transmission. This helps with real-time monitoring of the system while the user chooses when to receive the data.

3.4.1 Structure of the System

In Fig. 3.19 is illustrated the experimental and the block diagram of the setup that was built and tested within an anechoic chamber for the RF wireless data communication system. The half-wave dipole was placed at the edge of the circular aluminium pipe and connected in series with the USRP modem. Also, the barometric pressure/temperature (BMP180) sensor was connected to the input of the Arduino microcontroller board to allow the measurement and recording of the ambient temperature and pressure around the pipe. The setup above describes the arrangement of the transmitter side, which was positioned at a distance of $d = 850$ mm from the receiver. At the receiver side, the half-wave dipole was connected to the USRP.

The chosen OFDM protocol with the BPSK modulation is the IEEE 802a.11. The characteristics of this protocol include the fast Fourier transform (FFT) length, the pilot indices, the cyclic prefix length, the number of guard bands (Left/Right), and the DC

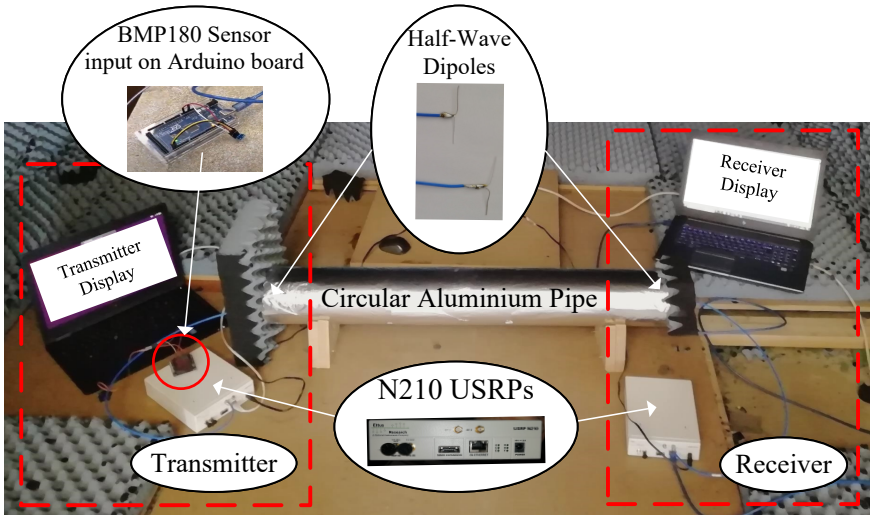

(a)

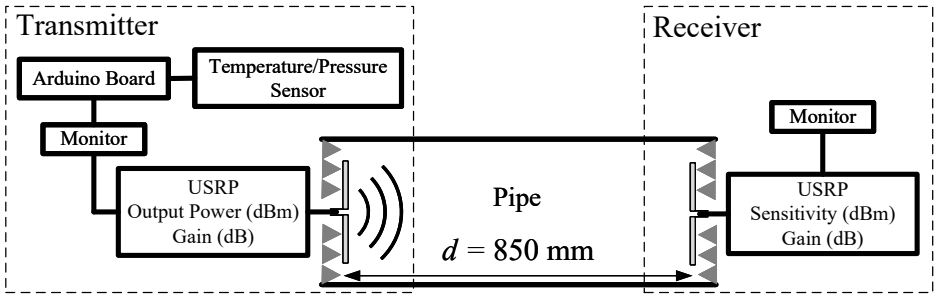

(b)

Figure 3.19: (a) Experimental and (b) Block diagram setup of the channel. The dipoles were placed at each end of the circular aluminium pipe and connected to the USPRs. On the transmitter side, the BMP180 sensor was connected to the Arduino board capturing the environmental data. The receiver accurately decoded the sensor data in real-time. At the edges of the pipe, a microwave absorber was positioned to contain power flow inside the pipeline.

subcarrier null. The values of these characteristics are shown in the Fig. 3.17.

3.4.2 Sensory Data Transmission

In a simple experiment, the transmitted power of the USRP was -25 dBm, and no additional gain nor amplifiers were applied to the transceiver. Based on Fig. 3.14a, the measured transmission loss was $\approx$ 8 dB, and the received power was calculated to be -33 dBm. The testing of the communications link was successful, as the sensory data was received and monitored accurately in real-time. The temperature that appeared on display was 28.06 °C, and the pressure was 102.2 kPa. A hot air blower was set next to the sensor in a subsequent test, and the temperature rise was monitored. A measurement increase in temperature from 28.06 °C to 31.79 °C was observed and

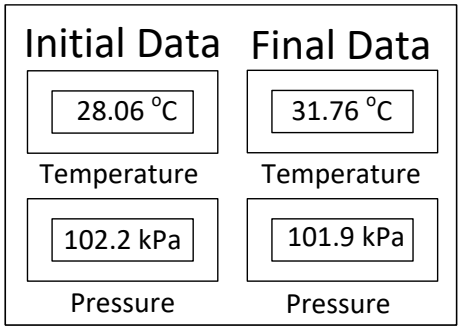

Figure 3.20: Tabulated initial and final temperature and pressure data, which were accurately transmitted through the pipe. The initial data refers to the environmental temperature and pressure at the beginning of the test. The final data is recorded when the sensor's heat source is placed next. The user was able to monitor the temperature change in real-time continuously.

verified with a digital thermometer. The atmospheric pressure was monitored at 101.9 kPa (see Fig. 3.20).

3.5 Summary

A wireless communication system was introduced for propagation inside an oil and gas well pipeline. The excited modes, the conductor losses, the electric and magnetic fields, and the power flow along a commercially available pipeline were analyzed.

By following classic metallic waveguide analysis and antenna theory, parameters such as the dominant TE_{11} mode, the TPL model, and the effective dipole directivity and gain were studied to estimate the propagating signal strength between the dipole transceivers. Sensory data such as temperature and pressure were successfully transmitted and monitored in real-time, using OFDM and software defined radios, i.e., USRPs at the transmitter and the receiver for a 2.5 GHz ISM band carrier frequency. Furthermore, a hot air blower was used to increase the air temperature around the sensor at the transmitter side. The system monitored the temperature changes accurately and provided an updated display of information to the user in real-time. It is clear from the results that an antenna-driven communication system is feasible in an oil and gas pipeline environment. However, a more advanced system is presented in the next chapter to overcome the limitations such as the antenna positioning, the possible transmission range, or the transmission of image and video data.

Chapter 4

Controlled Propagation within Oil and Gas Pipelines using Directive Antennas

4.1 Introduction

The modelling and design of a communication system are examined in this chapter, where the signal propagates within a circular metallic pipeline (see Fig. 4.1) using directive PCB-based antennas. This study is oriented to more realistic parameters such as corroded pipelines, mechanical housing for the antenna, and a more extensive field trial study (with longer pipes) when compared to the previous chapter. For experimental development and testing, the transmitter and the receiver antennas were initially placed inside the inner core at its edges and then in an enclosed mechanical housing for antenna and electronic circuit protection. A low-cost PCB-based antenna was employed since a directive source is required to support propagation down the pipeline. Also, a directive antenna feed helps to keep the pipeline (or waveguide) propagation characteristics stable and controlled while also allowing for placement within the pipeline sub-surface. Also, as further discussed in this chapter, the directive antenna enforces excitation of the dominant mode *only* in the pipeline.

This is not easy to achieve because the selected 2.4 GHz carrier frequency signal, is required to propagate within a multi-moded waveguide since industry standard pipeline dimensions are employed. However, reduced carrier frequencies are possible, but larger transducers would be required, which is not practical within industry pipelines as compact, low-profile, and low-cost equipment is needed. It should also be stressed that this pipeline propagation scenario defines an intricate and challenging EM engineering problem, requiring clever system design, mainly to ensure efficient data transmission within working pipeline conditions of high temperatures and pressures due to the gaseous flow (see Subsection 2.4). This is in contrast to more conventional microwave systems, which generally strive for dominant and unimodal excitation within metallic waveguides while possibly considering more high-power scenarios and shorter transmission line lengths. The motivation for the reported antenna-driven system is to efficiently transmit data within the enclosed overmoded metallic pipe at 2.4 GHz. As described in the chapter, sensory data (such as temperature and pressure) is accurately transmitted and received as digital images and videos.

The chapter is divided into three parts. The first part reports on such a circular metallic waveguide and its characteristics, including the relevant dimensions and some crucial factors, such as metallic properties and corrosion, which can alter the electro-

Figure 4.1: Full length of the inner core set up. Signal propagation tests took place considering different pipeline sections as well as the full length of this inner core (36.03 meters). In the inset, the radius ($r = 69.85$ mm) and the wall thickness ($t = 10$ mm) of the circular pipe are shown.

magnetic propagation inside the guide. Also, some numerical results of the conductor losses for the excited modes are reported, compared with the CST Studio Suite EM simulation software for various cases, and the results agree. This information is essential when defining the aforementioned link budget equation in Subsection 4.3.5. In particular, the examined cases are divided into the following categories: type of metal, waveguide radius, and the relative permittivity of the material within the pipe. Also, due to the magnetic properties of carbon steel 1010 (which is a common material for oil and gas pipelines [62]), a short study of the relationship between the attenuation constant of the dominant mode with the relative permeability is documented.

In the second part of the chapter, system operation at 2.4 GHz is further defined and studied using an end-fire microstrip-based planar antenna that directs EM waves into the inner core. A mechanical manufactured antenna housing is then introduced to protect the antenna itself and the supporting electronic circuits from oil and gas product flow and the potentially high temperatures and pressures. This antenna housing is placed on a 2-meter section of the inner core, defining a conventional mandrel configuration employed within oil and gas wells. As outlined in Section 4.4 the propagating mode, the transmission path loss, the impulse response, and the effective antenna gains are also all defined.

System testing is presented in the third part of the chapter. In particular, the transmission and the monitoring in real-time of sensory data such as temperature/pressure, digital images, and videos are outlined in Section 4.5. This system includes two N210 USRP modems, defining the transmitter and receiver hardware for data communications. Some commercially available high gain and low noise LNA amplifiers were also employed as well as barometric pressure/temperature sensors. These sensors were connected to an Arduino microcontroller for data transfer to the USRPs. Also, OFDM was selected for data communications for its multi-path mitigation properties, resistance to

Element	Content(%)
Iron, Fe	99.18-99.62
Manganese, Mn	0.30-0.60
Sulfur, S	≤ 0.050
Phosphorous, P	≤ 0.040
Carbon, C	0.080-0.13

Table 4.1: Chemical composition of the AISI 1010 carbon steel [65]

fading for long distance communications, and suppression of inter-symbol interference (ISI) [63]. In the inter-symbol interference (ISI) of a signal one symbol interferes with subsequent symbols, creating a signal distortion. In particular, when a pulse spreads beyond its allotted time interval, this can cause interference with neighbouring pulses. This can cause unreliable communication as the previous symbols have a similar effect as noise [64]. The ISI is very common in multipath (or multi-moded) environments such as the oil and gas pipeline. For this reason, the selection of OFDM was essential for ensuring good system operation.

Matlab/Simulink and LabVIEW were used for the coding development. Also, in some trials, additive white Gaussian noise (AWGN) was transmitted with the signal for testing purposes. This altered the signal-to-noise ratio (SNR) at the pipe receiver, which, for development purposes, was controlled by the user. Finally, the limitations in terms of minimum received power for data communications and the controlled SNR of the system are reported.

4.2 Pipeline Selection and Characteristics

The selected inner core belongs to the typical pipelines for a commercial downhole well. The radius (r) of the chosen inner core is 69.85 mm (or $0.525\lambda_0$ at 2.4 GHz) and wall thickness $t = 10$ mm (or $0.08\lambda_0$ at 2.4 GHz) (see inset of Fig. 4.1), i.e., same dimensions for the pipe that was used in the previous chapter. The wall material is the AISI 1010 carbon steel, which can be described by its chemical composition (see Table 4.1) [65]; i.e. the electrical conductivity (σ) and the relative magnetic permeability (μ_r) of carbon steel 1010 is 6.993×10^6 S/m and 100, respectively [66], [67].

The challenging operational environmental, geological conditions and the aging of the pipeline could also cause some corrosion in the interior of the metallic pipe. The main element of carbon steel 1010 is iron (over 99%), and there are a couple of ways that iron reacts with oxygen. The most common reaction is $3Fe + 2O_2 \rightarrow Fe_3O_4$. The compound, iron (II, III) oxide, also called ferrous ferric oxide, is dark brown/black. The EM properties of ferrous ferric oxide are described in Table 4.2. More information can be found in [68] and [69]. These details are important, and as further discussed in the following, this layer of rust can be induced in the inner core and can introduce extra losses at RF/microwave frequencies.

Conductivity (S/m) at 300 K	25000
μ_r	1.0072
ϵ_r	14.2
Density (kg/m^3)	5000

Table 4.2: Electromagnetic properties of ferrous ferric oxide

Mode	Cut-off Frequency (GHz)		α_c (dB/m) Aluminum Walls		α_c (dB/m) Steel 1010 Walls	
	Theory	Simulation	Theory	Simulation	Theory	Simulation
TE_{11}	1.257	1.257	0.0043	0.0043	0.0988	0.0989
TM_{01}	1.642	1.643	0.0073	0.0073	0.1666	0.1667
TE_{21}	2.086	2.084	0.0164	0.0163	0.3710	0.3692

Table 4.3: $r = 69.85$ mm, $\epsilon_r = 1$

Mode	Cut-off Frequency (GHz)		α_c (dB/m) Aluminum Walls		α_c (dB/m) Steel 1010 Walls	
	Theory	Simulation	Theory	Simulation	Theory	Simulation
TE_{11}	1.027	1.026	0.0043	0.0043	0.0990	0.0991
TM_{01}	1.342	1.341	0.0079	0.0079	0.1793	0.1796
TE_{21}	1.704	1.703	0.0117	0.0117	0.2651	0.2650
TE_{01}	2.138	2.137	0.0115	0.0115	0.2601	0.2587
TM_{11}	2.138	2.137	0.0145	0.0144	0.3276	0.3268
TE_{31}	2.344	2.343	0.0616	0.0607	1.3909	1.3559

Table 4.4: $r = 69.85$ mm, $\epsilon_r = 1.5$

Mode	Cut-off Frequency (GHz)		α_c (dB/m) Aluminum Walls		α_c (dB/m) Steel 1010 Walls	
	Theory	Simulation	Theory	Simulation	Theory	Simulation
TE_{11}	0.889	0.889	0.0045	0.0045	0.1027	0.1030
TM_{01}	1.162	1.161	0.0086	0.0087	0.1962	0.1967
TE_{21}	1.476	1.475	0.0108	0.0108	0.2458	0.2460
TE_{01}	1.852	1.850	0.0071	0.0082	0.1607	0.1603
TM_{11}	1.852	1.850	0.0119	0.0118	0.2699	0.2699
TE_{31}	2.030	2.029	0.0250	0.0250	0.5657	0.5644

Table 4.5: $r = 69.85$ mm, $\epsilon_r = 2$

4.2.1 Mode Analysis and Conductor Losses

Equations (3.1) to (3.4) presented the cut-off frequencies and the attenuation constants due to the conductivity of the metal for the circular metallic waveguide. Some numerical calculations using these developed equations are compared with CST Studio Suite EM simulation software. for some relevant cases. These cases are as follows: (i) the type of metal for the circular waveguide (aluminium or carbon steel 1010), (ii) the radius of the

Mode	Cut-off Frequency (GHz)		α_c (dB/m) Aluminum Walls		α_c (dB/m) Steel 1010 Walls	
	Theory	Simulation	Theory	Simulation	Theory	Simulation
TE_{11}	1.537	1.535	0.0071	0.0071	0.1603	0.1601
TM_{01}	2.007	2.006	0.0120	0.0120	0.2712	0.2709

Table 4.6: $r = 57.15$ mm, $\epsilon_r = 1$

Mode	Cut-off Frequency (GHz)		α_c (dB/m) Aluminum Walls		α_c (dB/m) Steel 1010 Walls	
	Theory	Simulation	Theory	Simulation	Theory	Simulation
TE_{11}	1.255	1.255	0.0065	0.0065	0.1476	0.1477
TM_{01}	1.640	1.639	0.0110	0.0110	0.2489	0.2492
TE_{21}	2.083	2.081	0.0244	0.0243	0.5507	0.5484

Table 4.7: $r = 57.15$ mm, $\epsilon_r = 1.5$

Mode	Cut-off Frequency (GHz)		α_c (dB/m) Aluminum Walls		α_c (dB/m) Steel 1010 Walls	
	Theory	Simulation	Theory	Simulation	Theory	Simulation
TE_{11}	1.087	1.086	0.0065	0.0065	0.1468	0.1470
TM_{01}	1.420	1.411	0.0115	0.0115	0.2603	0.2608
TE_{21}	1.804	1.802	0.0185	0.0185	0.4188	0.4183
TE_{01}	2.263	2.262	0.0248	0.0247	0.5618	0.5562
TM_{11}	2.263	2.262	0.0279	0.0278	0.6315	0.6272

Table 4.8: $r = 57.15$ mm, $\epsilon_r = 2$

circular waveguide (57.15 mm and 69.85 mm), and (iii) the relative permittivity of the filling material ($\epsilon_r = 1, 1.5, 2$) for the waveguide. As described earlier in Subsection 2.4, the pipeline waveguide could be filled in practice with gaseous crude (such as natural gas) at different temperatures and pressures, making its electrical properties slightly different from air [40], [42]. These studies are important for the EM engineer to understand the possible losses and changes in electrical properties while considering the different practical cases for natural gas and the industry standard pipelines.

The electrical conductivity for aluminium is 3.56×10^7 S/m [32] and 6.993×10^6 S/m for carbon steel 1010 [67]. Also, carbon steel 1010 has magnetic properties with its relative magnetic permeability (μ_r) equal to 100 [66]. Due to these magnetic characteristics, a short study is presented next where the relationship between the attenuation constant of the TE_{11} dominant mode for the circular waveguide defined by carbon steel 1010 having a radius, r, of 69.85 mm.

Numerical results are compared with the CST Studio Suite EM simulation software (see Fig. 4.2 and Tables 4.3 to 4.8). As can be observed, a good agreement is achieved between the calculations and the simulations. These characteristics studied, which include the type of metallic walls and their radius as well as the relative permittivity and permeability, are typical and possible values that could be observed in practical oil and gas well systems [40].

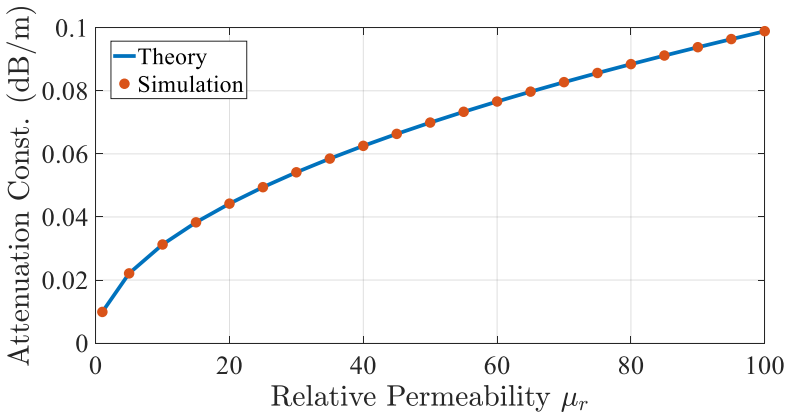

Figure 4.2: Attenuation constant of the TE_{11} mode as compared to different values for the relative permeability (from 1 to 100). This range depends on the iron content for the waveguide metal, and thus defines different possibilities for practical steel pipelines [65].

Mode	α_c (dB/m) Steel 1010	α_r (dB/m) Ferrous Ferric Oxide
TE_{11}	0.0989	0.166
TM_{01}	0.1666	0.280
TE_{21}	0.3710	0.623

Table 4.9: Conductor losses for the propagating modes of the circular waveguide with r = 69.85 mm, calculated at 2.4 GHz

For the presented theoretical calculations, the CST Studio Suite EM simulations as well as the measurements, in this study, the filling material inside the pipeline was considered to be air [42], i.e., the relative permittivity (ϵ_r) and permeability (μ_r) was taken equal to 1. Also, the metallic walls are made from carbon steel 1010, and the metal guide can experience rust (also known as ferrous ferric oxide). Given these conditions, the attenuation constants for all the possible modes at 2.4 GHz; i.e., the TE_{11}, TM_{01} and the TE_{21} modes are reported in Table 4.9.

4.3 PCB Yagi-Uda Antenna into the Circular Waveguide

This section studies the pipeline when a directive end-fire antenna is employed as the transceiver. The parameters analysed here are the propagating mode, the power flow, and the transmission path loss (TPL) inside the inner core. Also, the antenna's performance (i.e., its directivity and IEEE gain) in this enclosed environment is examined. At the end of the section, a link budget equation is developed with respect to the signal transmission length.

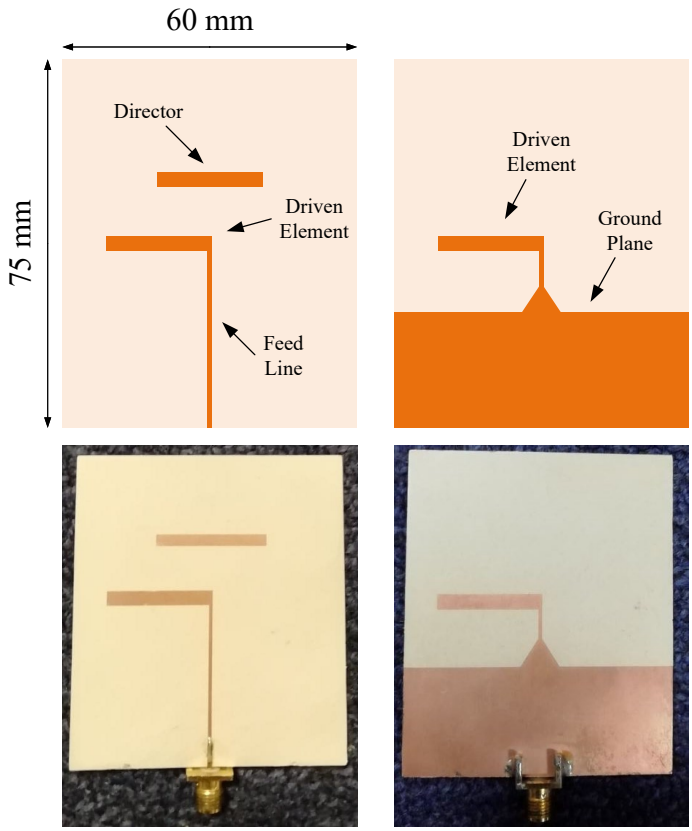

Figure 4.3: Microstrip based end-fire Yagi-Uda antenna structure. Top and bottom views of the schematic and the manufactured antenna are shown.

4.3.1 Antenna Selection

The selection of the proper antenna for directive field propagation inside the pipeline is important for the operation of the proposed transmission system. Most importantly, the antenna must fit inside the concentric metallic waveguide arrangement and into the mechanical housing that is being designed for it and, at the same time, operate effectively at 2.4 GHz. A compact planar Yagi-Uda PCB based antenna was designed and optimized using the CST Studio Suite EM simulation software for the aforesaid reasons.

The antenna (Fig. 4.3) is a microstrip-based or planar end-fire Yagi-Uda, and it consists of the feed line, the driven element, the director, and the ground plane. The driven element is the dipole antenna printed on both sides of the substrate. The feeding line is a microstrip transmission line of 50 Ω which is printed on the top side, and a ground plane is printed on the bottom side [70]. All the contents except for the substrate are made of copper with a thickness of 35 μm.

The primary resonance of the antenna mainly controls the driven element, and it affects the matching performance. On the other hand, the director is a parasitic stripline coupled to the driven element. It leads the antenna to radiate in the forward direction.

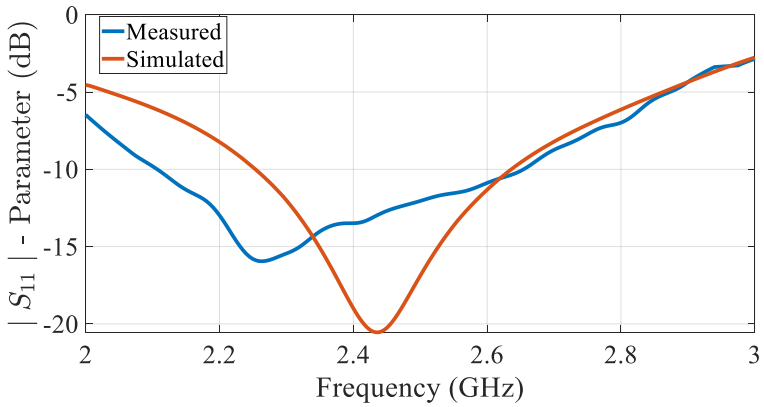

Figure 4.4: Simulated and measured reflection coefficient of the microstrip based end-fire Yagi-Uda antenna.

Also, the geometry of the structure is fundamental. The director must be shorter than the driven element in terms of length. In addition, the distance between the two elements affects the matching bandwidth of the antenna, and the directivity [70]. The distance between the driven element and the director was 10.35 mm. The substrate is Rogers RT6010 with a relative dielectric constant of $\epsilon_r = 10.2$, a loss tangent of $\tan\delta = 0.0023$ and its thickness is 1.27 mm, and the major PCB dimensions are 75 mm $\times$ 60 mm. This PCB material is typically employed for space applications, such as CubeSats as in [71]–[73], and also, is suitably rated for the temperature variations within oil and gas well pipelines.

It should be mentioned that the antenna can maintain a gain higher than 6 dBi in a free-space environment and the front to back ratio is close to 19 dB. The advantage of using an end-fire antenna for the excitation of the waveguide (inner core) rather than more conventional excitation techniques is that the fields generated are matched to the dominant mode of the pipe and with power flow in the desired forward direction. This is important as the antenna could be positioned in practice (within a real oil and gas well) at different pipeline depths for sensory information collection considering a repeater system implementation. So if a non-directive antenna was employed or a more conventional waveguide feed, signal power could be inadvertently directed to the pipeline edge (upwards) and down the pipeline (towards the bottom), which might not be desired.

The optimized design of the antenna was simulated and then fabricated, and its reflection coefficient was studied by simulations and lab measurements (Fig. 4.4). The following results describe how the antenna operates in a free space environment. In the bandwidth around 2.4 GHz where the system operates, the antenna has a good matching (below -10 dB). The results extracted from the simulation are the reflection coefficient, the radiation pattern, and the efficiency of the antenna. In Fig. 4.5 the realized gain and the radiation pattern as a function of ϕ when $\theta = 90°$ is shown.

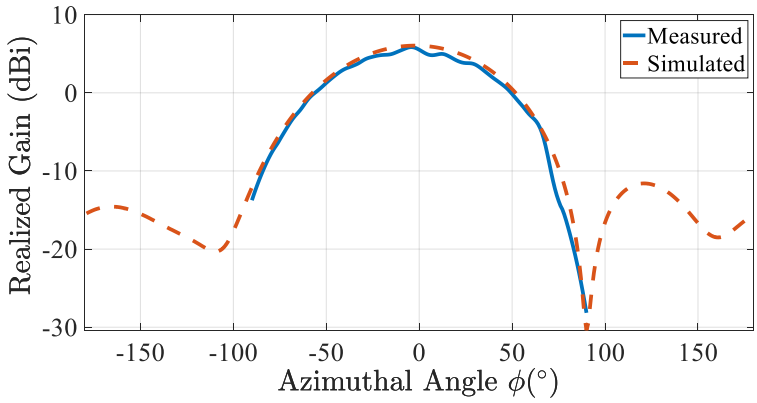

Figure 4.5: Realized gain of the antenna in free-space as a function of the azimuthal angle ϕ ($\theta = 90°$).

Pipe Section	Length (m)	$\mid S_{21} \mid$ (dB)
A	12.54	-7.86
B	12.15	-12.1
C	11.34	-6.1
Section Cut by C	1	-1.75
A & B	24.69	-12.12
A & B & C	36.03	-14.98

Table 4.10: Transmission coefficient ($\mid S_{21} \mid$) at 2.4 GHz for two antennas placed at either end of the corroded pipe (both individual and combined) considering carbon Steel 1010

4.3.2 Power Flow, Path Loss, & Testing

Table 4.10 defines the different pipeline sections that were chosen for the experimental testing. All the circular pipes were manufactured using carbon steel 1010 and had a radius $\alpha = 69.85$ mm. Also, a layer of rust (Ferrous Ferric Oxide) covers the interior walls of the pipeline sections.

The microstrip-based end-fire Yagi-Uda antennas were first centered and placed at the edges of each pipeline section (see Fig. 4.6), defining the transceiver system. Also, absorbing boundary conditions are employed using a practical microwave absorber such that no power is diverted outside the pipes (Fig. 4.6a). When simulating the aforementioned system, and when considering the pipe to be air-filled, the extracted electric field is the same as the electric field of the TE_{11} mode as reported in Fig. 3.12. The power flow was extracted, showing that the propagation is mainly routed in the z-direction (Fig. 3.13) while maintaining a maximum along the middle of the pipe. These simulation results are significant and identify that directive TE_{11} mode propagation is achieved for the experimental setup same as the half-wave dipole when routing power into the pipe system (see Subsection 3.3.3).

A transmission path loss (TPL) model can also be defined for the pipeline system. For each pipe section, the S-Parameters were measured (Fig. 4.7) using an S5048 2-Port vector network analyzer (VNA) by Copper Mountain Technologies. The reflection

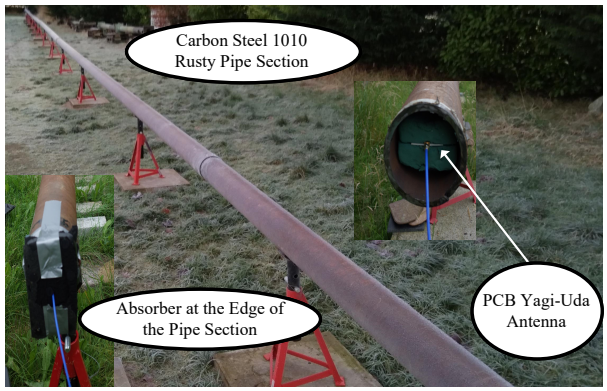

(a)

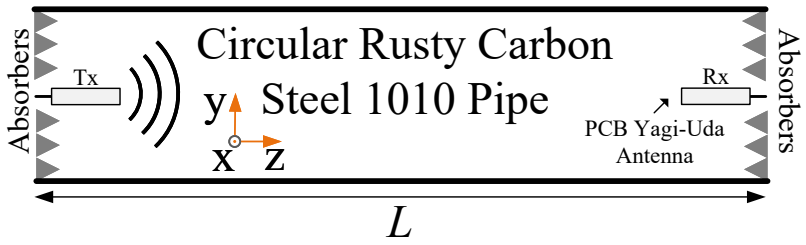

(b)

Figure 4.6: (a) Experimental and (b) schematic setup where the Yagi-Uda antennas were placed at the edges inside the corroded circular metallic pipe defining the transceiver system. Absorbers were placed at the edges behind the antennas.

coefficients of the antennas (| S_{11} |) and (| S_{22} |) in dB for the frequency range from 2.2 to 2.6 GHz, demonstrate good performance, (with values below -10 dB) inside each pipe section and the transmission coefficients (| S_{21} |) and (| S_{12} |) are quite low as well (Fig. 4.7). However, the transmission coefficients (| S_{21} |) and (| S_{12} |) for Pipe B are pretty low ($\ll$ -10 dB) due to the rust filings and some mud (in the interior of the pipe) which could not be removed practically during the measurement campaign.

The pipe sections were also mated together, in that pipe sections A & B, for example, were combined for a total pipeline length of about 25 m (see Table 4.10). Although the transmission coefficients for joint sections A & B are about -12.2 dB and -15 dB for the joint sections A & B & C, these values still make the system suitable for experimental testing. Due to the cable length requirements, the transmission loss for the joint pipe sections, A & B & C, was measured using a 2024 Marconi RF Signal Generator (operating from 10 kHz to 2.4 GHz) and an HP Agilent 8594E Spectrum Analyzer operating from 9 kHz to 2.9 GHz, by measuring the received signal power. The transmission loss, in that case, was measured at -14.98 dB (Fig. 4.8).

By studying all these transmission coefficients, TPL model was developed for the wireless system as reported in Fig. 4.8. Furthermore, the numerical curve in Fig. 4.8 is linear, and a good agreement can be observed with the measurements. Moreover, the developed TPL model for the system can be described by

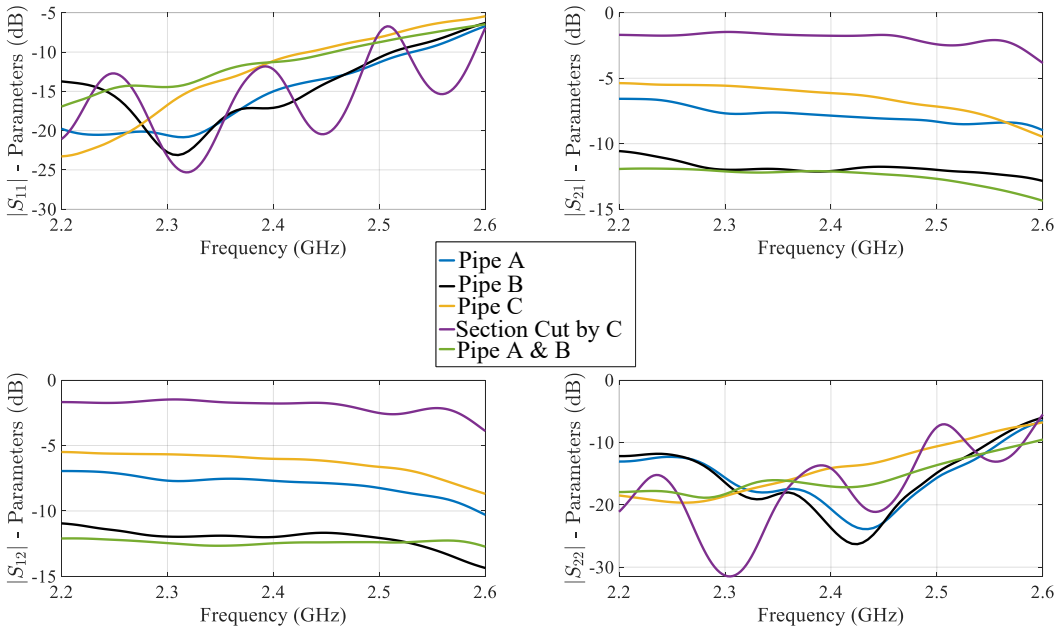

Figure 4.7: Measured S-Parameters for the system when the PCB Yagi-Uda antennas were placed inside the pipe sections.

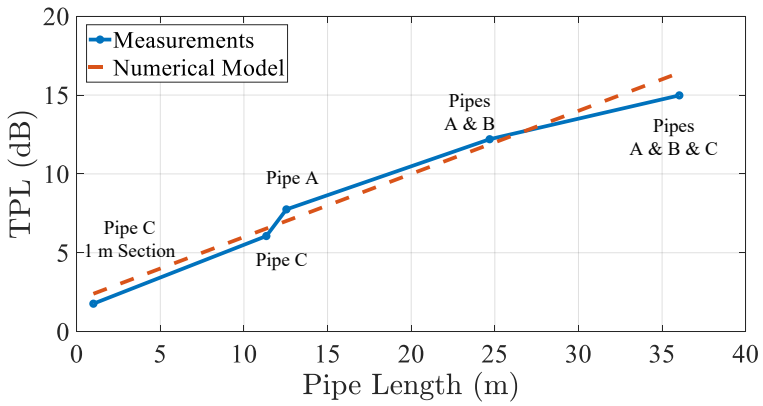

Figure 4.8: Measured and numerically calculated transmission path loss (TPL) for the two PCB Yagi-Uda antenna transceiver systems when placed at the edge of each pipe section.

$$\mathrm{TPL} \quad = \quad (\alpha_c + \alpha_r + \alpha_s) \times L + \mathrm{SL} - G_{eff_t} - G_{eff_r}. \tag{4.1}$$

The system loss (SL) accounts for standard power losses independent of the pipeline length. In particular, this SL defines the power not received at the receiver antenna and any possible power propagating in the backward direction with respect to the transmitting antenna. The variables α_c, α_r, and α_s symbolize the attenuation constants for the

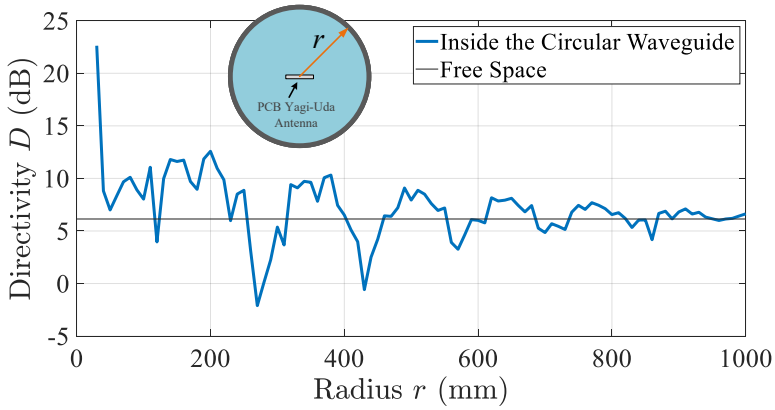

Figure 4.9: Simulated directivity in the forward +z-direction for the PCB Yagi-Uda antenna, operating at 2.4 GHz in terms of the circular metallic waveguide's radius (r) where it is operating within. A comparison is also shown with the free-space directivity value (horizontal line, about 6 dB) for an analogous PCB Yagi-Uda antenna.

power due to the conductor losses, the rust, and the surface roughness. The sum of these attenuation constants is defined by the slope of about 0.4 dB, referring to the blue line in Fig. 4.8. The numerically calculated attenuation constants for carbon steel 1010 (α_c), and for the ferrous ferric oxide (rust) (α_r) are given by Table 4.9. The simulated sum up of α_c and α_r for this system, considering a rust layer with a thickness of 0.3 mm, was extracted at 0.25 dB/m, which agrees with the numerical calculations. Also, the total measured loss factor (0.4 dB/m) must be related to surface roughness in the pipe. This difference of 0.15 dB/m between the measured and numerically modeled system is most likely related to this surface roughness and the mud, which cannot be easily modelled. Also, the TPL equation includes the effective gains of the PCB Yagi-Uda antennas within the pipeline.

It is interesting to note that the sum of the variables SL, G_{eff_t}, and G_{eff_r} is -2 dB when inspecting Fig. 4.8, and this suggests that the effective gains for the transmit and receive antennas are of suitably high value (see Figs. 4.9 and 4.10) to overcome any power losses whilst ensuring directive propagation as required. These parameters are further studied and calculated in Section 4.4.4.

4.3.3 Directivity, Gain, & Impulse Response

The effective gains for the two Yagi-Uda PCB-based antennas placed inside the pipe differ from the free space gains. This is because the radiating near-fields are dominant when placed in the guided circular metallic environment, in that the near-fields generated by the antennas do not reach the far-field zone. In particular, the near-fields generated are confined within the guide and are field matched to the dominate TE_{11} mode for power routed propagation within the pipeline (see Fig. 3.13). This scenario defines an alternative definition for the antenna gains within the communications link compared to more conventional free-space propagation. A similar analysis was presented for the half-wave dipole when it was placed into the pipe (see Section 3.3.5).

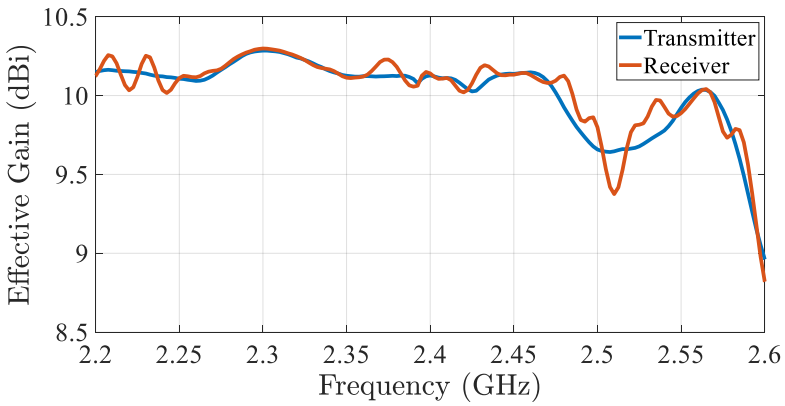

Figure 4.10: Measured gain for the transmitter and the receiver antennas using the impulse response. The PCB Yagi-Uda antennas were placed inside the circular pipe section (defined by Pipes A & B & C) with a radius of 69.85 mm.

Following this, the directivity (D) was studied and simulated for the employed Yagi-Uda PCB-based antenna when placed into the circular metallic environment while considering various waveguide radii (r). The results are presented in Fig. 4.9. For every change in the radius, the directivity was recorded in the z-direction, which is defined as the forward path for signal propagation. Then the radius of the pipe was gradually increased until it reached the far-field zone. As observed in Fig. 4.9, the free-space value for the directivity (6.14 dB) was eventually achieved as the radius of the pipe became larger.

When considering the maximum antenna gain (G_0), its value is related to the maximum directivity (D_0) multiplied by the radiated efficiency; i.e., $G_0 = \varepsilon_R D_0$, where ε_R is the total radiation efficiency of the antenna. Moreover, simulations suggest that the radiated efficiency of the PCB Yagi-Uda antenna (ε_R) was around 97% for all the simulated pipe radii. Moreover, it was observed that the maximum directivity (D_0) of the antenna when the pipe radius was $r \approx 70$ mm (such as the studied case) is 9.765 dB. Hence, the effective gain of the antenna antenna (which does not include mismatches) is given by [59] $G_{eff} = \varepsilon_R D_0 \approx 9.5$ dBi.

An alternative way to characterize the effective IEEE gain of an antenna is through the impulse response $h(t)$ [60], similarly as it was presented in 3.3.5. The Fourier transform of the normalised impulse response ($H_N(\omega)$) is given from (3.29) while considering the group velocity, v_g, of the propagating mode, which is not typical; i.e., most commonly the free-space wave velocity c is adopted when characterizing antennas. Here d is the distance between the transceiver and receiver. Specifically, v_g is the group velocity for the TE_{11} mode, 2.55×10^8 m/s. For the calculation of (3.29), the transmission coefficients $S_{21}(\omega)$ and $S_{12}(\omega)$ are required. Also, the relation between the gain of the transmitter and the impulse response [61] of an antenna is given from (3.30). The wavelength (λ_g) of the TE_{11} mode is, in this case, 0.1468 m (usually, the free-space wavelength λ_0 is used). Also, the gain of the receiver $G_r(\omega)$ is given by the use of $S_{12}(\omega)$ instead of $S_{21}(\omega)$.

Therefore, by placing the two identical PCB Yagi-Uda antennas within the pipeline

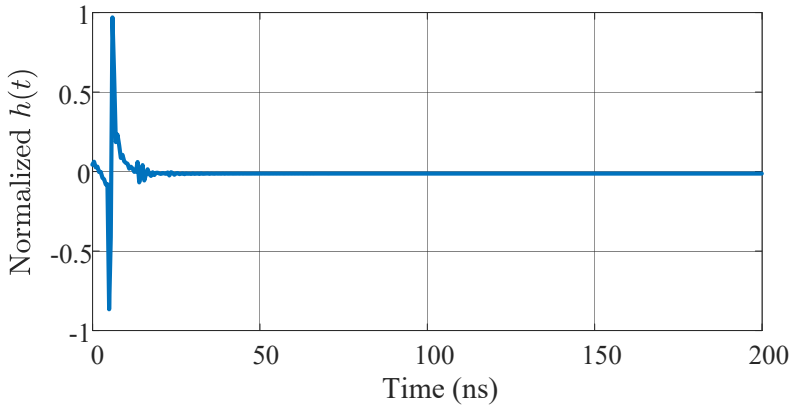

Figure 4.11: Time-domain impulse response of the system as described in Fig. 4.6.

Gap	Extra Loss (dB)
0	0
$\lambda_0/4$	1
$\lambda_0/2$	3
λ_0	5.2

Table 4.11: Extra loss due to controlled gaps between pipes A & B

and separated by a distance d apart, the impulse response was measured (see Fig. 4.11) while using pipe section C. Using these results, the measured transmitter and receiver antenna effective gains are reported in Fig. 4.10, by (3.30) from 2.2 to 2.6 GHz. At 2.4 GHz, the measured transmit and receive gains inside the circular waveguide were 9.1 dBi and 9.09 dBi, respectively. These gains are very close to the simulated effective gain of 9.5 dBi.

4.3.4 Gap Between the Pipe Sections

During the pipeline measurements in the field, it was observed that some unwanted gaps could exist between two sections of pipe. For example, between pipes A and B (see Table 4.11). The pipes could not be perfectly mated with commercials couplers even with the best efforts. This was related to the suitable positioning of the pipe sections, which were made possible by a mechanical forklift. This is because each pipeline section had a mass of over 200 kg. Therefore, the actual structure of the oil and gas pipeline is not homogeneous along its total length. Gaps may cause some extra losses. To further examine this loss, measurements considering the possible gaps between the joint pipe sections A and B are examined and outlined in Table 4.11, which are a function of λ_0 at 2.4 GHz.

4.3.5 Link Budget Analysis when Pipes A, B, & C are Combined

A power link budget analysis like in standard telecommunication systems can now be developed as all the parameters have been defined and evaluated. Based on (3.24)

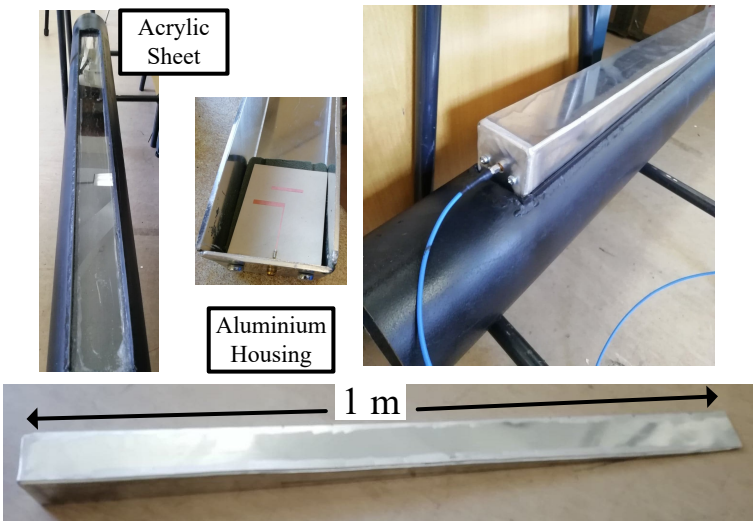

Figure 4.12: Aluminium mechanical housing 1 meter long (radome) of the antenna. The housing is placed on the top of a 2 meters piece of the inner core and between them, there is an acrylic sheet (mandrel).

to (3.26) each propagating mode has its own power flow. Also, it was defined that the propagated mode inside the pipelines is the TE_{11} mode, which has a percentage power flow of 89.35 %. Given this value, the rest of the power flow is considered lost. Numerically, this loss is translated to $\mid 10\log_{10}(0.8935) \mid \approx 0.5$ dB. Also, from the TPL, the total attenuation constant (α) is the sum of the attenuation constants due to the conductor losses, calculated to be 0.4 dB. As described previously, the effective gain of each antenna was measured and calculated to be about 9.1 dBi, and these values are included in the TPL model. By (4.1), the SL can be evaluated to be around 20 dB. Also, $\lambda_0/4$ was chosen as the distance for each gap between the pipe sections because this separation appeared to be the norm when mating the different pipe sections. Therefore the extra losses due to the gaps between the pipe sections were estimated as 1 dB. Given these parameters, the link budget equation can be stated as follows:

$$P_{Rx} = P_{Tx} - 0.5\,\text{dB} - \alpha \times L - \text{SL} + G_{eff_t} + G_{eff_r} - \text{No. of Gaps} \times 1\,\text{dB}, \quad (4.2)$$

where P_{Rx} and P_{Tx} are the received and transmitted power, respectively, and their units are dBm.

4.4 PCB Yagi-Uda Antenna and Housing Placement

In this section, the pipeline is studied when an end-fire antenna is employed as its waveguide source, but it is placed into a mechanical housing that protects the antenna and any electronic components from the well environment and gas flow. The parameters analyzed here are the propagating mode, the routing of the field, the path loss, and the effective antenna gains inside the circular pipeline.

(a)

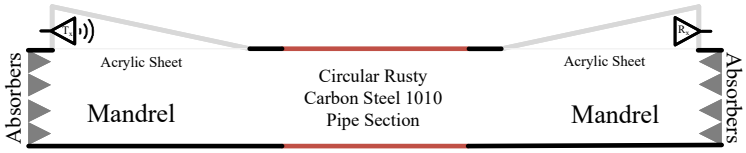

(b)

Figure 4.13: (a) Experimental and (b) schematic setup where the Yagi-Uda antennas were placed into the housing (or radome) which is installed on the top of a 2 m carbon steel 1010 section (representative of a practical mandrel rig). Between the transmitter and the receiver, the mandrel is connecting the experimental pipe sections (see Table 4.10). Absorbers were placed at the edges of the pipelines.

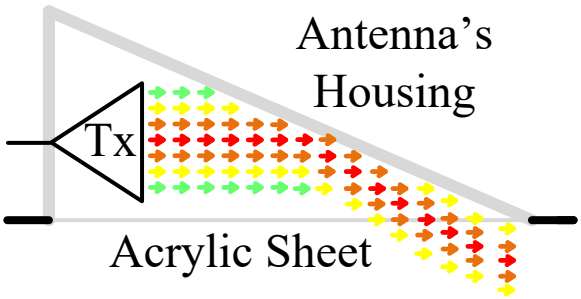

Figure 4.14: Simulated power flows shows the smooth injection through the sheet. This happens because of the long ramp housing as practically its termination is into the inner pipe.

4.4.1 Radome Housing

The selection of the optimal antenna design for directive field propagation inside the pipeline is vital for the operation of the proposed microwave reflection system. Most importantly, the antenna must fit inside the constraints imposed by the built-in housing and operate effectively at 2.4 GHz (see Fig. 4.12). For the aforesaid reasons, a compact planar Yagi-Uda printed circuit board (PCB) antenna was designed and optimized using the CST Studio Suite EM simulation software (see Section 4.3.1).

In an operational oil and gas flow system, the antenna and the electronic components can be exposed to high temperatures and pressures and might be damaged due to the surrounding pipeline contents and the production fluid flow [40]. For this reason,

Mode	TE_{11}	TM_{01}	TE_{21}
$\mid S_{21} \mid$ (dB)	**-2.37**	-31.6	-11.58

Table 4.12: Simulated transmission coefficient ($\mid S_{21} \mid$) for determining the coupling into each mode at 2.4 GHz. The simulation setup includes a 2 m carbon steel circular waveguide pipe with the antenna positioned within the mechanical housing which was placed on top of the waveguide. An ideal waveguide port was positioned on the other side of the guide

creating a sealed antenna housing, i.e., an effective radome cover will be required to provide a suitable protective environmental enclosure. Figure 4.12 shows the concept of the housing (see also Fig. 4.13), which has been constructed from aluminum, and there is a feed through at its edge so that the antenna can be connected with a coaxial cable for experimental testing of the prototype.

The mechanical housing is a 1-meter long ramp, its maximum height is 0.06 meters, and its width is 0.068 meters. This narrow space does not allow the use of another type of antenna, e.g., an antenna array, which potentially could be more efficient. Also, the housing is placed on top of a 2 meters piece of the inner core, and between them, there is an acrylic sheet (see Fig. 4.12). This complete mechanical system is called a mandrel. It can be positioned at both the transmitter and receiver sides of the pipeline or at a midpoint position of the pipeline for a repeater system. The electromagnetic wave propagates through the acrylic sheet, and the inner core is fed while the antenna is protected. The relative dielectric constant (ϵ_r) of the acrylic sheet used is 3. Also, the antenna is polarized horizontally (as it is end-fire), and its position within the housing has been optimized for minimal reflections and maximum coupling into the pipeline. More specifically, the antenna is placed parallel to the acrylic sheet. This is because the power flows smoothly into the pipeline, and this smooth injection happens because of the long ramp housing as practically its termination is into the inner pipe 4.14.

4.4.2 Field Routing Within the Pipe

At this stage in the system development, it is also essential to understand how the EM fields propagate when the directive antenna is mated with its mechanical housing and the circular pipeline itself. In the CST Studio Suite EM simulation software, the PCB end-fire Yagi-Uda antenna was placed into the mechanical housing, which was then placed on the top of the inner core section (see Figs. 4.13), defining the excitation source for the system. At the other edge of the mandrel, a waveguide port was placed. The waveguide port can excite all the desired modes (TE_{11}, TM_{01}, TE_{21}) and monitor the results of S-parameters for each mode separately. This CST Studio Suite EM simulation software was able to ascertain which modes were mainly excited, and this was studied by investigating the relative powers of each mode.

The results comparing the relative powers for each mode can be observed in Table 4.12. Here the transmission coefficient ($\mid S_{21} \mid$) represents the coupling into each mode from the driven antenna. Based on these results, the dominant mode is TE_{11} as the insertion loss value is minimum. This implies that the majority of power from the antenna excitation, and its protective housing arrangement, is coupled into the TE_{11} mode of the circular pipeline. This is because $\mid S_{21} \mid$ values are about - 2.4 dB, while

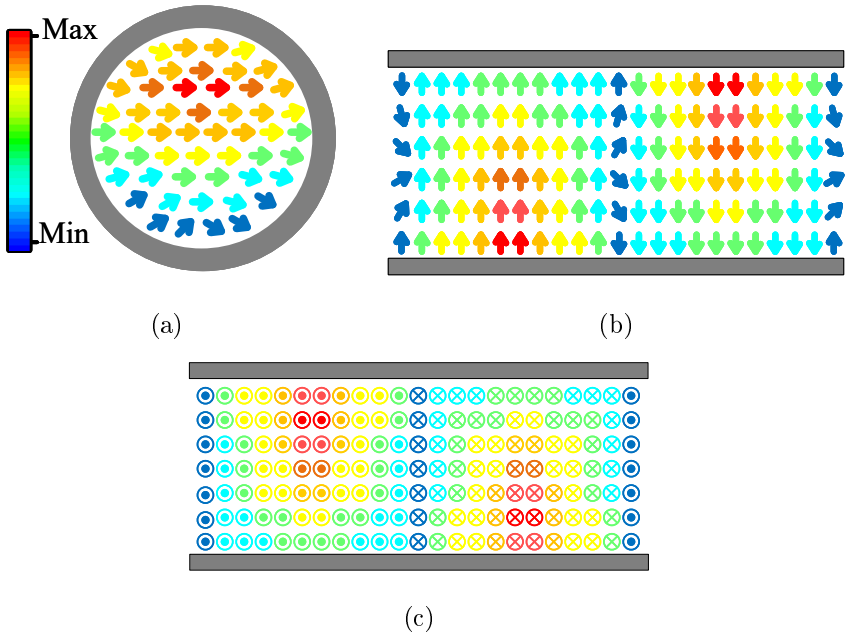

Figure 4.15: Electric field lines in the inner core, when the excitation occurs from the PCB Yagi-Uda antenna is placed into the mechanical housing. It can be observed that the propagating mode is the TE_{11} mode. (a) Transverse plane (x-y plane). (b) Longitudinal plane top view (x-z plane). c) Longitudinal plane side view (y-z plane) as they are extracted by the simulated circular metallic waveguide.

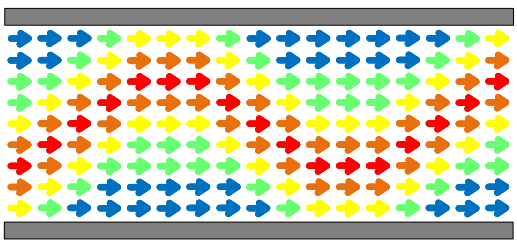

Figure 4.16: Simulated power flow lines within the circular metallic waveguide generated by the PCB Yagi-Uda antenna, which is placed into the mechanical housing. The longitudinal plane or side view is shown, i.e., the y-z plane.

all the other powers diverted into the different modes are about - 11.5 dB or below. Also, in Figs. 4.15 and 4.16 the simulated electric field is reported. These show the power flow along the circular pipeline beyond the ending point of the housing. More specifically, as it can be observed by Figs. 4.15 and 4.16 the electric field and the power flow are consistent with the corresponding of the TE_{11} mode (see Figs. 3.12 and 3.13), but slightly distorted because of the distribution of the TE_{21} mode.

Pipe Section with Mandrels	Length (m)	$\mid S_{21} \mid$ (dB)
A	16.54	-15.2
B	16.15	-18.1
C	15.34	-16.3
Section Cut by C	5	-9.04
A & B	28.69	-34.7
A & B & C	40.03	-38.6

Table 4.13: Transmission coefficient ($\mid S_{21} \mid$) at 2.4 GHz for the antennas when each mandrel is joint the edges of each pipe section

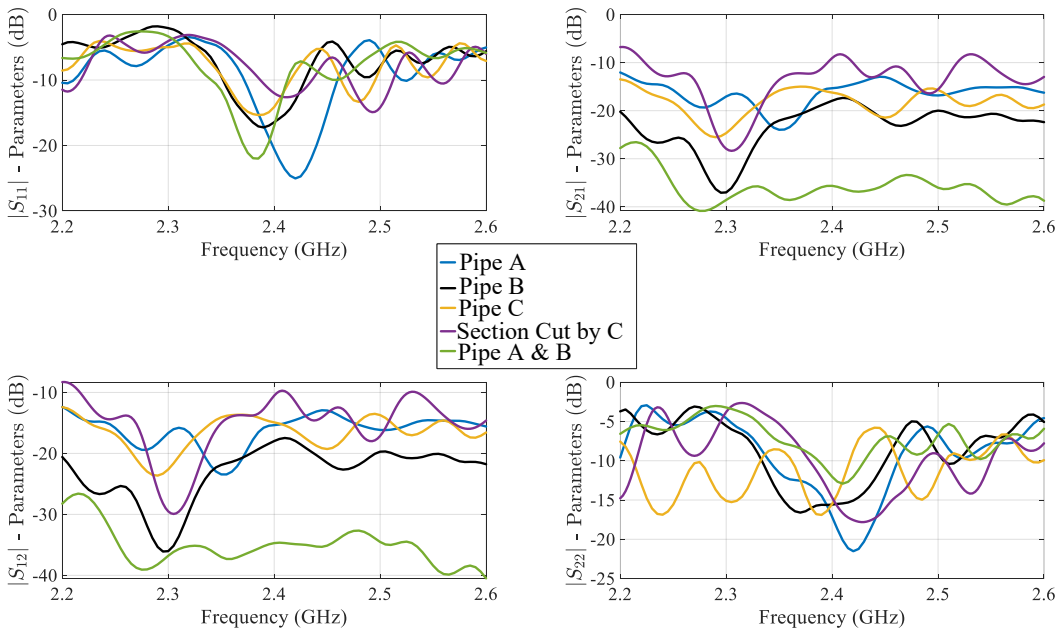

Figure 4.17: Measured S-Parameters for the system when the PCB Yagi-Uda antennas of each mandrel were is joint on the edges of each pipe section.

4.4.3 Path Loss & Testing

A transmission path loss (TPL) model can also be defined for the pipeline system described in the previous systems. For each pipe section the S-Parameters were measured (see Fig. 4.17 and Table 4.13) placing a mandrel in each side (see Fig. 4.13b) using a 2-Port VNA. The reflection coefficients of the antennas ($\mid S_{11} \mid$) and ($\mid S_{22} \mid$) in dB for the frequency range from 2.35 to 2.45 GHz, demonstrate good performance, (with values below -10 dB) inside each pipe section and the transmission coefficients ($\mid S_{21} \mid$) and ($\mid S_{12} \mid$) follow a linear scale in terms of the length of each pipe section (see Figs. 4.17 and 4.18).

The reflection coefficients for the joint sections A & B &, and C were measured at -13.5 and -17.4 dB for the experimental testing. The transmission loss, in that case, was measured at -38.6 dB (Table 4.13) using the noted Signal Generator and the Spectrum Analyzer.

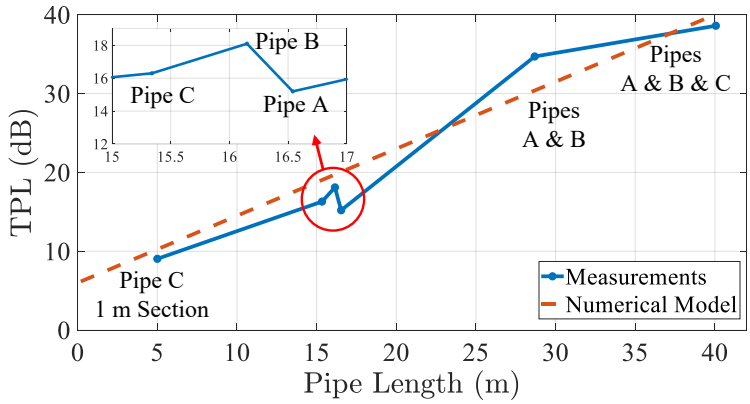

Figure 4.18: Measured and numerically calculated transmission path loss (TPL) for the two PCB Yagi-Uda transceiver antennas of each mandrel where they are joint at the edges of each pipe section.

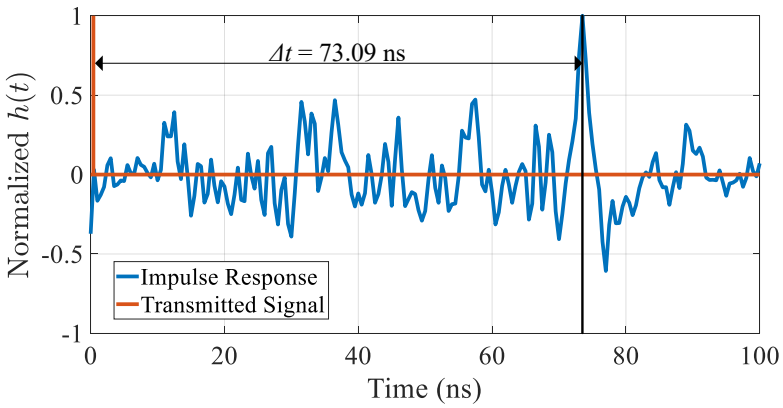

Figure 4.19: Time-domain impulse response of the system: Mandrel - Pipe A - Mandrel. The time difference between the transmitted signal and the impulse response is presented.

By studying all these transmission coefficients, TPL model was developed for the wireless system as reported in Fig. 4.18. Furthermore, the numerical curve in Fig. 4.18 keeps the linearity as was shown in Fig. 4.8. Moreover, the developed TPL model for this system can be described by (4.1). Although the sum of attenuation constants is about 0.85 dB/m, as can be extracted from the slope of the plot in Fig. 4.18. The higher value in comparison to the 4.8 is caused by the "bouncing" power flow along the pipeline. The sum of the variables SL, G_{eff_t}, and G_{eff_r} is -6 dB when inspecting Fig. 4.18. Also, the exact values of these parameters are calculated in Section 4.4.4.

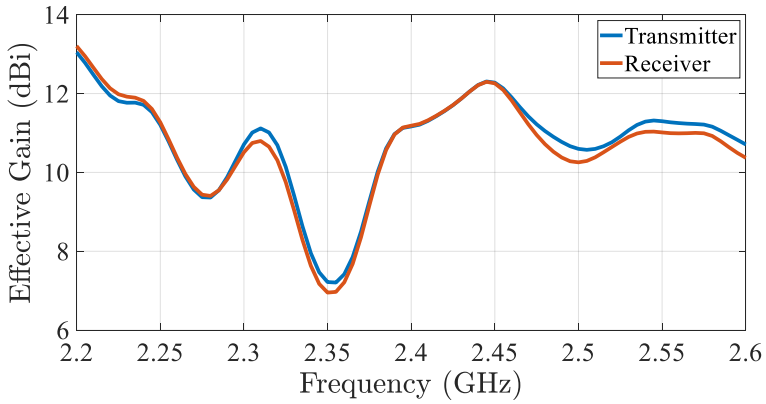

Figure 4.20: Measured gain for the transmitter and the receiver antennas using the impulse response. The PCB Yagi-Uda antennas into the housings of the mandrels where they were placed at the edges of the circular pipe section (defined by Pipes A & B & C) with a radius of 69.85 mm.

4.4.4 Effective Gain & Impulse Response

The impulse response investigation is crucial as it can characterize the group velocity of the propagating fields within the pipeline. This can also indicate the fields and modes within the pipeline environment. As it was shown earlier (see Table 4.12), the field matched mainly to the dominate TE_{11} mode and secondary to the TE_{21} mode and for power routed propagation within the pipeline (see Fig. 4.14). This suggests that the group velocity and the wavelength of the propagated signal are not precisely matched with the corresponding TE_{11} mode. Therefore, the values of the group velocity need to be further assessed and this will be discussed in the upcoming sections.

In the Fig. 4.19 is illustrated the measured normalised impulse response ($h(t)$) of the system mandrel - Pipe A - mandrel. The time difference between the transmitted signal and the impulse response is 73.09 ns. The distance (d) between the transmitter and the receiver antenna is 16.52 m. Therefore the group velocity (v_g) of the signal can be calculated, based on the expression $v_g = \frac{d}{\Delta t} = 2.26 \times 10^8$ m/s. It can be observed that the velocity of the system is between the group velocities of the TE_{11} (2.55×10^8 m/s) and of the TE_{21} (1.48×10^8 m/s), something that is was expected for the aforementioned reasons. The wavelength (λ_g) of the propagated signal mode is 0.185 m by inspection in Figs. 4.15. Using these results, the measured transmitter and receiver antenna effective gains into the housings are reported in Fig. 4.20, by (3.30) and (3.29) from 2.2 to 2.6 GHz. At 2.4 GHz, the measured transmit and receive gain values were calculated as 11.17 dBi and 11.19 dBi, respectively. Therefore, by (4.1), the SL can be valued to be around 28.36 dB.

It can be observed that the effective gain value of the antennas when placed into the mechanical housing is greater than when they are placed directly into the pipeline. This can be explained as the mechanical housing helps in the directivity of the radiated power as it is routed into the medium, i.e., pipeline. The system losses (SL) are greater as well because firstly, the "bouncing" of the power flow directs some of the signal backward,

and secondly, the antenna is within the housing, and this arrangement is on top of the pipeline. Basically, this arrangement can add some additional transmission losses when compared to the setup of having the antenna directly positioned within the middle of the pipeline.

4.5 Communication Testing

Two pipeline systems (with and without mechanical housing) from an EM point of view were studied in the previous sections. These transceiver systems were used for the pipeline data communication setup, similar to the structure which was described in Section 3.4. The system includes two N210 universal software radio peripherals (USRP) modems by National Instruments, defining the transmitter and receiver communications hardware. Also, some commercially available high gain and low noise amplifiers (with a maximum gain and noise figure of 21 dB and 1 dB, respectively) were employed, and barometric pressure and temperature sensors by Bosch (BMP180) for sensor information data collection and exchange. This sensor was managed by an Arduino (ATmega328P) microcontroller.

The primary sensory data that was tested for transmission along with the pipeline arrangement (see Fig. 4.1) was the environmental temperature and pressure. This was managed by an in-house code and graphical user interface (developed in MATLAB/Simulink and LabVIEW), which also was designed to send communication text messages and digitized images. Both could be defined by the user and uploaded in real-time, respectfully.

The modulation scheme adopted was OFDM and the techniques were BPSK for the transmission sensory and images, and QPSK for the video transmission. Using OFDM helps to mitigate any multipath effects in the pipeline (and in general) when transmitting over long distances [63]. In addition, the signal was transmitted with additive white Gaussian noise (AWGN) for some trials, so the SNR at the pipe input was controlled during experimental testing. Also, the default transmitted power of the USRP was -25 dBm which can be re-programmed to have a maximum total output power of about 5 dBm. For control of these parameters, the graphical user interface (GUI), as shown in Fig. 3.17, also controlled these transmission metrics. For example, the user can change the gains of the USRPs, the SNR values, and the type of transmitting data (text, image, pressure, and temperature). This GUI was made available on a laptop positioned at the transmitter side of the pipeline. The system was also programmed in such a way that the data was re-sent repeatedly until the user decided to stop the transmission. This helps with the real-time monitoring of the system. The user can also choose when to receive the transmitted data at the receiver laptop.

4.5.1 PCB Yagi-Uda Antenna into the Circular Waveguide

The experimental setup of the RF data communication system is further shown in Fig. 4.21 when the Yagi-Uda based PCB antennas that were placed into the pipe were connected in series with the N210 USRP modems at both transmitter and receiver sides of the pipeline. In particular, the antennas were placed at the ends of the joint pipe sections, i.e., the A, B, and C pipeline sections. This field testing aimed to investigate the

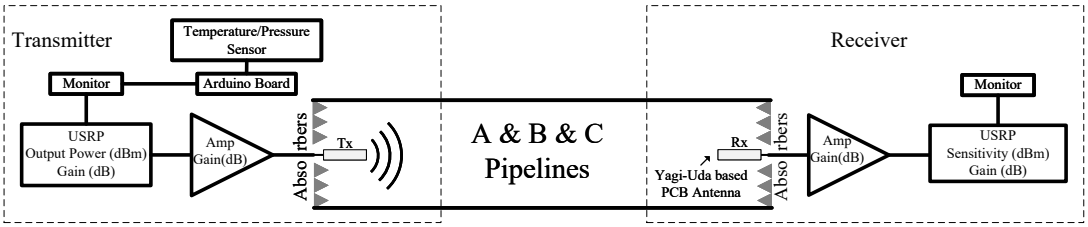

Figure 4.21: Block diagram of the setup for the experimental testing of the propagation system. Transmitter side chain: Monitor, USRP, amplifier, Tx Yagi-Uda PCB-based antenna (positioned at the edge of the inner core). Also, an Arduino microcontroller board and the temperature/pressure sensor were connected to the monitor for sensory data transmission. Receiver side chain: monitor, USRP, amplifier, Rx Yagi-Uda PCB-based antenna placed at the edge of the inner core. At the edges of the inner core, a microwave absorber was positioned to contain power flow inside the pipeline.

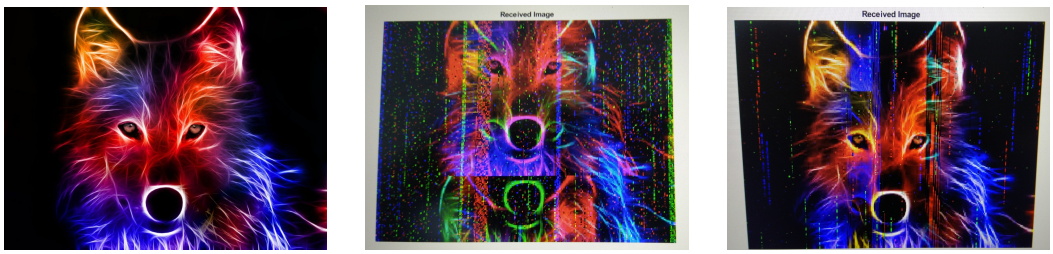

(a) (b) (c)

Figure 4.22: Transmitting directly through the circular pipe to test the limitations of the system as it is illustrated in Fig. 4.21. (a) Original photo. (b) Power level limitation. (c) SNR limitation.

data transmission through the pipe and then define any limitations for the transmission system in terms of BER and received power.

The system parameters were as follows: (i) the TPL for the A & B & C was 15 dB from Table 4.10, (ii) the USRP transmitted power was -25 dBm, and neither additional gain nor the external amplifiers were applied on the transceivers initially. Also, after significant efforts during the field measurement setups, at this stage, there were not any significant gaps between the different pipe sections. Therefore, based on (4.2), the received power was about -40 dBm, and this was verified experimentally. The digitized image was also successfully transmitted and received (Fig. 4.22a) in all attempts, without any deformation. Furthermore, the sensory data was transmitted, received, and monitored in real-time accurately. The temperature that appeared on display was 8.06° C, and the pressure was 102.2 kPa. Slight changes in the temperature and pressure near these initial values were successfully monitored during the measurements.

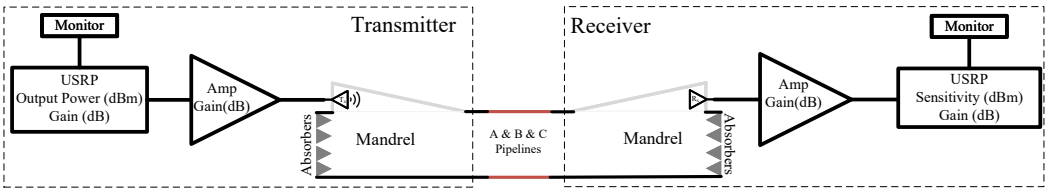

Figure 4.23: Block diagram of the setup for the experimental testing of the propagation system. Transmitter side chain: Monitor, USRP, amplifier, Tx Yagi-Uda PCB-based antenna (positioned into the mechanical housing). Receiver side chain: monitor, USRP, amplifier, Rx Yagi-Uda PCB-based antenna into the mechanical housing. At the edges of the inner core, a microwave absorber was positioned to contain power flow inside the pipeline.

4.5.2 PCB Yagi-Uda Antenna into the Housing

The same experiments mentioned above were repeated but with the mechanical housing as the set up in Fig. 4.23 shows. Again the USRP transmitted power was -25 dBm, and neither additional gain nor the external amplifiers were applied to the transceivers initially. The TPL for the A & B & C including the mandrels was 38.5 dB from Table 4.13. Therefore, the received power was about -64 dBm, verified experimentally using the Signal Analyser. The digitized image was also successfully transmitted and received (Fig. 4.22a) in all attempts, without any deformation.

Moreover, a live video was recorded when the mandrels were used. In this testing, a live streaming video was recorded, transmitted, and received in real-time through the pipeline. The transmitter mandrel and the receiver mandrel were joined together during the testing. In contrast with the transmission of the digitized images and sensory data, for the transmission of the live stream video, LabVIEW was used for the USRPs instead. The reason is that LabVIEW was preferred in this case rather than Matlab and Simulink in that it offered more efficient system communications and better transmission of the video packages. The QPSK modulation techniques was used.

4.5.3 Minimum Power Level Studies for Maximum Range Estimation

The next set of measurements was carried out to understand and identify when communications within the pipeline failed or were near failure, and it is referred to as the setup in Fig. 4.21. This was defined when the image or sensory data could not be successfully recovered at the receiver. For achieving the required low power levels, two 30 dB attenuators were employed at the receiver side of the pipeline. This emulated a total pipeline length of 150 m. Also, an amplifier with a gain of 20 dB was positioned on the transmitter side, and the internal gain of the USRP transmitter modem was set to be 3 dB. No amplification was defined at the receiver as well. Hence, the approximate received power was -77 dBm which is about the minimum power level required for USRP operation (which was characterized in the Heriot-Watt University microwave lab to be about -80 dBm where short cables were used to define a low noise setup). After repeated measurements, which were consistent, the image was received and monitored with a bit-error-rate (BER) of about 0.0015; however, there was some partial distortion

of the image (see Fig. 4.22b). With reduced power levels, the USRP could not successfully recover the image or demodulate sensory data accurately. Success and accurate communications resumed following increased transmit power levels and receiver gains.

4.5.4 Experiments with Additive White Noise

While maintaining the same setup as described above (by keeping all the same values for the components), however, now, controlled AWGN was introduced into the system for further testing. In particular, the SNR was set to be 15 dB. Again the image was received and monitored but with some partial distortion (see Fig. 4.22c). The BER, in that case, was increased to about 0.021. For lower values of the controlled SNR at the transmitter, the image or sensory data could not be received with any accuracy. Communications became successful with increased SNR values, considering the noted experimental setup.

In both experiments, with the minimum power level and apart from the noise at the received images, there is some inter-symbol interference (see Figs. 4.22b and 4.22c). This can be explained because of the multi-mode propagation in the pipeline which could be prevalent. As it has been mentioned, the propagated modes are three (TE_{11}, TM_{01}, and TE_{21}), and the majority of the power is coupled by the TE_{11} and secondly by the TE_{21}. This indicates a multi-path transmission. The use of the OFDM modulation scheme help to prevent this scenario as much as possible [63].

It should also be mentioned that similar data communication failure results were observed in the microwave lab at Heriot-Watt University and the field test trials in Aberdeen, Scotland. This suggests consistency of the transceiver system, albeit in a lab setting or the field with an extensive pipe length of 35 m. Moreover, the data rate in the previous experiments was estimated at 50 kbits/s using a manual stopwatch, and this maximum value was consistent for the different trials. This value could be improved in the future, but some redundancy was adopted into the developed OFDM code to ensure successful data links for the field trials. Similar testings as described in Subsections 4.5.3 and 4.5.4 took place with the mandrels and the results were in agreement.

4.6 Summary

This chapter described a more efficient communication system using compact Yagi-Uda antennas for the transceiver. The advantage of this antenna in comparison with the half-wave dipole (see Chapter 3) is that its end-fire radiation offers better system performance. Since the pipeline characteristics, the dimensions, the metallic walls, and the filling material were known, the modal analysis based on theory, the power analysis, and the conductor losses that exist because of the metallic walls were also developed.

Moreover, two different systems, both using the PCB Yagi-Uda antennas, were examined for different pipeline configurations by simulations and measurements. Firstly the antenna receiver and the transmitter were placed into a metallic pipe for oil and gas wells. The results showed that the setup could work efficiently at 2.4 GHz. The propagating mode is the TE_{11} mode, and the transmission path loss has been well defined, as well as the gain of the antennas. In addition, a link budget equation was developed, which can be applied to similar pipeline systems. A 36.03 m carbon steel circular pipe was set up in the field, and the propagation inside it was experimentally

tested. Using OFDM as the communication protocol and commercial RF components, the results showed that the transmission of about 150 m is possible (shown when using attenuators). Also, the receiving capability of the system was measured at -77 dBm in terms of power level and 15 dB in terms of the SNR demonstrating successful data communications.

In the second system, the antennas were placed into an aluminium housing on top of a mandrel. This mandrel was connecting to the pipeline. An acrylic sheet between the mandrel and the housing protects the antenna from a possible oil and gas product flow. The results showed that the system could work efficiently at 2.4 GHz. The propagated mode is a superposition mainly of the TE_{11} mode and secondly of the TE_{21} mode. Also, the transmission path loss and the effective gain of the antennas were defined, showing slightly more lossy performance than the first system. During the communication testing, digitized images and live streaming video were transmitted and successfully received through the system. All in all, the proposed systems have good performance demonstrating that real-time data can be sent and received successfully. The system, which includes the mandrels, is more practical, and despite the good performances observed, it can be improved at the mechanical and RF level in the future. These possible improvements will be further discussed in the conclusion chapter.

Chapter 5

Microwave Liquid Level Determination for Oil and Gas Pipelines

5.1 Introduction

This chapter examines the modelling and design of a complete wireless liquid level determination system in a metallic pipeline. The determination is achieved by measuring the delay between the original and the reflected signal by a liquid that could be positioned at the bottom of an oil well, using microwave and antenna engineering principles as well as the supporting signal processing (see Fig. 5.1a). Briefly, the proposed system operates as follows. A signal is excited by an antenna installed in a mechanical housing and placed adjacent to a rectangular slot at the exterior face of the outer pipeline core. The signal is reflected from the liquid at a depth, d, and returns to the antenna, where the distance to the fluid level can then be calculated. For the experimental laboratory setup, the top face of the water level is about 5.5 cm above the bottom of the pipeline. The proposed technique can reduce operational safety hazards by eliminating compressed gasses to obtain acoustic depth level measurements in wells [7]. Furthermore, the proposed technique offers a compact, low-cost, and continuous or routine method for monitoring the liquid level depths within wells and thus assisting with hydrocarbon extraction productivity, as it has already been described in Section 1.2.

This microwave approach for depth detection is further described in this chapter by reporting on the design, development, and testing of a proof-of-concept system demonstrator for such depth ranging. Fundamentally the system offers instantaneous liquid level determination using an electromagnetic wave transmitted from the surface of the wellhead. Then the reflected signal returned from the liquid-level interface (within the well) is measured. The signal is transmitted into the wellbore via microwave circuits and an antenna. These components are placed into a covered compartment at the inlet flange of the wellhead, similar to a radome allowing for the propagation of electromagnetic waves. Like in the previous chapter, this mechanical housing enclosing the circuit and antenna is essential to protect the hardware from pipeline gas flow erosion. Also, this radome protection housing makes the microwave system more universally adaptable for utilization in standard pipeline dimensions and other industry related configurations.

The pipe dimensions selected for the studies were chosen from the commercially available pipeline tubing sizes. This also ensures mechanical compatibility with industry standard pipelines. Also, given the large diameter of the pipeline (i.e., industry standard) and the adopted feeding technique (of placing the 2.4 GHz compact antenna

into the external housing, see Fig. 5.1), several challenging electromagnetic engineering problems arise as higher order modes can be excited, which is not conventional for microwave waveguides. Also, more standard (and non-directive) guide excitation techniques such as a vertical probe or loop feed [32], [56] are not practical for the intended oil and gas system, as they can perturb or interfere with the gas flow which is generally unwanted. For these reasons, a directive and low-profile antenna configuration (within a radome housing) were adopted and experimentally tested, defining the feeding arrangement.

The chapter is divided into four parts. The first part defines the coaxial waveguide characteristics, such as the relevant dimensions, the filling material, the material defining the guide, and an overview of the relevant microwave theory as applied to the pipeline. Parameters such as the excited modes, the conductor losses, and the group velocity are examined in Subsection 5.2.2 by numerical calculations and verified using the CST Studio Suite EM simulation software. In the second part of the chapter, a simulated liquid level determination for three different liquids (water, seawater, and oil) is presented in Section 5.3 at 400 MHz. In this initial unimodal propagation study, parameters such as travelling time, distance, and power loss are initially presented, having excluded the factor of multi-mode propagation. Finally, a primary link budget equation is presented based on the reflection coefficient of the waveguide source. The operation of the system is further studied in the third part of the chapter when an end-fire microstrip-based planar antenna is positioned into the radome housing, acting as the source for the system. Also, the excited EM field, the signal velocity, and the effective antenna gain are defined in Section 5.4.3 by studying the impulse response.

The final part of the chapter presents the proof-of-concept demonstrator to determine liquid levels. In particular, the reflectometry (instrumentation and microwave circuit) system, as well as the results from two different kinds of exciting pulses, are explored in Section 5.5. Finally, a link budget equation is developed to calculate the maximum depth that can be achieved for the system. To the best knowledge of the author, no similar liquid level determination system using microwaves has been reported previously in the open literature while also providing the theoretical foundations. CST Studio Suite EM simulations and laboratory measurements also support all these findings.

5.2 Pipeline System and Modeling

The proposed system can be further described as follows. The EM wave is transmitted and propagates into the annular waveguide space formed by the well conduit. When the signal reaches the reflection boundary at the segregated liquid interface (representing an equivalent electrical short circuit), the wave is then reflected from the boundary and received back at the surface of the well (using the same antenna as for signal transmission). The propagation time of flight for the signal is then processed and analyzed to determine the liquid level depth (i.e., the physical distance from the wellhead antenna to the liquid interface depth). For this work, the fluid interface shall be assumed to be water or an under-saturated hydrocarbon liquid phase mixture which is representative of most oil and gas wells [74]. Also, to complement the design and test of such a microwave system, a link budget equation and a reflectometry analysis of the time-domain signals are needed to define the propagation characteristics of the microwave signal and, thus,

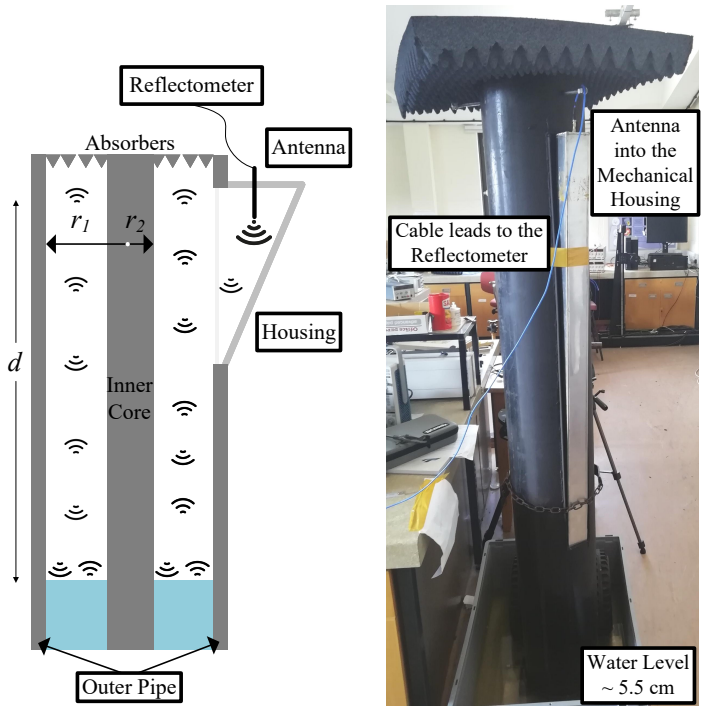

(a) (b)

Figure 5.1: (a) System schematic and (b) experimental test setup for proof-of-concept of the proposed microwave ranging system.

are fully described in the following.

Basically, the oil and gas pipeline can be treated as a coaxial metallic waveguide and this is why the background on coaxial waveguides was presented in Chapter 2. The propagating environment is defined by the dimensions, the structure, the filling material, and the environmental conditions under which the waveguide operates. Thus, it is analyzed by the possible modes, the conductor losses, the group velocity, the electromagnetic field, and the power flow through the waveguide at the operational frequency, which was selected to be 2.4 GHz for the system demonstrator. This is because there is an abundance of low-cost commercially available RF devices that operate at 2.4 GHz. This inherently will reduce the system implementation costs and the complexity of any licensing requirements when deploying the system for practical oil and gas pipelines.

5.2.1 Selected Pipeline Characteristics and Filling Material

The available downhole well geometry defines the selected coaxial waveguide size used for this study. In particular, these are typical dimensions for oil and gas pipeline tubing. The inner radius (r_2) of the chosen pipeline is 69.85 mm (or $0.525\lambda_0$ at 2.4 GHz) and wall thickness t = 10 mm (or $0.08\lambda_0$ at 2.4 GHz). The external radius (r_1) is 136.525 mm (or $1.0925\lambda_0$ at 2.4 GHz), and the wall thickness is the same as the inner pipe (10 mm). The wall material is AISI 1010 carbon steel, and its chemical composition can be found in Table 4.1. Also, regarding the pipeline electrical properties, this has already been mentioned in Section 4.2; i.e. the conductivity (σ) and the relative magnetic

permeability (μ_r) of carbon steel 1010 is 6.993×10^6 S/m and 100, respectively.

During oil and gas production periods, essentially when the well is operating under hydrocarbon flowing conditions, the pipeline contains a multi-phase mixture (defined by combinations of gas, oil, and water [51]). This allows for a full range of possible chemical compositions, making it too broad to describe all gas flow production situations considered in this thesis. Therefore a representative and simplified model for the gas flow was adopted. Methane (i.e., C_2H_4, natural gas) is considered to flow inside most pipelines (and in the coaxial, annulus region) and thus can define the production fluid inside the wellbore. Also, in this work, the methane mixture is assumed to be in a gaseous phase at the oil and gas well pressure and temperature conditions, which is typical. This is important as the electrical properties of methane can be approximated as an air medium [42]. This has also been described in the last chapter. Therefore for the presented theoretical calculations, the CST Studio Suite EM simulations as well as measurements, in this chapter, the representative filling material inside the pipeline was also considered to be air [42], i.e., the relative permittivity (ϵ_r) and permeability (μ_r) was taken equal to 1 (see Subsection 2.4).

5.2.2 Mode Analysis & Conductor Losses & Group Velocity

The coaxial waveguide can support TE and TM waveguide modes and the TEM mode. This transverse electromagnetic or TEM mode is the dominant mode in a coaxial guide (here $\lambda_g = \lambda_0$ is defined as the guide wavelength for the dominant TEM mode). The operational frequency for the demonstrator has already been identified at 2.4 GHz, so every mode with its cut-off frequency over this threshold does not propagate. The cut-off frequency for the higher order modes is as follows from [56]:

$$f_c = \frac{1}{2\pi\left(r_1 + r_2\right)\sqrt{\mu_0\epsilon_0}}\left(\frac{r_1}{r_2} + 1\right)\chi'_{m1}, \tag{5.1}$$

for TE_{m1} modes, when $m > 0$

$$f_c = \frac{1}{2\pi\left(r_1 - r_2\right)\sqrt{\mu_0\epsilon_0}}\left(\frac{r_1}{r_2} - 1\right)\chi'_{mn}, \tag{5.2}$$

for TE_{mn} modes, when $n > 1$ and

$$f_c = \frac{1}{2\pi\left(r_1 - r_2\right)\sqrt{\mu_0\epsilon_0}}\left(\frac{r_1}{r_2} - 1\right)\chi_{mn}, \tag{5.3}$$

for TM_{mn} modes. The term χ_{mn} is defined by the n^{st} non-vanishing root of the m^{th}-order Bessel-Neumann combination function, $Z_m\left(\frac{r_2}{r_1}\chi_{mn}\right)$, and as χ'_{mn} for the n^{st} non-vanishing root of the derivative of the m^{th}-order *Bessel-Neumann* Combination Function, $Z'_m\left(\frac{r_2}{r_1}\chi'_{mn}\right)$.

The walls of the waveguides are metallic, which means they are imperfect conductors, and thus there is power loss during signal propagation down the pipe. The attenuation constant is defined by the conductor losses, α_c. In this section are outlined the analytical expressions of the attenuation constants (5.4), (5.5), (5.6) for the TEM, TE, and TM modes respectively considering coaxial waveguide as they are given by [56]:

$$\alpha_c = \left(\frac{R_{s1}}{r_1} + \frac{R_{s2}}{r_2}\right)\frac{1}{2\zeta ln\frac{r_1}{r_2}}, \tag{5.4}$$

$$\alpha_c = \frac{\left[\frac{R_{s1}}{r_1}\frac{J_m'^2(\chi'_{mn})}{J_m'^2\left(\frac{r_1}{r_2}\chi'_{mn}\right)}\left(\frac{r_2}{r_1}\right)^2 + \frac{R_{s2}}{r_2}\right]\frac{1}{\zeta}\frac{m^2}{\chi'^2_{mn}}\sqrt{1-\left(\frac{\lambda}{\lambda_c}\right)^2}}{\frac{J_m'^2(\chi'_{mn})}{J_m'^2\left(\frac{r_1}{r_2}\chi'_{mn}\right)}\left[1-\frac{m^2}{\frac{r_1}{r_2}\chi'^2_{mn}}\right]-\left[1-\frac{m^2}{\chi'^2_{mn}}\right]} + \frac{\left[\frac{R_{s1}}{r_1}\frac{J_m'^2(\chi'_{mn})}{J_m'^2\left(\frac{r_1}{r_2}\chi'_{mn}\right)} + \frac{R_{s2}}{r_2}\right]\frac{1}{\zeta}\frac{\left(\frac{\lambda}{\lambda_c}\right)^2}{\sqrt{1-\left(\frac{\lambda}{\lambda_c}\right)^2}}}{\frac{J_m'^2(\chi'_{mn})}{J_m'^2\left(\frac{r_1}{r_2}\chi'_{mn}\right)}\left[1-\frac{m^2}{\frac{r_1}{r_2}\chi'^2_{mn}}\right]-\left[1-\frac{m^2}{\chi'^2_{mn}}\right]} \tag{5.5}$$

$$\alpha_c = \left[\frac{\frac{R_{s1}}{r_1}\frac{J_m^2(\chi_{mn})}{J_m^2\left(\frac{r_1}{r_2}\chi_{mn}\right)} + \frac{R_{s2}}{r_2}}{\frac{J_m^2(\chi_{mn})}{J_m^2\left(\frac{r_1}{r_2}\chi_{mn}\right)}-1}\right]\frac{1}{\zeta\sqrt{1-\left(\frac{\lambda}{\lambda_c}\right)^2}}, \tag{5.6}$$

The R_{s1} and R_{s2} terms are the characteristic resistance of the outer and inner conductors respectively, which are defined by $\sqrt{\frac{\omega\mu}{2\sigma}}$ [32].

Equations (5.1) to (5.6) present the cut-off frequencies and the attenuation constants due to conductivity of the wall in a coaxial metallic waveguide. Reported below are the numerical results of those equations in comparison with the simulated results for various cases (see Table 5.1 - 5.6). The cases are divided into the following categories: the type of the metal wall (aluminium or carbon steel 1010), the radius of the coaxial waveguide (57.15 mm, 122.2375 mm and 69.85 mm, 136.525 mm), and the relative permittivity of the filling material (ϵ_r = 1, 1.5, 2) of the waveguide. Due to the magnetic properties of the carbon steel 1010, a short study is presented where it is shown the relationship between the attenuation constant of the TE_{11} mode of the coaxial waveguide made by carbon steel 1010 with a radius of 69.85 mm, 136.525 mm with the relative magnetic permeability (μ_r). The results are compared with the respected simulated results (Fig. 5.2). The values of the types of the metal walls, the radius, and the relative permittivity of the filling material are typical in the oil and gas industry, as already have been described in Section 4.2.1.

In a waveguide each propagating mode also has its own group velocity which is given by $\upsilon_g = \frac{c\beta}{k}$, where c is the speed of light (2.998×10^8 m/sec) and β is defined the phase constant which is given by $\beta = \sqrt{k^2 - k_c^2}$. Here k_c is the cut-off wavenumber and $k = \omega\sqrt{\mu\epsilon}$, for all modes [32]. The cut-off wavenumber, in a coaxial waveguide is given by $k_c = \frac{\left(\frac{r_1}{r_2}+1\right)\chi'_{m1}}{r_1+r_2}$, for the TE_{m1} modes, $k_c = \frac{\left(\frac{r_1}{r_2}-1\right)\chi'_{m1}}{r_1-r_2}$, for the TE_{mn} modes, when $n > 1$, and, $k_c = \frac{\left(\frac{r_1}{r_2}-1\right)\chi_{mn}}{r_1-r_2}$, for the TM_{mn} modes [32], [56]. Following these definitions, the group velocities can be defined as follows:

$$\upsilon_g = \frac{c\sqrt{\left(\omega\sqrt{\mu\epsilon}\right)^2 - \left(\frac{\left(\frac{r_1}{r_2}+1\right)\chi'_{m1}}{r_1+r_2}\right)^2}}{\omega\sqrt{\mu\epsilon}} \tag{5.7}$$

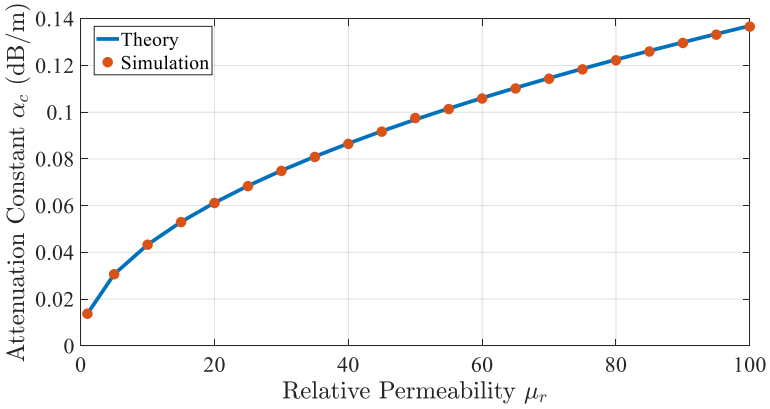

Figure 5.2: Attenuation constant of the TEM mode due to the conductivity of the metallic walls. The metallic walls are made of carbon steel 1010. The relative permeability of the material begins from 1 and gradually increases to 100. Numerical results are compared with simulations.

Mode	Cut-off Frequency (GHz)		α_c (dB/m) Aluminum Walls		α_c (dB/m) Steel 1010 Walls	
	Theory	Sim.	Theory	Sim.	Theory	Sim.
TEM	all frequencies		0.006	0.006	0.138	0.137
TE_{11}	0.469	0.469	0.006	0.006	0.137	0.136
TE_{21}	0.929	0.930	0.006	0.006	0.140	0.139
TE_{31}	1.373	1.374	0.007	0.007	0.155	0.154
TE_{41}	1.800	1.801	0.009	0.009	0.201	0.199
TE_{51}	2.209	2.210	0.017	0.017	0.384	0.385
TM_{01}	2.237	2.235	0.032	0.031	0.711	0.712
TE_{01}	2.286	2.285	0.034	0.034	0.765	0.765
TM_{11}	2.286	2.287	0.036	0.036	0.810	0.811
TE_{12}	2.344	2.344	0.048	0.047	1.085	1.086

Table 5.1: $r_1 = 136.525$ mm, $r_2 = 69.85$ mm - $\epsilon_r = 1$

for TE_{m1} modes, when $m > 0$, and

$$v_g = \frac{c\sqrt{\left(\omega\sqrt{\mu\epsilon}\right)^2 - \left(\frac{\left(\frac{r_1}{r_2}-1\right)\chi'_{m1}}{r_1-r_2}\right)^2}}{\omega\sqrt{\mu\epsilon}} \tag{5.8}$$

for TE_{mn} modes, when $n > 1$, and

Mode	Cut-off Frequency (GHz)		α_c (dB/m) Aluminum Walls		α_c (dB/m) Steel 1010 Walls	
	Theory	Sim.	Theory	Sim.	Theory	Sim.
TEM	all frequencies		0.006	0.006	0.144	0.143
TE_{11}	0.541	0.541	0.006	0.006	0.143	0.142
TE_{21}	1.067	1.067	0.007	0.006	0.146	0.145
TE_{31}	1.566	1.567	0.008	0.008	0.172	0.171
TE_{41}	2.034	2.035	0.012	0.012	0.277	0.277
TM_{01}	2.288	2.287	0.039	0.038	0.878	0.879
TE_{01}	2.353	2.351	0.049	0.049	1.113	1.111
TM_{11}	2.353	2.351	0.056	0.055	1.262	1.263

Table 5.2: $r_1 = 122.2375$ mm, $r_2 = 57.15$ mm - $\epsilon_r = 1$

Mode	Cut-off Frequency (GHz)		α_c (dB/m) Aluminum Walls		α_c (dB/m) Steel 1010 Walls	
	Theory	Sim.	Theory	Sim.	Theory	Sim.
TEM	all frequencies		0.007	0.007	0.168	0.167
TE_{11}	0.383	0.383	0.007	0.007	0.167	0.166
TE_{21}	0.758	0.759	0.007	0.007	0.167	0.166
TE_{31}	1.121	1.121	0.008	0.008	0.173	0.172
TE_{41}	1.470	1.471	0.009	0.009	0.198	0.199
TE_{51}	1.803	1.805	0.011	0.011	0.259	0.258
TM_{01}	1.827	1.825	0.022	0.021	0.486	0.485
TM_{11}	1.867	1.865	0.021	0.021	0.480	0.480
TE_{01}	1.867	1.865	0.013	0.014	0.290	0.290
TE_{12}	1.914	1.913	0.014	0.014	0.325	0.324
TM_{21}	1.982	1.982	0.021	0.021	0.472	0.470
TE_{22}	2.049	2.048	0.020	0.019	0.441	0.440
TE_{61}	2.126	2.127	0.019	0.019	0.421	0.423
TM_{31}	2.161	2.161	0.023	0.022	0.512	0.510
TE_{32}	2.261	2.261	0.035	0.034	0.788	0.789
TM_{41}	2.384	2.384	0.070	0.069	1.561	1.559

Table 5.3: $r_1 = 136.525$ mm, $r_2 = 69.85$ mm - $\epsilon_r = 1.5$

$$v_g = \frac{c\sqrt{\left(\omega\sqrt{\mu\epsilon}\right)^2 - \left(\frac{\left(\frac{r_1}{r_2}-1\right)\chi_{m1}}{r_1-r_2}\right)^2}}{\omega\sqrt{\mu\epsilon}} \tag{5.9}$$

for TM_{mn} modes. The group velocity of the TEM mode is equal to the speed of light, i.e., 2.998×10^8 m/sec [32].

Given these conditions, the group velocities considering the defined coaxial waveguide are outlined in Table 5.7. Also, all the numerical findings in Table 5.7 are verified

Mode	Cut-off Frequency (GHz)		α_c (dB/m) Aluminum Walls		α_c (dB/m) Steel 1010 Walls	
	Theory	Sim.	Theory	Sim.	Theory	Sim.
TEM	all frequencies		0.008	0.008	0.175	0.176
TE_{11}	0.442	0.439	0.008	0.008	0.173	0.173
TE_{21}	0.871	0.869	0.008	0.008	0.171	0.170
TE_{31}	1.278	1.278	0.008	0.008	0.184	0.182
TE_{41}	1.663	1.662	0.010	0.010	0.232	0.231
TM_{01}	1.868	1.867	0.023	0.023	0.507	0.516
TE_{01}	1.921	1.919	0.014	0.016	0.327	0.325
TM_{11}	1.921	1.919	0.023	0.023	0.511	0.510
TE_{12}	1.984	1.982	0.017	0.017	0.380	0.378
TE_{51}	2.029	2.029	0.016	0.016	0.364	0.365
TM_{21}	2.068	2.067	0.023	0.023	0.514	0.516
TE_{22}	2.166	2.164	0.026	0.026	0.585	0.582
TM_{31}	2.293	2.292	0.032	0.032	0.714	0.714
TE_{61}	2.384	2.384	0.089	0.091	2.017	1.981

Table 5.4: $r_1 = 122.2375$ mm, $r_2 = 57.15$ mm - $\epsilon_r = 1.5$

Mode	Cut-off Frequency (GHz)		α_c (dB/m) Aluminum Walls		α_c (dB/m) Steel 1010 Walls	
	Theory	Sim.	Theory	Sim.	Theory	Sim.
TEM	all frequencies		0.009	0.009	0.194	0.194
TE_{11}	0.332	0.330	0.009	0.009	0.193	0.192
TE_{21}	0.657	0.655	0.008	0.008	0.189	0.188
TE_{31}	0.971	0.971	0.009	0.008	0.192	0.190
TE_{41}	1.273	1.273	0.009	0.009	0.209	0.206
TE_{51}	1.562	1.562	0.011	0.011	0.250	0.248
TM_{01}	1.581	1.579	0.021	0.022	0.480	0.484
TM_{11}	1.615	1.614	0.021	0.021	0.479	0.472
TE_{01}	1.615	1.615	0.010	0.013	0.214	0.213
TE_{12}	1.657	1.655	0.011	0.011	0.241	0.240
TM_{21}	1.715	1.714	0.019	0.020	0.440	0.441
TE_{22}	1.774	1.772	0.014	0.014	0.319	0.316
TE_{61}	1.842	1.841	0.015	0.015	0.331	0.331
TM_{31}	1.870	1.868	0.018	0.018	0.408	0.412
TE_{32}	1.958	1.956	0.020	0.020	0.447	0.443
TM_{41}	2.064	2.063	0.018	0.019	0.411	0.414
TE_{71}	2.113	2.113	0.023	0.023	0.510	0.514
TE_{42}	2.195	2.192	0.031	0.031	0.705	0.699
TM_{51}	2.288	2.287	0.025	0.026	0.571	0.572
TE_{81}	2.381	2.380	0.099	0.101	2.229	2.177

Table 5.5: $r_1 = 136.525$ mm, $r_2 = 69.85$ mm - $\epsilon_r = 2$

Mode	Cut-off Frequency (GHz)		α_c (dB/m) Aluminum Walls		α_c (dB/m) Steel 1010 Walls	
	Theory	Sim.	Theory	Sim.	Theory	Sim.
TEM	all frequencies		0.009	0.009	0.203	0.203
TE_{11}	0.383	0.382	0.009	0.009	0.200	0.199
TE_{21}	0.754	0.754	0.009	0.009	0.194	0.192
TE_{31}	1.107	1.107	0.009	0.009	0.200	0.197
TE_{41}	1.440	1.441	0.010	0.010	0.233	0.231
TM_{01}	1.617	1.616	0.022	0.023	0.497	0.507
TM_{11}	1.662	1.662	0.022	0.021	0.491	0.491
TE_{01}	1.662	1.662	0.011	0.013	0.235	0.234
TE_{12}	1.718	1.717	0.012	0.012	0.274	0.272
TE_{51}	1.758	1.758	0.014	0.014	0.310	0.310
TM_{21}	1.791	1.791	0.020	0.020	0.452	0.455
TE_{22}	1.876	1.874	0.017	0.017	0.383	0.382
TM_{31}	1.986	1.985	0.019	0.019	0.433	0.436
TE_{61}	2.065	2.065	0.021	0.022	0.484	0.486
TE_{32}	2.119	2.117	0.026	0.026	0.597	0.594
TM_{41}	2.227	2.226	0.023	0.023	0.520	0.522
TE_{71}	2.366	2.366	0.076	0.076	1.722	1.686

Table 5.6: $r_1 = 122.2375$ mm, $r_2 = 57.15$ mm - $\epsilon_r = 2$

Mode	Group Velocity v_g m/s $\times 10^8$	
	Theory	Sim.
TEM	2.998	2.998
TE_{11}	2.940	2.942
TE_{21}	2.765	2.765
TE_{31}	2.460	2.457
TE_{41}	1.985	1.981
TE_{51}	1.178	1.169
TM_{01}	1.096	1.135
TE_{01}	0.918	0.969
TM_{11}	0.918	0.969
TE_{12}	0.655	0.724

Table 5.7: Group velocities for the possible modes of the selected coaxial waveguide. Theoretical values are compared to the CST Studio Suite EM simulations

by the CST Studio Suite EM simulation software, and the results are in agreement.

5.2.3 Power Loss & Power Flow

This subsection provides a derivation for the TEM, TE and TM power flow equations of a coaxial waveguide and these equations are useful when calculating the attenuation

constants, see (5.4), (5.5), and (5.6).

General modal equations are initially defined and expanded upon herein for the coaxial waveguide starting from the preliminary analytical expressions for the possible electromagnetic field components by introducing the complete sinusoidal equations, which leads to an analysis of the power flow and attenuation within the coaxial metallic pipeline. More specifically, while (5.14) and (5.15) were originally defined in [32] and in [75], respectively, (5.16) was needed to further be developed based on the initial findings from [32], [56], and [75]. As a first step, this is achieved by considering all constants A, B, C and D, thus providing an advancement from [32], [56], [75].

The electric and magnetic fields for the TEM mode are given by (5.14). The Z_0 $\left(= \eta \ln \frac{r_1}{r_2}/2\pi\right)$ is the characteristic impedance of the coaxial line, V_0 is the voltage across the line at z = 0, amd η is the intrinsic admittance of the medium. On the other hand, the electromagnetic field components for the higher order TE_{mn} and TM_{mn} modes are given by (5.15), and (5.16), respectively. Also, the β term is the propagation phase constant for the relevant mode, J_m is the mth-order 1st Bessel function, and J'_m is the derivative of it. Also, Y_m is the mth-order 2nd Bessel function and Y'_m is the derivative of it.

The power loss and power flow analytical expressions are described below. These expressions are presented and fully developed for each mode and are based on the original electromagnetic theory outlined in [32], [56], [75]. This is needed because terms such as the TEM, TE, and TM power flow and loss (5.17) and (5.21) have not been well defined in the open literature. These proofs result in a new set of equations for the TE and TM modes: see results in (5.19), (5.20), (5.22), and (5.23).

To start the derivation, the power loss per unit length along the line can be defined by [75] $P_\ell = \frac{R_s}{2} \int_{\mathbf{S}} |\mathbf{J}_s| \, \mathrm{d}s$. Here, $\mathbf{J}_s$ is the surface current for the interior surface of the coaxial pipe. The coaxial waveguide's derivation of the power loss equations follows next and when cylindrical coordinates are adopted. For the TEM modes, the power loss is given by (5.17). Moreover for the TE_{mn} mode the power loss is given by (5.18). Also, when applying boundary conditions, a relation between C and D can be derived and is given by

$$\begin{cases} CJ'_m(k_c r_1) + DY'_m(k_c r_1) = 0 \\ CJ'_m(k_c r_2) + DY'_m(k_c r_2) = 0 \Rightarrow \end{cases} \tag{5.10}$$

$$D = -C\frac{J'_m(k_c r_1)}{Y'_m(k_c r_1)} = -C\frac{J'_m(k_c r_2)}{Y'_m(k_c r_2)} = C\gamma, \tag{5.11}$$

where,

$$\gamma_{\mathrm{TE}_{mn}} = -\frac{J'_m(k_c r_1)}{Y'_m(k_c r_1)} = -\frac{J'_m(k_c r_2)}{Y'_m(k_c r_2)}. \tag{5.12}$$

Also, (5.18) can be written as in (5.19). Following the same procedure, the power loss for the TM_{mn} modes is given by (5.20), but here, because of the boundary conditions,

$$\gamma_{\mathrm{TM}_{mn}} = -\frac{J_m(k_c r_1)}{Y_m(k_c r_1)} = -\frac{J_m(k_c r_2)}{Y_m(k_c r_2)}. \tag{5.13}$$

The power flow is defined as function of the Poynting vector ($\mathbf{S}$) by the general expression $P_0 = \oint_{\mathbf{S}} \mathbf{S} \cdot \mathrm{d}\mathbf{s} = \oint_{\mathbf{S}} \mathbf{E} \times \mathbf{H}^{\star} \cdot \mathrm{d}\mathbf{s}$. Therefore the power flow for the TEM modes is given by (5.21). The integrals for the calculation of the power flow of the TE$_{mn}$ and TM$_{mn}$ modes are quite complicated, hence the following property is used for the calculation as well as the attenuation constant: $\alpha_c = \frac{P_\ell}{2P_0}$ which leads to (5.4), (5.5), and (5.6) as described further next.

$$\text{TEM}: \quad \begin{cases} \mathbf{E}_\rho = \frac{V_0}{\rho \ln \frac{r_1}{r_2}} e^{-j\beta \mathrm{z}} \\ \mathbf{E}_\phi = 0 \\ \mathbf{E}_\mathrm{z} = 0 \\ \mathbf{H}_\rho = 0 \\ \mathbf{H}_\phi = \frac{V_0}{2\pi\rho Z_0} e^{-j\beta \mathrm{z}} \\ \mathbf{H}_\mathrm{z} = 0 \end{cases} \tag{5.14}$$

$$\text{TE}_{mn}: \quad \begin{cases} \mathbf{E}_\rho = -\frac{j\omega\mu m}{k_c^2 \rho} \left(A\mathrm{cos}m\phi - B\mathrm{sin}m\phi\right) \left(CJ_m(k_c\rho) + DY_m(k_c\rho)\right) e^{-j\beta \mathrm{z}} \\ \mathbf{E}_\phi = \frac{j\omega\mu}{k_c} \left(A\mathrm{sin}m\phi + B\mathrm{cos}m\phi\right) \left(CJ'_m(k_c\rho) + DY'_m(k_c\rho)\right) e^{-j\beta \mathrm{z}} \\ \mathbf{E}_\mathrm{z} = 0 \\ \mathbf{H}_\rho = -\frac{j\beta}{k_c} \left(A\mathrm{sin}m\phi + B\mathrm{cos}m\phi\right) \left(CJ'_m(k_c\rho) + DY'_m(k_c\rho)\right) e^{-j\beta \mathrm{z}} \\ \mathbf{H}_\phi = -\frac{j\beta m}{k_c^2 \rho} \left(A\mathrm{cos}m\phi - B\mathrm{sin}m\phi\right) \left(CJ_m(k_c\rho) + DY_m(k_c\rho)\right) e^{-j\beta \mathrm{z}} \\ \mathbf{H}_\mathrm{z} = \left(A\mathrm{sin}m\phi + B\mathrm{cos}m\phi\right) \left(CJ_m(k_c\rho) + DY_m(k_c\rho)\right) e^{-j\beta \mathrm{z}} \end{cases} \tag{5.15}$$

$$\text{TM}_{mn}: \quad \begin{cases} \mathbf{E}_\rho = -\frac{j\beta}{k_c} \left(A\mathrm{sin}m\phi + B\mathrm{cos}m\phi\right) \left(CJ'_m(k_c\rho) + DY'_m(k_c\rho)\right) e^{-j\beta \mathrm{z}} \\ \mathbf{E}_\phi = -\frac{j\beta m}{k_c^2 \rho} \left(A\mathrm{cos}m\phi - B\mathrm{sin}m\phi\right) \left(CJ_m(k_c\rho) + DY_m(k_c\rho)\right) e^{-j\beta \mathrm{z}} \\ \mathbf{E}_\mathrm{z} = \left(A\mathrm{sin}m\phi + B\mathrm{cos}m\phi\right) \left(CJ_m(k_c\rho) + DY_m(k_c\rho)\right) e^{-j\beta \mathrm{z}} \\ \mathbf{H}_\rho = \frac{j\omega\epsilon m}{k_c^2 \rho} \left(A\mathrm{cos}m\phi - B\mathrm{sin}m\phi\right) \left(CJ_m(k_c\rho) + DY_m(k_c\rho)\right) e^{-j\beta \mathrm{z}} \\ \mathbf{H}_\phi = \frac{j\omega\epsilon}{k_c} \left(A\mathrm{sin}m\phi + B\mathrm{cos}m\phi\right) \left(CJ'_m(k_c\rho) + DY'_m(k_c\rho)\right) e^{-j\beta \mathrm{z}} \\ \mathbf{H}_\mathrm{z} = 0 \end{cases} \tag{5.16}$$

Combining (5.5), (5.6), (5.19), and (5.20) the power flow and the attenuation constant can be determined in general form whilst considering important variables for this chapter such as the finite conductivity of pipeline materials as well as the relative power loss for each mode. Expression (5.22) describes the power flow for the TE$_{mn}$ modes and (5.23) describes the power flow for the TM$_{mn}$ modes while attenuation constants are outlined in (5.4), (5.5), and (5.6). To the best knowledge of the author, never before has such a power flow analysis, which is now linked to the calculation of the attenuation constants and the different TE and TM modes, been reported previously in the open literature in this most general form.

$$\begin{aligned} P_{\ell_{\mathrm{TEM}}} &= \frac{R_{s_1}}{2} \int_{\phi=0}^{2\pi} |H_\phi|^2_{\rho=r_1} \, r_1 \mathrm{d}\phi + \frac{R_{s_2}}{2} \int_{\phi=0}^{2\pi} |H_\phi|^2_{\rho=r_2} \, r_2 \mathrm{d}\phi \\ &= \frac{V_0^2}{4\pi Z_0^2} \left(\frac{R_{s_1}}{r_1} + \frac{R_{s_2}}{r_2} \right) \end{aligned} \tag{5.17}$$

$$
\begin{aligned}
P_{\ell_{\mathrm{TE}mn}} &= \frac{R_{s_1}}{2}\int_{\phi=0}^{2\pi}\left(|H_\phi|^2_{\rho=r_1}+|H_z|^2_{\rho=r_1}\right)r_1\mathrm{d}\phi \\
&+ \frac{R_{s_2}}{2}\int_{\phi=0}^{2\pi}\left(|H_\phi|^2_{\rho=r_2}+|H_z|^2_{\rho=r_2}\right)r_2\mathrm{d}\phi \qquad (5.18)\\
&= \frac{\pi\left(A^2+B^2\right)C^2}{2}\left[R_{s_1}\left(J_m(k_cr_1)+\gamma Y_m(k_cr_1)\right)^2 r_1\left(1+\frac{\beta^2m^2}{k_c^4r_1}\right)\right.\\
&\left.+R_{s_2}\left(J_m(k_cr_2)+\gamma Y_m(k_cr_2)\right)^2 r_2\left(1+\frac{\beta^2m^2}{k_c^4r_2}\right)\right] \qquad (5.19)
\end{aligned}
$$

$$
\begin{aligned}
P_{\ell_{\mathrm{TM}mn}} &= \frac{\pi\omega^2\epsilon^2\left(A^2+B^2\right)C^2}{2k_c^2}\left[R_{s_1}\left(J'_m(k_cr_1)+\gamma Y'_m(k_cr_1)\right)^2 r_1\right.\\
&\left.+R_{s_2}\left(J'_m(k_cr_2)+\gamma Y'_m(k_cr_2)\right)^2 r_2\right] \qquad (5.20)
\end{aligned}
$$

$$
\begin{aligned}
P_{0_{\mathrm{TEM}}} &= \frac{1}{2}\mathrm{Re}\int_{\rho=r_2}^{r_1}\int_{\phi=0}^{2\pi}\mathbf{E}\times\mathbf{H}^\star\cdot\hat{z}\rho\mathrm{d}\phi\mathrm{d}\rho\\
&= \frac{1}{2}\mathrm{Re}\int_{r_2}^{r_1}\int_{\phi=0}^{2\pi}\left(E_\rho H_\phi^\star - E_\phi H_\rho^\star\right)\rho\mathrm{d}\phi\mathrm{d}\rho = \frac{V_0^2}{2Z_0} \qquad (5.21)
\end{aligned}
$$

$$
P_{0_{\mathrm{TE}mn}} = \frac{\frac{\pi\left(A^2+B^2\right)C^2}{2}\left[R_{s_1}\left(J_m(k_cr_1)+\gamma Y_m(k_cr_1)\right)^2 r_1\left(1+\frac{\beta^2m^2}{k_c^4r_1}\right)+R_{s_2}\left(J_m(k_cr_2)+\gamma Y_m(k_cr_2)\right)^2 r_2\left(1+\frac{\beta^2m^2}{k_c^4r_2}\right)\right]}{2\left[\frac{R_{s1}}{r_1}\frac{J'^2_m(\chi'_{mn})}{J'^2_m\left(\frac{r_1}{r_2}\chi'_{mn}\right)}\left(\frac{r_2}{r_1}\right)^2+\frac{R_{s2}}{r_2}\right]\frac{1}{\zeta}\frac{m^2}{\chi'^2_{mn}}\sqrt{1-\left(\frac{\lambda}{\lambda_c}\right)^2}+\left[\frac{R_{s1}}{r_1}\frac{J'^2_m(\chi'_{mn})}{J'^2_m\left(\frac{r_1}{r_2}\chi'_{mn}\right)}+\frac{R_{s2}}{r_2}\right]\frac{1}{\zeta}\frac{\left(\frac{\lambda}{\lambda_c}\right)^2}{\sqrt{1-\left(\frac{\lambda}{\lambda_c}\right)^2}}} \qquad (5.22)
$$
$$
\frac{\frac{J'^2_m(\chi'_{mn})}{J'^2_m\left(\frac{r_1}{r_2}\chi'_{mn}\right)}\left[1-\frac{m^2}{\frac{r_1}{r_2}\chi'^2_{mn}}\right]-\left[1-\frac{m^2}{\chi'^2_{mn}}\right]}
$$

$$
P_{0_{\mathrm{TM}mn}} = \frac{\frac{\pi\omega^2\epsilon^2\left(A^2+B^2\right)C^2}{2k_c^2}\left[R_{s_1}\left(J'_m(k_cr_1)+\gamma Y'_m(k_cr_1)\right)^2 r_1+R_{s_2}\left(J'_m(k_cr_2)+\gamma Y'_m(k_cr_2)\right)^2 r_2\right]}{2\left[\frac{\frac{R_{s1}}{r_1}\frac{J^2_m(\chi_{mn})}{J^2_m\left(\frac{r_1}{r_2}\chi_{mn}\right)}+\frac{R_{s2}}{r_2}}{\frac{J^2_m(\chi_{mn})}{J^2_m\left(\frac{r_1}{r_2}\chi_{mn}\right)}-1}\right]\frac{1}{\zeta\sqrt{1-\left(\frac{\lambda}{\lambda_c}\right)^2}}} \qquad (5.23)
$$

5.3 Liquid Level Determination Considering the Dominant TEM Mode

As an initial study of the proposed liquid level system, a simulation model was developed considering a coaxial carbon steel 1010 waveguide with radii 69.85 mm and 136.525 mm for unimodal propagation. This study helps to understand better the reflections of the Gaussian signal related to the various liquid types and the velocity of the propagated signal throughout its travelling time and distance and compare it with the group velocity of the TEM mode. Additionally, this is developed as a link budget equation which was the basis for the final link budget equation for the developed experimental system.

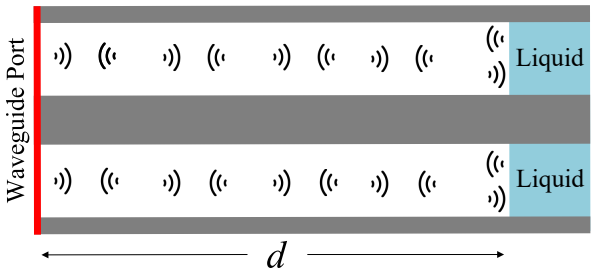

Figure 5.3: Simulated setup for liquid level determination considering single mode operation for the pipe.

5.3.1 Testing System & the Liquid Properties

In this study, the signal was excited by a waveguide port, as illustrated in Fig. 5.3. A Gaussian pulse was excited by a waveguide port for propagation within the coaxial waveguide (outer pipe). In particular, the excited signal is a time-domain Gaussian pulse which can be described by the function $G(x) = \frac{1}{\sigma\sqrt{2\pi}} e^{-\frac{(x-\mu)^2}{2\sigma^2}}$ [76], where σ is the standard deviation with a value of 0.8518 and μ is the mean of the distribution with a value with 4.4324, in this case (see Fig. 5.4). The chosen bandwidth to be simulated was from 0 to 400 MHz. Also, the time signal was defined from 0 to 9 ns. In this bandwidth only the dominant TEM mode is propagated (see Table 5.1. This approach simplifies the system and thus verifies the feasibility of the system. Also, the attenuation constant at this frequency is 0.056 dB/m, and the distance (d) between the waveguide port (point of excitation) and the liquid level is 1-meter. The signal is reflected from the liquid boundary layer, and the waveguide port captures the returned reflection signal.

To verify the methodology, the excited and the reflected signals for three different liquids were studied: water, seawater, and a hydrocarbon lubricating oil. These three liquids and some combinations of them are met in the oil and gas annulus region, typically, as it was explained in Subsection 2.4. The electric properties of those liquids are shown in the Table 5.8. The complex relative permittivity of water, and the oil has a dependence on the frequency and the temperature, which is given by [77]

$$\varepsilon(f,T) = \varepsilon'(f,T) - j\varepsilon''(f,T), \tag{5.24}$$

where f is the frequency. In the case of seawater, the salinity is considered for the complex relative permittivity, as well, and it is given by [78]

$$\varepsilon(f,T,S) = \varepsilon'(f,T,S) - j\varepsilon''(f,T,S), \tag{5.25}$$

where ε', ε'' are the real and the imaginary parts of the complex relative permittivity, respectively, and S is the salinity. Accordingly, the conductivity is given by [32]

$$\sigma = \omega\varepsilon' \tan\delta - \omega\varepsilon''. \tag{5.26}$$

In the literature, there are several models for the calculation of the exact values of the 5.24 and 5.25. The most common is the Debye and the Wentz models [79]. For this study the values are given by the CST Suite studio for the frequency of the 400 MHz, at 20° C, and salinity at 3% [80]. The values of the complex relative permittivity and the conductivity are shown in the Table 5.8.

Liquid	ε'	ε''	σ (S/m)	L_{Liquid} (%)	$\mid S_{11} \mid$ (dB)
Water	78	7.35	0.005	13.97	-2.14
Seawater	74	≈ 0	3.53	15.48	-1.350
Oil	2.33	0.4	0	-	-15.636

Table 5.8: Electric properties of the testing liquid, as well as, the volume losses (L_{Liquid}). The reflection coefficient of the waveguide port is also reported

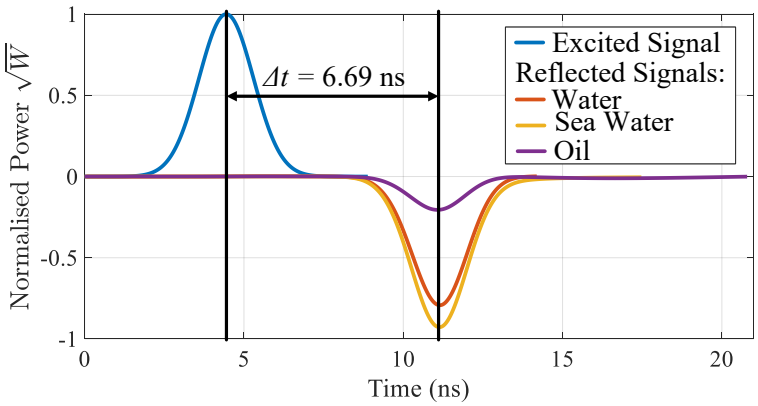

Figure 5.4: Excited and reflected pulses by water, seawater, and oil.

5.3.2 Travelling Time of the Signal & Link Budget Equation

The excited Gaussian pulse and the reflected pulses by the water, the seawater, and the liquid oil samples are reported in Fig. 5.4. Also, in this figure, the power of the pulse was normalized. The reflected power has negative power values because the waveguide port accepts it, and magnitude values are both about 0.8 for the water and 0.9 for the seawater case as it has greater conductivity (see Table 5.8). This suggests a modest absorption of power into liquid. On the other hand, oil appears to have more adsorbing properties (see Table 5.8). Regardless, the time difference (Δt) between the exciting pulse and the reflected pulse is 6.69 ns and represents the total travel time of the signal, i.e., the forward and backward paths. Based on the group velocity (v_g) of the TEM mode (2.998×10^8 m/sec) and the total travelling time (Δt) the total travelled distance can be calculated, and in this introductory simulation study, is known to be 2-meters (since the length of the physical pipe is 1-meter). Hence, the distance between the excitation and the liquid level was 1 m as the velocity of the signal is constant within the unimodal pipeline as the TEM mode is dominant.

Additionally, the travelling time of the signal is independent of the liquid type contained at the bottom of the pipeline. The travelling time is dependent on the group velocity of the dominant propagated mode (TEM here) and, therefore, the environmental contents of the pipeline (air in this study case).

Following the findings in the previous section, while considering a unimodal operation, a link budget equation can be defined for the proposed microwave system. Firstly, the attenuation constant of the TEM mode is 0.056 dB/m at 400 MHz considering the parameters of the pipe. Also, the volume loss in the liquid (L_{Liquid}) due to the inci-

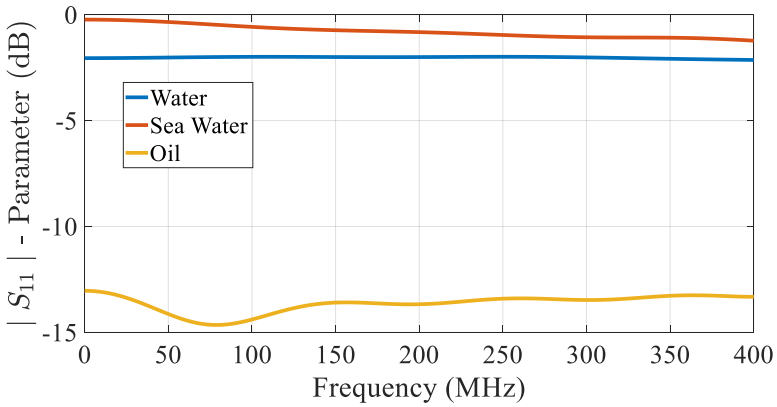

Figure 5.5: Reflection coefficient (| S_{11} |) of the waveguide port when the three different liquids are considered.

dent and reflection waves onto it can be calculated as a percentage with respect to the stimulating power at the transmitter, which was set at 0.5 W. The percentage values of L_{Liquid} at 400 MHz, for each liquid are presented in Table 5.8. Moreover, the reflection coefficient (| S_{11} |) of the applied waveguide port in each case is presented in Table 5.8.

The waveguide port in this simulated system acts as a transceiver. Therefore the reflection coefficient is described by the metallic losses ($2 \times \alpha_c \times d$), the volume losses from the liquid (L_{Liquid}), the outgoing power from the system minus the stimulated power (P_{stim}) and the reflected power by the system, which includes the reflection of the liquid. Without loss of generality, the link budget equation for this system can be given by

$$P_{Rx}\ (\text{dBm}) \approx P_{stim}\ (\text{dBm}) - \ ||\ S_{11}\ ||\ \ (\text{dB}), \tag{5.27}$$

where P_{Rx} is the received power by the waveguide port.

From Table 5.8, it can be observed that the volume loss in seawater is greater than the loss in water. Nevertheless, the reflection coefficient of the waveguide port when the seawater is considered is lower in absolute value. This is because the electrical conductivity of seawater is greater than that of water; thus, the reflected power is greater (see Fig. 5.4). On the other hand, the electrical conductivity of the hydrocarbon lubricating oil is zero, therefore, the reflected signal back to the waveguide port is relatively low, i.e., the reflection coefficient value is below -10 dB (see Fig. 5.5) suggesting that the majority of the power was absorbed.

5.4 Propagation Modeling

This section studies the pipeline when an end-fire antenna is employed as its waveguide source. Also, a mechanical housing mandrel that protects the antenna and any electronic components from the well environment and gas flow is presented. The parameters analysed here are the propagating mode and the power flow inside the annulus. Moreover, the impulse response of this enclosed environment is examined when an identical mandrel is included in the system defining the receiver.

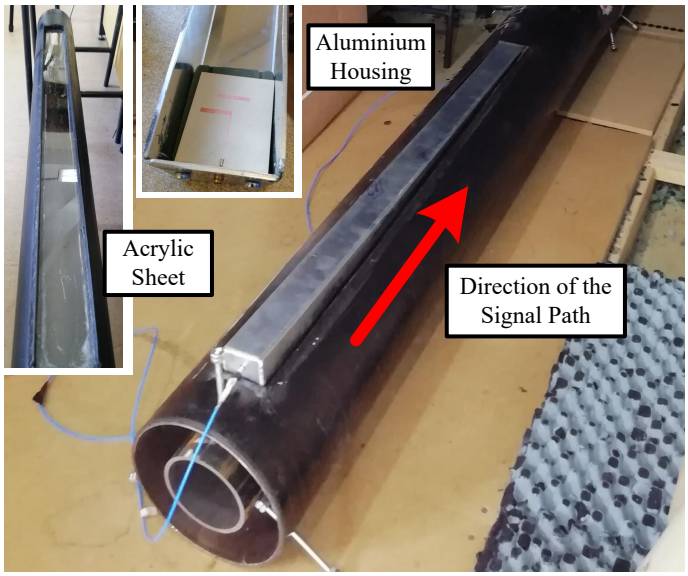

Figure 5.6: PCB Yagi-Uda antenna placed into the housing (or radome) which is installed on the top of a 2 m carbon steel 1010 section (representative of a practical mandrel rig). The red arrow shows the path of the signal from the antenna into the pipeline.

Mode	TEM	TE_{11}	TE_{21}	TE_{31}	TE_{41}
$\mid S_{21} \mid$ (dB)	-48	-21.72	**-8.15**	**-8.05**	-17.06
Mode	TE_{51}	TM_{01}	TE_{01}	TM_{11}	TE_{12}
$\mid S_{21} \mid$ (dB)	-15.22	-34.05	-11.68	-37.29	-19.21

Table 5.9: Simulated transmission coefficient ($\mid S_{21} \mid$) for determining the coupling into each mode at 2.4 GHz. The simulation setup includes a 2 m PEC waveguide pipe with the antenna positioned within the mechanical housing which was placed on top of the waveguide. An ideal waveguide port was positioned on the other side of the guide

5.4.1 Antenna Selection and Radome Housing

The selection of the optimal antenna design for directive field propagation inside the pipeline is essential for the operation of the proposed microwave reflection system. Most importantly, the antenna must fit inside the constraints imposed by the built-in housing on the top of the outer pipe and operate effectively at 2.4 GHz. For the aforesaid reasons, the same compact planar Yagi-Uda printed circuit board (PCB) antenna, which was used for the communication system (see Chapter 4), was employed for the setup herein.

As has already been mentioned, the advantage of using an end-fire antenna rather than a more conventional waveguide excitation technique is that the majority of the power flows in the desired forward direction with higher intensity because of the directivity. This is important as the antenna could be positioned in practice (within an actual oil and gas pipeline and possibly placed at a certain depth below the surface) to monitor the reflected signal from a liquid interface. As such, it is desired to ensure

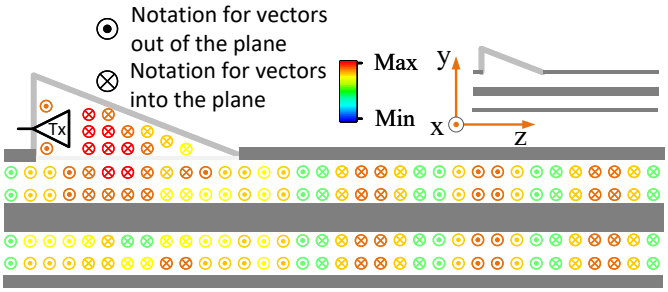

Figure 5.7: Simulated longitudinal plane (y-z plane) of the electric field lines in the coaxial waveguide pipeline. Excited field distribution when the antenna housing is employed.

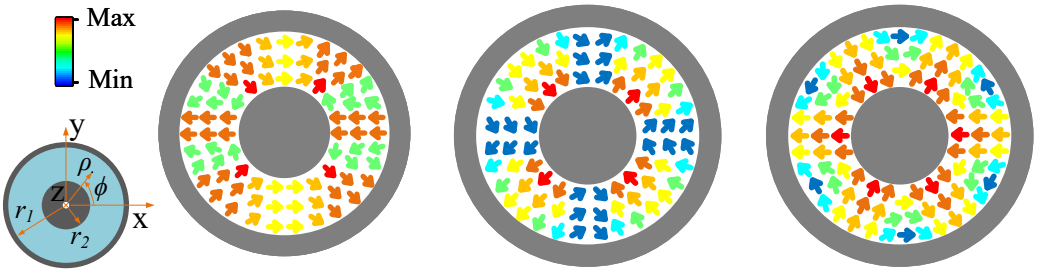

Figure 5.8: Simulated transverse plane (x-y plane) of the electric field lines in the coaxial waveguide pipeline. (a) Excited field distribution when the antenna housing is attached. As can be observed the field is defined by a superposition of the (b) TE_{21} and (c) TE_{31} modes.

uni-directional propagation down the pipe.

In an operational oil and gas flow system, the antenna and the electronic components can be exposed to high temperatures and pressures and might be damaged due to the surrounding pipeline contents and the production fluid flow [42]. For this reason, creating a sealed antenna housing, i.e., an effective radome cover will be required to provide a suitable protective environmental enclosure. Figure 5.6 shows the concept of the housing (see also Fig. 5.1a), which has been constructed from aluminum, and there is a feed through at its edge so that the antenna can be connected with a coaxial cable for experimental testing of the prototype. This housing is similar to the one that was presented in Subsection 4.4.1, but this time the length of the ramp is 1.2 meters, its maximum height is 0.05 meters, and its width is 0.068 meters. Also, the housing is placed on top of a 2-meter piece of the outer pipe, and between them, there is an acrylic sheet (see Fig. 5.6). The electromagnetic wave propagates through the acrylic sheet, and the inner core is fed while the antenna is protected. The relative dielectric constant (ϵ_r) of the acrylic sheet used is 3. Also, the antenna is polarised horizontally (as it is end-fire), and its position within the housing has been optimized for minimal reflections and maximum coupling into the pipeline. More specifically, the antenna is placed parallel to the acrylic sheet. This allows the applied power to couple into the pipeline structure with gradual injection occurring due to the long ramp inside the

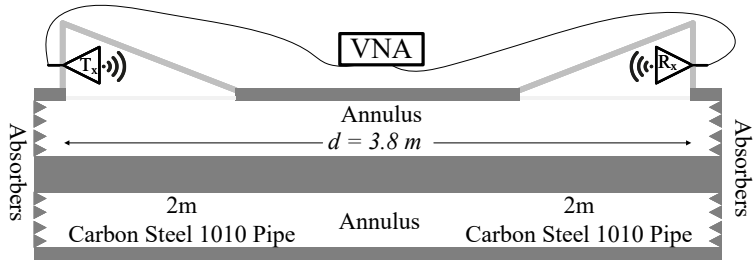

Figure 5.9: Experimental setup for the measurement of the S - parameters reported in Fig. 5.10.

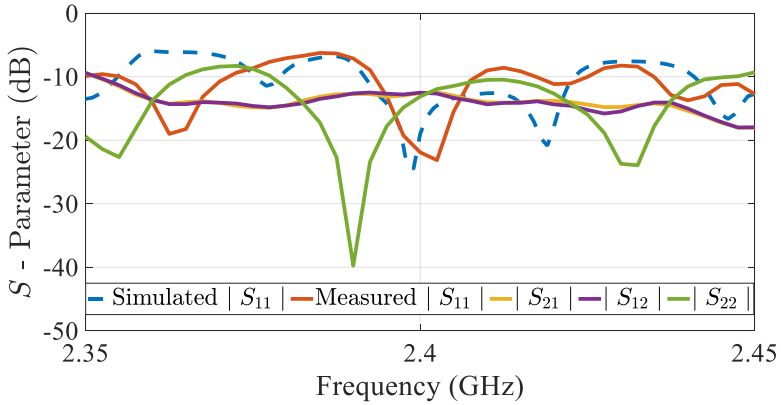

Figure 5.10: Measured S-Parameters for the system (see Fig. 5.9) when the Yagi-Uda PCB-based antennas were placed into the mechanical housings. The simulated | S_{11} | is also shown.

housing and the termination into the outer pipe.

5.4.2 Field Routing Within the Pipe

At this initial stage in the system development, it is also essential to understand how the EM fields propagate when the directive antenna is mated within its mechanical housing and the pipeline structure itself. This was accomplished by studying the field lines and the power flow along the pipeline through the simulations as described in this section. In CST, the PCB end-fire Yagi-Uda antenna was placed into the mechanical housing, which was then placed on the top of the outer pipeline section (see Fig. 5.6), defining the excitation source for the system. A waveguide port was placed at the other edge of the coax pipe. The waveguide port can be excited by all the desired modes and monitor the S-parameters results for each mode separately. The CST Studio Suite EM simulations was able to ascertain which modes were mainly excited, and this was studied by investigating the relative powers of each mode.

The results comparing the relative powers for each mode can be observed in Table 5.9. Here the transmission coefficient (| S_{21} |) represents the coupling into each mode from the driven antenna. Based on these results, the dominant modes are the TE_{21} and

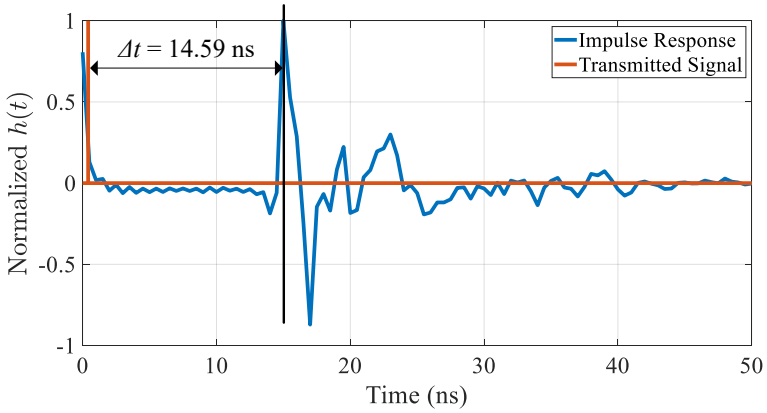

Figure 5.11: Measured impulse response of the end-to-end system (see Fig. 5.9).

TE_{31} modes as insertion loss values are minimum. This implies that the majority of power from the antenna housing excitation is coupled into the TE_{21} and TE_{31} modes of the coaxial pipeline. This is because $\mid S_{21} \mid$ values are about -8 dB, while all the other powers diverted into the different modes are about -12 dB or below. Also, as reported in Fig. 5.7, the simulated electric field distributions divert into other modes. More specifically, as it can be observed by studying Fig. 5.8 that the electric field is mainly a superposition of the electric fields of the TE_{21} and TE_{31} modes. Also, the electric field lines of the TE_{21} and TE_{31} modes can be found in [56] which are consistent with the simulations as shown in Fig. 5.8.

5.4.3 Impulse Response of the System & Antenna Effective Gain

The calculation of the impulse response requires a bi-directional communications system using a second mandrel (see Fig. 5.9). This investigation is important as it can characterize the group velocity of the propagating fields within the pipeline, and this can also indicate the fields and modes within the guide. In this study, two identical coaxial carbon steel 1010 pipes with the antenna housings installed on the top define the bi-directional transceiver system under test. Also, two identical Yagi-Uda based PCB antennas were placed into the housings and separated by a distance $d = 3.8$ m apart. To avoid power radiation leakage outside the testbed, absorbers have been placed at the ends of the pipes, thus helping to emulate a more representative oil and gas scenario where the enclosed pipeline boundary is a longer overall length.

The S-Parameters of the system was then measured using an S5048 2-Port vector network analyzer (VNA) by Copper Mountain Technologies (see Fig. 5.10). The reflection coefficients of the antennas ($\mid S_{11} \mid$) and ($\mid S_{22} \mid$) in dB for the frequency range from 2.35 to 2.45 GHz, demonstrate good matching (with values below -10 dB) and agreement is observed with the CST Studio Suite EM simulation software. It should be mentioned that, since the use of the mechanical antenna housings form a boundary with the coaxial pipeline, the reflection coefficients are not significantly altered by the pipeline length and maintain a good performance at 2.4 GHz. Also, the transmission coefficients values, ($\mid S_{21} \mid$) and ($\mid S_{12} \mid$) were observed to be around to -12.5 dB. This means that 75 % of

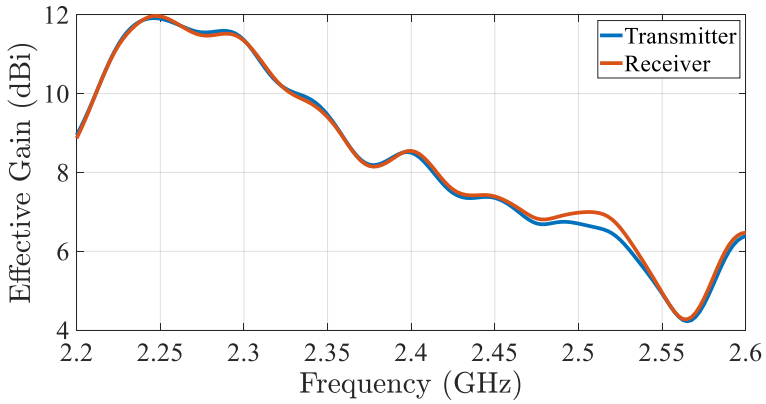

Figure 5.12: Measured gain for the transmitter and the receiver antennas using the impulse response. The PCB Yagi-Uda antennas were placed into the housings (see Fig. 5.9).

the transmitted power was lost either because of the conductor or flowed towards the absorbers. Therefore, only one quarter of the source power was captured by the receiver antenna. The reflection coefficient of the antenna ($\mid S_{11} \mid$) when only one of the pipe sections is simulated is presented in Fig. 5.10 and results show good agreement with the measured reflection coefficient. Due to the large EM simulation model required, the complete two-port system could not be fully simulated.

Additionally, the normalised impulse response ($h(t)$) of the system was measured (see Fig. 5.11). The time difference between the transmitted signal and the impulse response is 14.59 ns. The distance (d) between the transmitter and the receiver antenna is 3.8 m. Therefore the group velocity (υ_g) of the signal can be calculated, based on the expression $\upsilon_g = \frac{d}{\Delta t} = 2.605 \times 10^8$ m/s. It can be observed that the velocity of the system is between the group velocities of the TE_{21} and TE_{31} modes, based on Table 5.7. These results provide further justification that the dominant modes were indeed the TE_{21} and TE_{31} modes, as previously mentioned when reviewing the CST Studio Suite EM simulations. The wavelength (λ_g) of the propagated signal mode is 0.1575 m by inspection in Fig. 5.7, between the values of wavelengths of the TE_{21} and TE_{31} modes, 0.147 m, and 0.186 m, respectively. Using these results, the measured transmitter and receiver antenna effective gains into the housings are reported in Fig. 5.12, by (3.30) and (3.29) from 2.2 to 2.6 GHz. At 2.4 GHz, the measured transmit and receive gains were 8.5 dBi and 8.55 dBi, respectively.

5.5 Liquid Level Determination Testing

In this section, the experimental testing of the proposed system (see Fig. 5.1) is presented. Firstly, the exciting signals (Gaussian and rectangular pulses) and the reflectometry system are defined. Secondly, manual calibration is also described where the delay due to the electronics between the original and the reflected signals is determined and subtracted from the measurements. Also, experimental results for the proof-of-concept system are presented, particularly the reflected signal compared to the original. Both

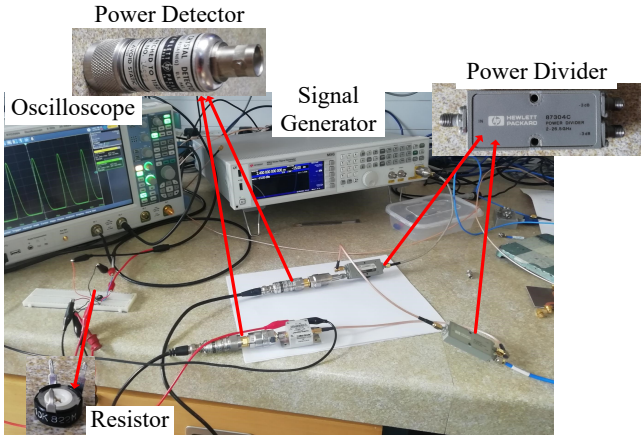

Figure 5.13: Bench-top photograph of the experimental setup for the reflectometry studies.

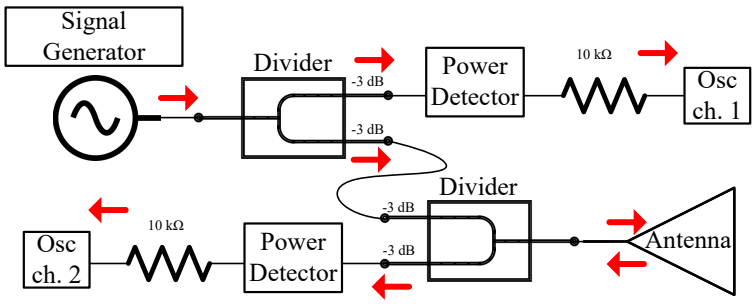

Figure 5.14: Schematic of the developed reflectometry system (circuits and instrumentation). The red arrows show the path of the power from the signal generator to the channels of the oscilloscope.

pulse types are examined, and the distance between the source and the liquid level is calculated. Following this, the measured reflection coefficient is illustrated, which helps understand the signal response and develop a link budget for more extended pipeline scenarios.

5.5.1 Excited Signals, Calibrations, & the Reflectometry System

The signals that are excited in this experiment are Gaussian and a rectangular pulse (see Fig. 5.17). The Gaussian pulse was described in Section 5.3, however, for this experimental case, the standard deviation (σ) was set to 0.3 and the mean of the distribution (μ) is 2 (see Fig. 5.17a Original Signal). The pulses were excited by the Keysight MXG N5183B Signal Generator (operating from 9 kHz to 6 GHz) at 2.4 GHz with a stimulating power of 15 dBm and 19 dBm for the Gaussian and rectangular pulses, respectively. The exciting source signals generated for the microwave reflectometry system were displayed on the Rohde & Schwarz RTO2064 oscilloscope in the time domain

and on the Keysight PXA Signal Analyzer N9030B Spectrum Analyzer in the frequency domain. The Rohde & Schwarz RTO2064 oscilloscope has a bandwidth from 600 MHz to 6 GHz, maximum sample rate 20 GSa/s. The Keysight PXA Signal Analyzer N9030B Spectrum Analyzer operating from DC to 50 GHz and the typical noise floor level at 2.4 GHz is -153 dBm.

It was shown that the PCB Yagi-Uda antenna is narrow-band when placed inside the mechanical housing (see Fig. 5.10). However, its performance from 2.35 to 2.45 suggests good matching, and especially around 2.4 GHz ($\mid S_{11} \mid < -20$ dB). Furthermore, the selected pulses are narrow-band as well. Additionally, any pulse radiated by an antenna is the time-derivative of the pulse applied to the antenna. The applied pulse may have DC content, e.g., a Gaussian pulse, but the radiated pulse does not have any DC content [81].

In Figs. 5.15 and 5.16 the Gaussian and the rectangular pulses for various spans are plotted. They show that the frequency bandwidth of the Gaussian pulse is from 2.3998 to 2.4002 GHz (see Fig. 5.15b); therefore, the total bandwidth is 400 kHz around the 2.4 GHz. In addition, the rectangular pulse has harmonics, with power over -40 dBm (the receiving sensitivity of the oscilloscope) from 2.36 to 2.44 GHz (see Fig. 5.16a). Also, the bandwidth of the main harmonic at 2.4 GHz is 200 kHz (see Fig. 5.16b). The reflected rectangular pulse is more likely to detect errors because of the strength of the harmonics over a greater bandwidth. The error estimate study is described in Subsection 5.5.2.

A high sampling rate was chosen because a high level of accuracy is required for capturing the time delay, which is of an order of ns. A lesser sampling rate recorder would be sufficient in a more realistic scenario, where the travelling time and distance measurements are greater. Also, an internal low pass (LP) digital signal processor (DSP) filter was used with a cut-off frequency of 100 kHz. This filter helped to extract the signals to a higher resolution while suppressing higher frequency noise. It should also be mentioned that the reflectometer is similar to the system described in [82] and [83], where it was used for heartbeat detection and respiration in humans.

As for the findings herein, the signal was excited by the aforementioned signal generator, then connected to a power divider (see Figs. 5.13 and 5.14). One output of the divider leads to a power detector and then to a resistor of 10 kΩ and finally to the oscilloscope. This signal is the original reference signal. The other output of the power divider leads to the same power divider, which receives the reflected signal at its input. Then, the signal is led to a power detector and eventually to the oscilloscope through the other output. This is the reflected signal.

The difference in time for these two signals (as they are displayed on the oscilloscope) is related to the relevant time delays for the signal to reach the liquid level and return. From this, the distance travelled by the signal can be calculated. The 87304C Hybrid Power Divider by Hewlett Packard was used. The power detector was a 423A Coaxial Crystal Detector also by Hewlett Packard (see Fig. 5.13).

It should be mentioned that many electronic sub-components and cables define the reflectometry system. These elements can cause undesired reflections and delays. For this reason, manual calibration was performed. For this calibration, the antenna was replaced by a short circuit component supplied by Keysight, and the delay between the original signal and the reflected signal was measured (Fig. 5.17). The absolute values of the reflected signal were plotted to provide a better characterisation of the delay from

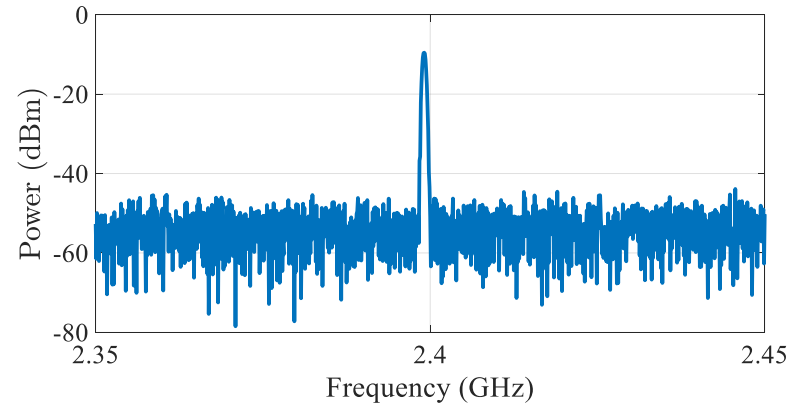

(a)

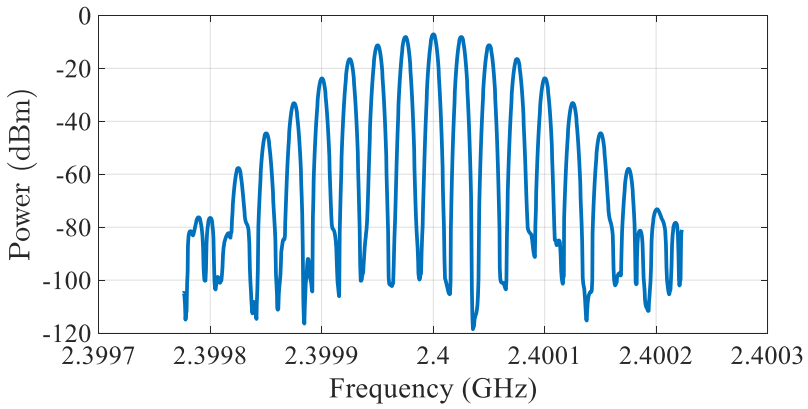

(b)

Figure 5.15: Measurements of the transmitted Gaussian signal in the frequency domain. Spans: (a) 2.35 to 2.45 GHz and (b) 2.3997 to 2.4003 GHz.

the original signal. From this calibration setup, the delay due to the electronics for the Gaussian pulse was observed to be around 0.9749 μs and for the rectangular pulse is around 0.9959 μs. The delay between the Gaussian pulses is defined by the difference between the peak value of the original and the reflected pulse. On the other hand, the delay between the rectangular pulses is defined by the difference between the last peak value of the original and the reflected pulse. In other words, it is compared to the time of the last samples which has the value of the flat top.

5.5.2 Experimental Results for Liquid Level Determination

The following results describe the liquid level determination using the proposed prototype system while considering the two different excited signals, i.e., the Gaussian and the rectangular pulses. As mentioned previously, a photograph of the experimental setup is shown in Fig. 5.1b. It also should be identified that the antenna in Fig. 5.1a leads to the reflectometry system as shown in Fig. 5.14.

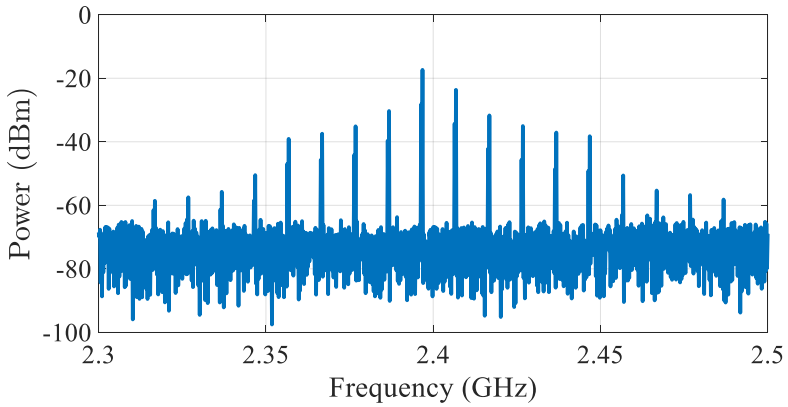

(a)

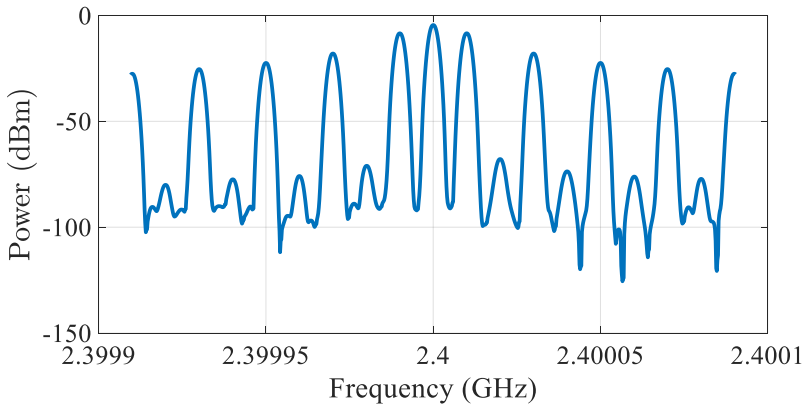

(b)

Figure 5.16: Measurements of the transmitted rectangular pulse signal in the frequency domain. Spans: (a) 2.3 to 2.4 GHz and (b) 2.3999 to 2.4001 GHz.

In this setup, the antenna receives the reflected signals from the electronics modules and the metallic parts of the pipework assembly, the mandrel, and the liquid-level interface. The reflections from the metallic parts of the antenna and the mandrel are very low power ($| S_{11} | \approx -10$ dB at 2.4 GHz) as Fig. 5.19a demonstrates. On the other hand, when the water is added at the bottom of the pipe, the reflection coefficient increases (-5.66 dB at 2.4 GHz) as in Fig. 5.19b.

The reflected signals and their propagation delays from the original reference signals are reported in Fig. 5.18 when water is considered at the bottom of the pipe. The delay for the Gaussian pulse was observed to be around 0.9891 μs and for the rectangular pulse is around 1.0099 μs. The delay was measured with the same procedure as it is described in Subsection 5.5.1.

These results must be corrected for the electronic delays recorded from the calibration above and thus subtracted from the measurements. Also, for improved comparison of the time delays (corrected and calibrated) for the transmitted and received signals, absolute values are plotted in Fig. 5.18. Therefore actual measurements suggest that

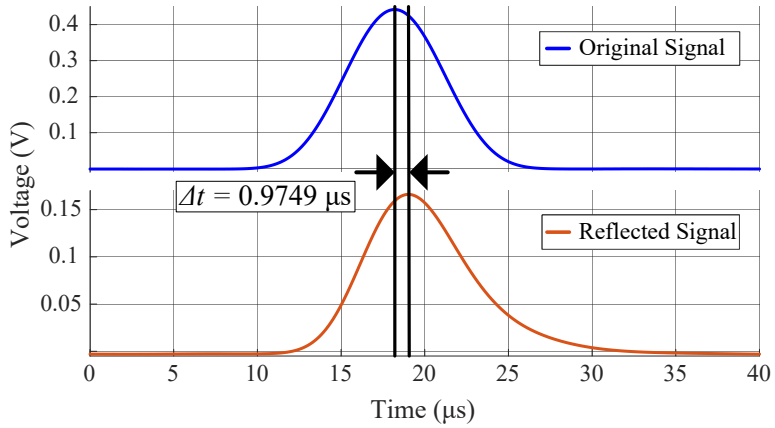

(a)

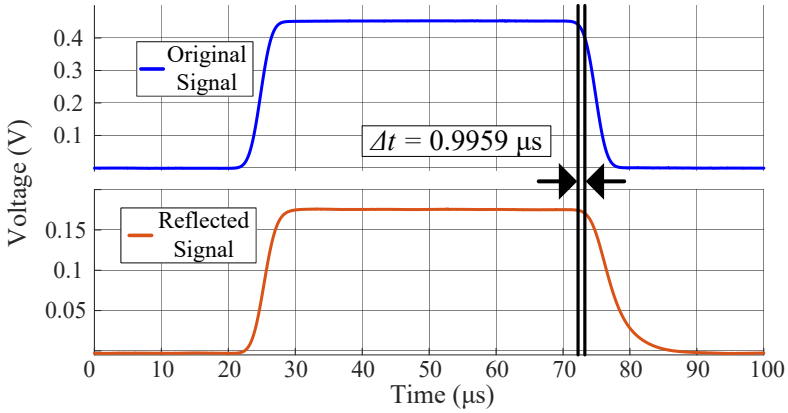

(b)

Figure 5.17: Measurements of the transmitted and reflected signals for the reflectometry system. The demonstrated delays are used for the calibration of the system. (a) Gaussian pulse and (b) Rectangular pulse.

the true delay of the reflected signal (forward and backward path) when water was positioned at the boundary of the pipe is approximately 14.2 ns for the Gaussian pulse and 14 ns for the rectangular pulse.

Also as it is described in Subsection 5.4.3, the extracted group velocity which was based on the experimental impulse response of the end-to-end system (see Fig. 5.9) was 2.605×10^8 m/s. Therefore the depth is calculated to be 1.84955 m and 1.8235 m based on the expression $d = \frac{v \times \Delta t}{2}$, for the Gaussian pulse and the rectangular pulse, respectively. However, the actual depth is 1.845 m, i.e., the physical distance from the antenna to the water level. The measured depth range error is 0.455 % and 2.55 % for the Gaussian and rectangular pulse, respectively. The depth range error seems to be less when the Gaussian pulse applies as the measurement is more accurate as the comparison occurs from peak to peak. On the other hand, the result is less accurate when the rectangular pulse is applied as it is more difficult to compare its rise or fall time.

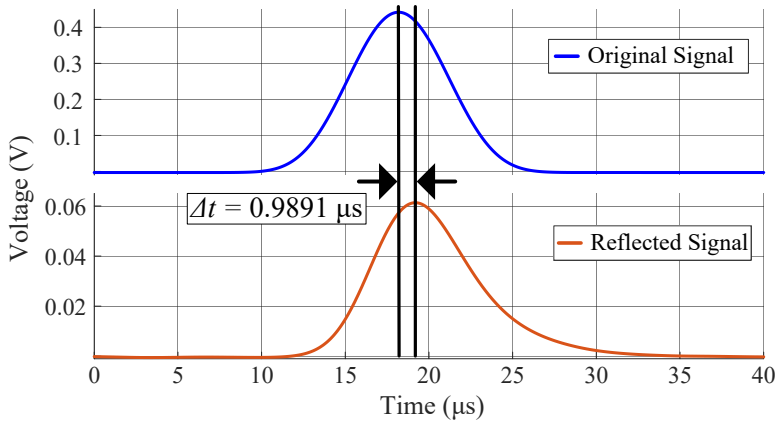

(a)

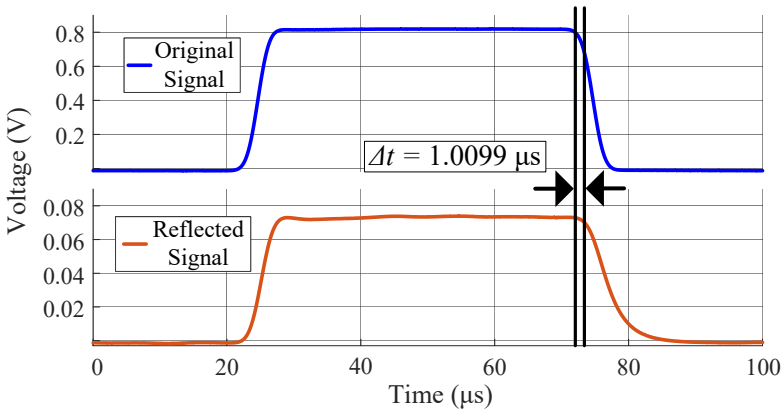

(b)

Figure 5.18: The transmitted and reflected signal measurements for the proposed system as is reported in Fig. 5.1a. (a) Gaussian pulse and (b) rectangular pulse.

5.5.3 Link Budget Analysis

Like standard telecommunication systems, a link budget can now be developed as all the relevant parameters have been defined and evaluated for the microwave liquid level determination system. The procedure can be described as follows.

The losses in the reflectometer are firstly calculated. Considering that the internal impedance of all the devices and the cables is 50 Ω, the peak voltage of the reflected Gaussian pulse is 0.0613 V. This make the total power of the signal to be given by $P_{Rx} = \frac{V_0^2}{Z_0} = \frac{0.0613^2}{50} = 0.075$ mW or -11.25 dBm. Additionally, the stimulated power was set to 15 dBm; therefore, the loss due to the reflectometer and the propagation (forward and back) into the pipe was 26.25 dB. The power loss due to the reflectometer is given when the reflection coefficient of the antenna (i.e., -5.66 dB at 2.4 GHz) is subtracted by the total system loss (26.25 dB). Thus the loss due to the reflectometer (L_{ref}) is 21.25 dB. As shown previously, the propagating signal is defined by a superposition of the TE_{21} and TE_{31} modes; therefore, the attenuation constant of the system can be assumed to be around 0.15 dB/m based on Table 5.7. Based on these parameters, a

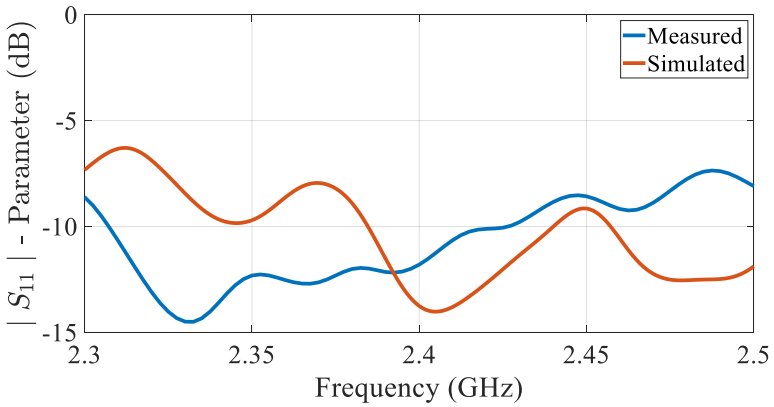

(a)

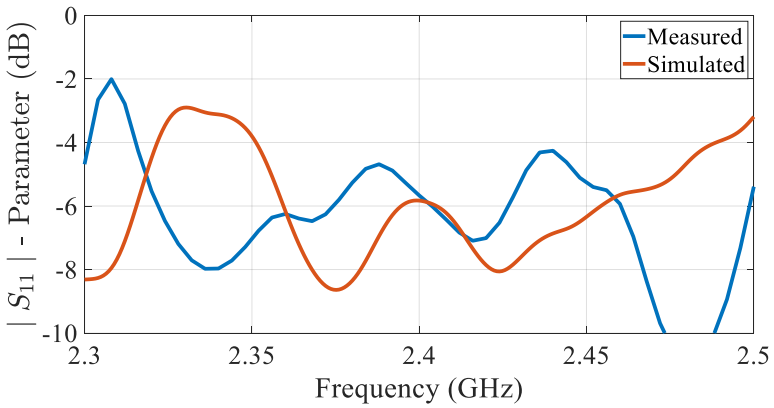

(b)

Figure 5.19: Reflection coefficient of the antenna the system as is reported in Fig. 5.1a, when (a) the bottom of the pipe is covered by microwave absorbers, and (b) a liquid layer of 5.5 cm is introduced at the bottom of the pipe.

general link budget equation can now be developed as follows,

$$\begin{aligned} P_{Rx}\,(\text{dBm}) \;\approx\; & P_{stim}\,(\text{dBm}) - \,||\, S_{11} \,||\, (\text{dB}) - L_{ref}\;(\text{dB}) \\ & -2 \times (d - 1.845) \times \alpha_c\,(\text{dB}). \end{aligned} \tag{5.28}$$

From the term $2 \times (d - 1.845) \times \alpha_c$, 1.845 m is necessary to be subtracted as it is already included into the parameter $|\, S_{11} \,|$. The minimum required stimulating power is -13 dBm. This is because the sensitivity of the oscilloscope was measured at around -40 dBm in the Heriot-Watt University RF/microwave lab.

The depth of interest required for liquid level determination is dependent on the prevailing subsurface pressure gradient. For example, on lower pressure wells, lift pumps are required to provide artificial assistance to produce the fluids, in which case the hydrostatic liquid level will be found relatively shallow in these scenarios, and a depth measurement range of 250 meters can provide helpful monitoring data. The proposed

application is also very relevant for monitoring the integrity of abandoned wells, where any abnormal rise of hydrostatic pressure may be measured above the cemented isolation barrier plugs, which are set relatively close to the surface. This is particularly relevant for the safe decommissioning of wells. Therefore, the valuable depth range can be much shallower than 250 meters which was considered to be a practical maximum depth for the initial experimental study [42].

Based on (5.28) estimations can now be completed for real pipelines whilst considering the attenuation constants as in Table 5.1. For example, for a stimulating power of 60 dBm (or 1 kW), theoretical depths for liquid level determination are about 250 meters. This considers the minimum received signal level to be -40 dBm which again is defined by the RTO2064 oscilloscope. For reducing this source power as future work can set the finding of a receiver with higher sensitivity than -40 dBm. Future work can also assess the impulse source power requirements while also increasing the receiver range sensitivity when designing a practical monitoring system. A more efficient system can motivations for future work by utilizing less transmit power and making use of equipment that can offer greater sensitivity levels than the -40 dBm for the oscilloscope which was employed for the laboratory experiments and concept study for proof-of-concept. The design basis for a dedicated reflectometer system can also be improved to overcome the 21.25 dB insertion losses for the developed connector-based system. This circuit system was useful but a more integrated circuit version would likely have fewer insertion losses. These future improvements can help to significantly decrease the impulse source power requirements whilst considering a maximum liquid determination depth of 250 meters.

5.6 Conclusion

As outlined in this chapter, there have not been any previous experimental studies to investigate the feasibility of liquid level determination within oil and gas pipelines by employing microwave carrier frequencies. In particular, the current research work in this chapter targeted the modeling and design of a microwave liquid level determination system, where the transceiver was placed into a metal pipe used for oil and gas well production to achieve liquid depth determination in real-time. The chapter examined the entire microwave measurement system, which included the electromagnetic background theory, the antenna design and its effective protective mechanism (i.e., radome), and the analysis to assess commercially available pipeline geometries. The numerical, simulation and experimental results demonstrated that the proof-of-concept system could work efficiently at 2.4 GHz (for a multi-mode scenario). Further supporting simulations were investigated at 400 MHz (considering unimodal operation).

Both scenarios are important to demonstrate alternate system feasibility. For the multi-mode scenario, the dominant propagating mode is a superposition of the TE_{21} and the TE_{31} modes, and this helped when developing the proposed link budget equation. These findings can be applied to similar pipeline systems and help define the maximum liquid level depth detected. As outlined in the chapter, the full depth ranges are limited by the attenuation constant of the metal casings, the transmit powers, the sensitivity of the receiver system, as well as the type of liquid mixtures contained within the pipe. Final experimental verification was made in the lab using a 4-meter long carbon steel

coaxial pipeline, and the propagation characteristics inside this test-bed arrangement were experimentally measured. The results were consistent with the numerical calculations and the supporting theory.

In the modelling, simulations, and measurements, the employed signals were Gaussian and rectangular pulses, while the following liquid types were considered: water, seawater, and oil. Also, commercially available RF components and simple microwave circuits were used to implement the reflectometry system. It should also be mentioned that future work can entail extending the pipeline length and studying different liquid mixtures and composition types. However, as fully reported in the chapter, the initial findings of the finite length pipe measurement setup (as developed for the lab test setting) fully demonstrated the feasibility and accuracy of the proposed microwave approach. Also, to the best knowledge of the author, no similar liquid level determination system has been reported previously with application to oil and gas well pipelines.

Chapter 6

Conclusions and Future Work

6.1 Conclusions

This thesis contributed to the oil and gas industry, particularly to the real-time sensory information collection and data exchange within pipelines as well as liquid level determination. Both studies were developed using microwave technologies, advanced waveguide theory, and antenna techniques. This scenario describes complex electromagnetic signal propagation within enclosed environments, such as pipes, tunnels, and mines, all of which, are not typical or well-researched engineering problems. In this concluding chapter, the key findings of the thesis are summarized. Then some potential improvements to the developed technologies and some future work are discussed.

6.1.1 Communications within Oil and Gas Well Pipelines

As documented in the literature, there has been a limited number of studies relating to electromagnetic propagation within the oil and gas well pipelines [8]-[17]. Despite these significant contributions, there have not been experiments and extensive studies which investigated the feasibility of communications within long pipelines considering microwave carrier frequencies. In particular, the current research work of this thesis targets the modelling and design of a communication system, where the antenna receiver and the transmitter are placed into a metallic pipe for oil and gas wells, mainly to deal with various problems such as real-time and continuous monitoring of the pipeline condition, the corrosion, possible gas leak detection, and other similar issues. The thesis also examined the entire system, including the complete electromagnetic environment, antenna integration, microwave analysis based on existing pipelines, the definition of wireless communication protocols, and the limitations of the developed systems in terms of power and SNR.

During the design of the transmission system, in summary, it was decided that the pipelines of the oil and gas well environment would be treated as a waveguide for the industry standard chosen radius (69.85 mm) and operational frequency at the ISM band. Since the pipeline characteristics, the dimensions, and the filling material were known, the modal analysis based on theory and the power analysis was also developed. Also, the conductor losses that exist because of the metallic walls were studied for two different materials, carbon steel 1010 and aluminium.

Firstly, some dipole transceivers were used in a one-meter aluminium pipeline, and parameters such as the TPL to estimate the propagating signal strength between them

(see Chapter 3). Additionally, the directivity of the dipoles and the effective gains when placed inside the pipeline were studied using the impulse response. Sensory data such as temperature and pressure were also successfully transmitted and monitored in real-time, using OFDM and software defined radios, i.e., USRPs at the transmitter and the receiver for a 2.5 GHz ISM band carrier frequency. Furthermore, a hot air blower was used to increase the air temperature around the sensor at the transmitter side. The system monitored the temperature changes accurately and provided an updated information display to the user. This lab-based feasibility study allowed for and led to a more efficient design, whilst considering a more realistic scenario, as presented in Chapter 4.

Secondly, a compact Yagi-Uda antenna was chosen and designed using microstrip technology for the transceiver. The antennas were placed inside the pipes and different pipeline configurations were extensively examined vis-a-vis simulations and measurements. The results showed that the setup could work efficiently at 2.4 GHz. The selected propagating mode is the TE_{11} mode, and the transmission path loss has been well defined in the thesis (see Chapter 4) for each propagation scenario, as well as the effective gain of the antennas. In addition, a link budget equation was developed, which can be applied to similar pipeline systems. An antenna housing was also built for the PCB Yagi-Uda antenna, allowing good system operation at 2.4 GHz and physical protection for the antenna. The propagating mode, in that case, is a superposition mainly of the TE_{11} mode and secondly of the TE_{21} mode. A TPL model for this propagation scenario was also developed, considering the effective gain of the antennas inside the housing.

All in all, a 36.03 m carbon steel circular pipe was set up in the field, and the propagation inside it was experimentally tested. Using OFDM as the communication protocol and commercial RF components, the results showed that the transmission of about 150 m is possible (shown when using attenuators, experimentally). Also, the receiving capability of all the developed systems was measured at -77 dBm in terms of power level and 15 dB in terms of the SNR demonstrating successful data communications.

6.1.2 Liquid Level Determination Method for Oil and Gas Pipelines

In Chapter 5, a different system for oil and gas wells was presented, basically, for liquid level determination at the bottom of the well reservoir with respect to the wellhead. As outlined, there have not been any previous experiments and studies which investigated the feasibility of liquid level determination within oil and gas pipelines considering microwave carrier frequencies. In particular, the research work of Chapter 5, targeted the modelling and design of a microwave liquid level determination system. The transceiver was placed into a metallic pipe for oil and gas well systems achieving liquid depth determination in real-time. Chapter 5 also examined the entire microwave system, which includes the electromagnetic background theory, the antenna design and its effective protective mechanism (i.e., radome), and an analysis considering commercially available pipelines. The numerical, simulation, and experimental results demonstrated that the proof-of-concept system could work efficiently at 2.4 GHz (for a multi-mode scenario). At the same time, supporting simulations were also investigated at 400 MHz (considering unimodal operation). Both frequency scenarios are essential to demonstrate system feasibility.

For the multi-mode scenario, the dominant propagating mode is a superposition of the TE_{21} and the TE_{31} modes, and this helped when developing the proposed link budget equation. These findings can be applied to similar pipeline systems and help define the maximum liquid level depth detected. As outlined in the chapter, depths are limited by the attenuation constant of the metal, the transmit powers, the sensitivity of the receiver system, and the type of liquid at the bottom of the pipe. All in all, a 4-meter carbon steel coaxial pipe was set up in the lab, and the propagation inside it was experimentally tested. Results were consistent with numerical calculations and the supporting theory.

In the modeling, simulations, and measurements, the employed signals were Gaussian and rectangular pulses, while the following liquid types were considered: water, seawater, and oil. Also, commercially available RF components and simple microwave circuits were used to implement the reflectometry system. However, as fully reported in Chapter 5, initial findings of the finite length pipe measurement setup (as developed in the lab setting) fully demonstrated the feasibility and accuracy of the proposed microwave approach.

6.2 Future Work

This section introduces improvements over the existing techniques, which can be studied in future research and engineering activities.

6.2.1 Communications within Oil and Gas Well Pipelines

In Chapter 4, it was shown that the transmission of about 150 m is possible when using attenuators. Further experimental testing by considering carbon steel pipelines, and significantly increasing the transmission ranges, are planned as future work. Also, repeaters may be required when transmitting over long ranges depending on the possible transmit powers and system implementation and any observed conductor and transmission losses within practical pipelines. The selection of a lower frequency, e.g., 900 MHz, may be helpful for propagation over long ranges (due to the lower attenuation rates), and it would be interesting to study such a system with that carrier frequency, or possibly, a dual-frequency system. These will require the re-design of the antennas, RF components, and transceivers.

The housing on the top of the mandrel has some margins of improvement from its mechanical and RF points-of-view.

For example, in terms of making the antenna housing more compact; i.e. shorter. This is because existing designs are more than 1 meter in length Also, the antenna housing could be re-designed into a PCB version that couples power into the pipeline. This is because the function of the antenna housing cover is basically to act like a directional coupler [32]. However, more conventional couplers work on uni-modal propagation, and since the pipeline is likely to be a multi-mode system, clever and new design approaches would be needed. A more robust design for the mandrel can be the primary target for future work.

Other research and development activities include a more established workable prototype system for both the inner core and which includes the needed electronics and antenna within one PCB. A good next step would be to combine all components onto

one board and not have a connectorized system. In addition, future goals can be to develop a more robust system that includes two transmitters and two receivers for propagation into the inner and outer pipes simultaneously. Also, the developed OFDM coding for the existing pipeline system would help to implement the new two-by-two transceiver system. Also, additional modulation schemes could be adopted or multiple-input multiple-output (MIMO) principles could be adopted to improve the system performances in terms of SNR, modal control, and signal directivity.

A compact Yagi-Uda antenna was chosen for the transceiver, and placed into the radome. An alternative option could be using a substrate integrated waveguide (SIW) antenna and this could also be integrated with the required coupling functions of the antenna and its housing configuration. This SIW coupler feeding system would help in the injection of the power into the inner core and the annulus region, at the same time making the system more robust without the use of mechanical housing.

6.2.2 Liquid Level Determination Method for Oil and Gas Pipelines

Much of the future work discusses how the communications within oil and gas well pipelines apply to the liquid level determination method. For example, future work can better extend the pipeline length to understand the maximum possible propagation range. Also, implementing a frequency, e.g., 400 MHz, where only the TEM mode is excited by the source is set as a future goal. Moreover, a more robust design for the mandrel could help improve the performance of the system. Also, employing different pulse types might be of interest, or, adopting more radar type signals such as frequency modulated continuous waveform (FMCW) signals. Studying different liquid types is also essential as well to test the system further. Essentially the well flow conditions can contain other particulates and some multi-phase mixtures (combinations of gas, oil, and seawater) which also need to be assessed. Furthermore, the reflectometry system can be improved and made more robust into a single printed circuit form, and this would help to reduce the losses of this circuit system.

Appendix A

List of Publications

This appendix includes a list of the research papers that have been published or are under review during the Ph.D. project.

A.1 Journal Papers

1. **K. Kossenas**, S. K. Podilchak and M. Beveridge, "Wireless Propagation in a Metallic Pipe for the Transmission of Sensory Oil and Gas Well Data," in IEEE Antennas and Wireless Propagation Letters, vol. 21, no. 6, pp. 1124-1128, June 2022 (accepted, to appear).

2. **K. Kossenas**, S. K. Podilchak and M. Beveridge, "Antenna Generated Controlled Propagation for Communications within Oil and Gas Well Pipelines," in IEEE Transactions on Antennas and Propagation, 2022 (under review).

3. **K. Kossenas**, S. K. Podilchak and M. Beveridge, "A Microwave Liquid Level Determination Method for Oil and Gas Pipelines," in IEEE Access, vol. 10, pp. 67031-67046, 2022 (accepted, to appear).

4. * **K. Kossenas** et al., "A Methodology for Remote Microwave Sterilization Applicable to the Coronavirus and Other Pathogens Using Retrodirective Antenna Arrays," in IEEE Journal of Electromagnetics, RF and Microwaves in Medicine and Biology, vol. 6, no. 1, pp. 41-51, March 2022.

A.2 Conference Papers

First Author

1. **K. Kossenas**, S. K. Podilchak and M. Beveridge, "RF System Development for Sensor and Wireless Communication Applications Inside a Circular Pipe," 2020 IEEE International Symposium on Antennas and Propagation and North American Radio Science Meeting, 2020, pp. 1143-1144.

2. * **K. Kossenas**, D. Comite, S. N. Daskalakis, P. Kontou, M. Kuznetcov, and S. K. Podilchak, "A Remote Microwave Thermal Sterilization Approach for the Coronavirus and Other Pathogens by Wireless Power Transmission," URSI GASS 2021,

August-September 2021, Rome, Italy **(URSI GASS 2021 Young Scientist Award)**.

3. * **K. Kossenas**, M. V. Kuznetcov, D. Comite and S. K. Podilchak, "Remote Destruction of the Coronavirus by Dual-Polarized Wireless Power Transmission," 2021 IEEE International Symposium on Antennas and Propagation and USNC-URSI Radio Science Meeting (APS/URSI), 2021, pp. 459-460. **(Honorable Mention in the AP-S Student Paper Competition)**

Co-Author

4. * M. V. Kuznetcov, **K. Kossenas** et al. "Remote Microwave Sterilization Applicable to Coronavirus Using a Van-Atta Retrodirective Antenna Array with 2-D Tracking Capability," 2021 51st European Microwave Conference (EuMC), April 2022, London, United Kingdom.

*The marked publications regard the development of RF systems for achieving remote microwave sterilization of the coronavirus. This project was undertaken in parallel with the presented works of this thesis on oil gas well RF systems, due to the importance of the sterilization work which helped to circumvent the pandemic. Despite the extended research, the findings, and the techniques that were developed for the oil and gas systems were also used in the microwave remote sterilization project, but the internal committee of the University of Edinburgh recommended that these papers not be included in the thesis dissertation. The main reason was the minor connection, from an application point-of-view, between the sterilization work itself, and the antenna/microwave engineering and electromagnetic systems work. For these main reasons, these papers are not discussed in this dissertation.

Bibliography

[1] M. Yusif and M. Babayev, "A brief history of oil and gas well drilling," *Visions of Azerbaijan*, January - February 2012. [Online]. Available: http://www.visions.az/en/news/366/4ca556e3/.

[2] F. M. Jonathan Craig Francesco Gerali and R. Sorkhabi, "The history of the european oil and gas industry (1600s–2000s)," Geological Society, Ed., 21 June 2018. [Online]. Available: https://sp.lyellcollection.org/content/465/1/1.1.

[3] G. D. Mitchell, "Chapter 6 - direct coal liquefaction," in *Applied Coal Petrology*, I. Suárez-Ruiz and J. C. Crelling, Eds., Burlington: Elsevier, 2008, pp. 145–171, ISBN: 978-0-08-045051-3. DOI: https://doi.org/10.1016/B978-0-08-045051-3.00006-3. [Online]. Available: https://www.sciencedirect.com/science/article/pii/B9780080450513000063.

[4] A. Jarrot, A. Gelman, and J. Kusuma, "Wireless digital communication technologies for drilling: Communication in the Bits's Regime," *IEEE Signal Processing Magazine*, vol. 35, no. 2, pp. 112–120, 2018.

[5] B. Elbert, *The Satellite Communication Applications Handbook*, ser. Artech House space technology and applications library. Artech House, 2004. [Online]. Available: https://books.google.co.uk/books?id=D9k5s2-mMKgC.

[6] N. G. Franconi, A. P. Bunger, E. Sejdić, and M. H. Mickle, *Wireless Communication in Oil and Gas Wells*, E. Technology, Ed. 2014-10-24, ch. Chapter 12, 996–1005.

[7] C. C. Rodd, "The application of fluid level measurements to oil wells in kansas," Professional Degree Thesis, Dept. Mechanical, Aerospace Engineering Missouri School of Mines, and Metallurgy, KC, USA, 1940.

[8] M. Aalsalem, W. Khan, W. Gharibi, K. Khan, and Q. Arshad, "Wireless sensor networks in oil and gas industry: Recent advances, taxonomy, requirements, and open challenges," *Journal of Network and Computer Applications*, vol. 113, Apr. 2018. DOI: 10.1016/j.jnca.2018.04.004.

[9] K. T. Erickson, A. Miller, E. K. Stanek, C. Wu, and S. Dunn-Norman, "Pipelines as communication network links," Rolla Missouri University of North Texas Libraries Digital Library, Tech. Rep., March 14, 2005.

[10] Z Wang, T. Li, D McCormack, and M. Mintchev, "Wireless data transmission options in rotary in-drilling alignment (r-ida) setups for multilateral oil drilling applications," *International Journal of Information Theories and Applications*, vol. 21, pp. 154–164, Jun. 2014.

[11] E. Zhang and A. Abdi, "Communication rate increase in drill strings of oil and gas wells using multiple actuators," *Sensors (Basel)*, vol. 113, Mar. 2019. DOI: 10.1016/j.jnca.2018.04.004.

[12] N. Franconi, A. Bunger, E. Sejdic, and M. Mickle, "Wireless communication in oil and gas wells," *Energy Technology*, vol. 2, Oct. 2014. DOI: 10.1002/ente.201402067.

[13] A. Jarrot, A. Gelman, and J. Kusuma, "Wireless digital communication technologies for drilling: Communication in the bitss regime," *IEEE Signal Processing Magazine*, vol. 35, no. 2, pp. 112–120, 2018.

[14] K. A. Colati, G. P. Dalmaschio, E. V. de Castro, A. O. Gomes, B. G. Vaz, and W. Romão, "Monitoring the liquid/liquid extraction of naphthenic acids in brazilian crude oil using electrospray ionization FT-ICR mass spectrometry (ESI FT-ICR MS)," *Fuel*, vol. 108, pp. 647–655, 2013, ISSN: 0016-2361.

[15] G. T. Polley, D. I. Wilson, S. J. Pugh, and E. Petitjean, "Extraction of crude oil fouling model parameters from plant exchanger monitoring," *Heat Transfer Engineering*, vol. 28, no. 3, pp. 185–192, 2007.

[16] D. K. Ferguson, C. Li, C. Jiang, A. Chakraborty, S. E. Grasby, and C. R. Hubert, "Natural attenuation of spilled crude oil by cold-adapted soil bacterial communities at a decommissioned high arctic oil well site," *Science of The Total Environment*, vol. 722, p. 137 258, 2020, ISSN: 0048-9697.

[17] A. Akinyemi, M. Sun, and A. Gray, "Data integration for offshore decommissioning waste management," *Automation in Construction*, vol. 109, p. 103 010, 2020, ISSN: 0926-5805.

[18] C. Rodd, *The Application of Fluid Level Measurements to Oil Wells in Kansas*. University of Missouri, School of Mines and Metallurgy, 1940. [Online]. Available: https://books.google.co.uk/books?id=pld5nQEACAAJ.

[19] J. Godbey and C. Dimon, *The Automatic Liquid Level Monitor for Pumping Wells*. 1977, vol. 29, pp. 1019–1024.

[20] K. Thomas, *A Review of the Acoustic Determination of Liquid Levels in Gas Wells*. 1968, vol. 20, pp. 784–785.

[21] V Bhargava, A Sethi, S Singh, and I Chellani, "A case study-determination of accurate liquid level and its applications in cbm wells," in *SPE Oil & Gas India Conference and Exhibition*, OnePetro, 2015.

[22] *Acoustic Liquid Level Testing of Gas Wells*, vol. All Days, SPE Oklahoma City Oil and Gas Symposium / Production and Operations Symposium, Apr. 2009.

[23] R. Andsager and R. Knapp, "Acoustic Determination of Liquid Levels in Gas Wells," *Journal of Petroleum Technology*, vol. 19, no. 05, pp. 601–605, May 1967.

[24] J. Shinyakov, M. Sukhorukov, D. Torgaeva, A. Soldatov, N. Shalyapina, and D. Li, "Analysis of methods for measuring the liquid level in the annular space of an oil well," *MATEC Web of Conferences*, vol. 158, p. 01 029, Jan. 2018. DOI: 10.1051/matecconf/201815801029.

[25] W. Zhou, J. Liu, and L. Gan, "Dynamic liquid level detection method based on resonant frequency difference for oil wells," *Turkish Journal of Electrical Engineering ans Computer Sciences*, vol. 26, pp. 2968–2976, Nov. 2018.

[26] X. Zhang, J. Fan, S. Wu, and D. Liu, "A novel acoustic liquid level determination method for coal seam gas wells based on autocorrelation analysis," *Energies*, vol. 10, p. 1961, Nov. 2017. DOI: 10.3390/en10121961.

[27] H. Yanbin, G. Xianwen, W. Mingshun, L. Xiangyu, L. Yu, and W. Bing, "Application of dynamic liquid level prediction model based on improved svr in sucker rod pump oil wells," in *Proceedings of the 32nd Chinese Control Conference*, 2013, pp. 7826–7830.

[28] A. Podio and J. McCoy, *Acoustic Fluid Level Measurements in Oil and Gas Wells Handbook*. University of Texas at Austin, Petroleum Extension (PETEX), 2017. [Online]. Available: https://books.google.co.uk/books?id=NKOZAQAACAAJ.

[29] G. Peng, J. He, S. Yang, and W. Zhou, "Application of the fiber-optic distributed temperature sensing for monitoring the liquid level of producing oil wells," *Measurement*, vol. 58, pp. 130–137, 2014, ISSN: 0263-2241.

[30] H. Zhang, W. Fu, C. Wang, G. Zhang, and Z. Wang, "Real-time monitoring of oil-well dynamic liquid-level based on optical fiber sensing," *AIP Conference Proceedings*, vol. 1839, no. 1, p. 020 076, 2017. DOI: 10.1063/1.4982441.

[31] H. Devold, "Oil and gas production handbook: An introduction to oil and gas production, transport, refining and petrochemical industry."

[32] D. M. Pozar, "Microwave engineering," in New Jersey, NJ: John Wiley & Sons, Inc., 2012, ch. 1-3.

[33] K. Kossenas, S. K. Podilchak, D. Comite, P. D. H. Re, G. Goussetis, S. K. Pavuluri, S. J. Griffiths, R. J. Chadwick, C. Guo, N. Bruns, C. Tait-Burkard, J. G. Haas, and M. P. Desmulliez, "A methodology for remote microwave sterilization applicable to the coronavirus and other pathogens using retrodirective antenna arrays," *IEEE Journal of Electromagnetics, RF and Microwaves in Medicine and Biology*, vol. 6, no. 1, pp. 41–51, 2022. DOI: 10.1109/JERM.2021.3077110.

[34] K. Kossenas, M. V. Kuznetcov, D. Comite, and S. K. Podilchak, "Remote destruction of the coronavirus by dual-polarized wireless power transmission," in *2021 IEEE International Symposium on Antennas and Propagation and USNC-URSI Radio Science Meeting (APS/URSI)*, 2021, pp. 459–460. DOI: 10.1109/APS/URSI47566.2021.9704048.

[35] K. Kossenas, D. Comite, S. N. Daskalakis, P. Kontou, M. V. Kuznetcov, and S. K. Podilchak, "A remote microwave thermal sterilization approach for the coronavirus and other pathogens by wireless power transmission," in *URSI GASS 2021*, 2021.

[36] "Hazardous area classification and control of ignition sources," Health and Safety Executive, Tech. Rep., 2004. [Online]. Available: https://www.hse.gov.uk/comah/sragtech/techmeasareaclas.htm.

[37] S. Mochizuki, "RF technology for ejx/yta series wireless transmitters in hazardous areas," Yokogawa, Tech. Rep., 2013. [Online]. Available: https://www.yokogawa.com/ca/library/resources/yokogawa-technical-reports/rf-technology-for-ejx-yta-series-wireless-transmitters-in-hazardous-areas/.

[38] I. Verhappen, "How to ensure intrinsic safety for wireless systems," PROFIBUS & PROFINET International), Tech. Rep., 2019. [Online]. Available: https://www.controlglobal.com/articles/2019/how-to-ensure-intrinsic-safety-for-wireless-systems/.

[39] "Hazardous area classifications and protections," Emerson Automation Solutions, Tech. Rep., 2019.

[40] H. Uhlig, J. Kirkwood, and F. Keyes, "The dependence of the dielectric constants of gases on temperature and density," *J.Chem.Phys.*, vol. 1, pp. 155–159, 1933.

[41] C. L. Holloway, D. A. Hill, R. A. Dalke, and G. A. Hufford, "Radio wave propagation characteristics in lossy circular waveguides such as tunnels, mine shafts, and boreholes," *IEEE Transactions on Antennas and Propagation*, vol. 48, no. 9, pp. 1354–1366, 2000. DOI: 10.1109/8.898768.

[42] D. Joinson, Senior Production Technologist for Shell Amsterdam, Private communication, August 2020.

[43] V. Gómez-Guillamón Buendía, S. K. Podilchak, G. Goussetis, D. Masotti, A. Costanzo, and P. Nicole, "A smart cable offering selective and distributed antenna radiation using RF switches and non-conventional hybrid couplers," *IEEE Transactions on Antennas and Propagation*, vol. 66, no. 11, pp. 6346–6351, 2018. DOI: 10.1109/TAP.2018.2863753.

[44] A. Malone and C. Sarris, ""electromagnetic vision": Machine intelligence models of radiowave propagation in tunnels," Jul. 2018, pp. 557–558. DOI: 10.1109/APUSNCURSINRSM.2018.8608893.

[45] S. Palit, S. Bickerstaff, and C. Langmaid, "Design of wireless communication sensing networks for tunnels, trains and buildings," 2009.

[46] X. Zhang, N. Sood, and C. D. Sarris, "Fast radio-wave propagation modeling in tunnels with a hybrid vector parabolic equation/waveguide mode theory method," *IEEE Transactions on Antennas and Propagation*, vol. 66, no. 12, pp. 6540–6551, 2018. DOI: 10.1109/TAP.2018.2864344.

[47] X. Zhang and C. D. Sarris, "Statistical modeling of electromagnetic wave propagation in tunnels with rough walls using the vector parabolic equation method," *IEEE Transactions on Antennas and Propagation*, vol. 67, no. 4, pp. 2645–2654, 2019. DOI: 10.1109/TAP.2019.2894285.

[48] N. Sood, S. Baroudi, X. Zhang, J. Liebeherr, and C. D. Sarris, "Integrating physics-based wireless propagation models and network protocol design for train communication systems," *IEEE Transactions on Antennas and Propagation*, vol. 66, no. 12, pp. 6635–6645, 2018. DOI: 10.1109/TAP.2018.2876649.

[49] X. Zhang, N. Sood, J. K. Siu, and C. D. Sarris, "A hybrid ray-tracing/vector parabolic equation method for propagation modeling in train communication channels," *IEEE Transactions on Antennas and Propagation*, vol. 64, no. 5, pp. 1840–1849, 2016. DOI: 10.1109/TAP.2016.2535125.

[50] Q. P. Soo, S. Y. Lim, and D. W. Gin Lim, "Investigation of rough surfaces for propagation modeling in caves," in *2018 IEEE International Symposium on Antennas and Propagation USNC/URSI National Radio Science Meeting*, 2018, pp. 555–556. DOI: 10.1109/APUSNCURSINRSM.2018.8609186.

[51] J. G. Speight, "Chapter 4 - reservoir fluids, in introduction to enhanced recovery methods for heavy oil and tar sands," in Laramie, Wyoming, USA: Gulf Professional Publishing, 2016.

[52] J. Fleming, *The Principles of Electric Wave Telegraphy and Telephony*. Longmans, Green, 1919, p. 364. [Online]. Available: https://books.google.co.uk/books?id=xHNBAAAAIAAJ.

[53] R. Graf, *Modern Dictionary of Electronics*, ser. Electronics & Electrical. Elsevier Science, 1999, p. 29. [Online]. Available: https://books.google.co.uk/books?id=uah1PkxWeKYC.

[54] A. J. (CET), "A diplexer and associated waveguides in an air traffic control radar," https://commons.wikimedia.org/wiki/File:Diplexer1.jpg.

[55] AZoOptics. (2014). "Waveguide - definition and applications."

[56] N. Marcuvitz, "Waveguide handbook," in Massachusetts Institute of Technology: Dover Publications Inc., 1965, ch. 2.

[57] P. Massoud Salehi and J. Proakis, *Digital Communications*. McGraw-Hill Education, 2007, ISBN: 9780072957167. [Online]. Available: https://books.google.co.uk/books?id=HroiQAAACAAJ.

[58] S. B. Weinstein, "The history of orthogonal frequency-division multiplexing [history of communications]," *IEEE Communications Magazine*, vol. 47, 2009.

[59] C. Balanis, "Antenna theory: Analysis and design," in Wiley, 2015, ch. 4.

[60] B. Scheers, A. Marc, and A. Vander Vorst, "Time-domain simulation and characterisation of tem horns using a normalised impulse response," *Microwaves, Antennas and Propagation, IEEE Proceedings*, vol. 147, pp. 463 –468, Jan. 2001. DOI: 10.1049/ip-map:20000708.

[61] L. Bowen, E. Farr, and W. Prather, "Fabrication and testing of two collapsible impulse radiating antennas," *Sensor and Simulation Notes*, note 440, Jan. 1999.

[62] M. Kielmas, "The types of metals used in the oil & gas industry." [Online]. Available: https://smallbusiness.chron.com/industry-information-industrial-diamonds-74997.html.

[63] G. Forbes, S. Massie, and S. Craw, "Wifi-based human activity recognition using raspberry pi.," M. Alamaniotis and S. Pan, Eds., Institute of Electrical and Electronics Engineers, 2020, pp. 722–730. [Online]. Available: https://rgu-repository.worktribe.com/output/966777.

[64] B. Lathi, *Modern Digital and Analog Communication Systems*, ser. Oxford series in electrical engineering. Oxford University Press, 1995, ISBN: 9780195105001.

[65] AZoM, "AISI 1010 Carbon Steel (UNS G10100)," Sep 21 2012.

[66] E. ToolBox, "Permeability," 2016.

[67] Mat Web, "Aisi 1010 steel, cold drawn," Material Property Data.

[68] R. M. Cornell and U. Schwertmann, *The iron oxides: structure, properties, reactions, occurrences and uses*. John Wiley & Sons, 2003.

[69] G. S. Parkinson, "Iron oxide surfaces," *Surface Science Reports*, vol. 71, no. 1, pp. 272–365, 2016, ISSN: 0167-5729.

[70] M. Wahib, A. Freundorfer, and Y. Antar, "A planar wideband quasi-yagi antenna with high gain and ftbr," in *2017 International Workshop on Antenna Technology: Small Antennas, Innovative Structures, and Applications (iWAT)*, 2017, pp. 42–45.

[71] S. K. Podilchak, M. Caillet, D. Lee, Y. M. M. Antar, L. C. Chu, J. Cain, M. Hammar, D. Caldwell, and E. Barron, "A compact circularly polarized antenna using an array of folded-shorted patches," *IEEE Transactions on Antennas and Propagation*, vol. 61, no. 9, pp. 4861–4867, 2013.

[72] Y. Li, S. K. Podilchak, D. E. Anagnostou, C. Constantinides, and T. Walkinshaw, "Compact antenna for picosatellites using a meandered folded-shorted patch array," *IEEE Antennas and Wireless Propagation Letters*, vol. 19, no. 3, pp. 477–481, 2020.

[73] *Maritime monitoring and messaging microsatellite (M3MSat) mission*, https://www.asc-csa.gc.ca/eng/satellites/m3msat/default.asp, Accessed: 2021-10-20.

[74] A. Podio and J. McCoy, *Acoustic Fluid Level Measurements in Oil and Gas Wells Handbook*. University of Texas at Austin, Petroleum Extension (PETEX), 2017. [Online]. Available: https://books.google.co.uk/books?id=NKOZAQAACAAJ.

[75] C. Xu, I. Ben-Zvi, H. Wang, T. Xin, and L. Xiao, "A new concept for high power rf coupling between waveguides and resonant rf cavities," *Progress In Electromagnetics Research B*, vol. 75, pp. 59–77, Jan. 2017. DOI: 10.2528/PIERB17022604.

[76] G. Squires and S. L, *Practical Physics*. Cambridge University Press, 2001. [Online]. Available: https://books.google.co.uk/books?id=vrNIj4re3-wC.

[77] U. Kaatze, "Complex permittivity of water as a function of frequency and temperature," *Journal of Chemical & Engineering Data*, vol. 34, no. 4, pp. 371–374, 1989. DOI: 10.1021/je00058a001.

[78] S. Zainud-Deen, H. Malhat, and M. Mohamed, "Reconfigurable sea-water based reflectarray antenna for uhf applications," *Wireless Personal Communications*, vol. 106, Jun. 2019. DOI: 10.1007/s11277-019-06235-y.

[79] T. Meissner and F. Wentz, "The complex dielectric constant of pure and sea water from microwave satellite observations," *IEEE Transactions on Geoscience and Remote Sensing*, vol. 42, no. 9, pp. 1836–1849, 2004. DOI: 10.1109/TGRS.2004.831888.

[80] "User's Manual of CST Microwave Studio 2020," 2020.

[81] W. Wiesbeck, G. Adamiuk, and C. Sturm, "Basic properties and design principles of uwb antennas," *Proceedings of the IEEE*, vol. 97, no. 2, pp. 372–385, 2009. DOI: 10.1109/JPROC.2008.2008838.

[82] P. Kontou, S. Ben Smida, S. Nektarios Daskalakis, S. Nikolaou, M. Dragone, and D. E. Anagnostou, "Heartbeat and respiration detection using a low complexity cw radar system," in *2020 50th European Microwave Conference (EuMC)*, 2021, pp. 929–932. DOI: 10.23919/EuMC48046.2021.9338223.

[83] P. Kontou, S. Ben Smida, M. Dragone, S. Nikolaou, and D. E. Anagnostou, "CW radar based system with automated dc offset reduction for heartbeat detection," in *2020 IEEE USNC-CNC-URSI North American Radio Science Meeting (Joint with AP-S Symposium)*, 2020, pp. 73–74. DOI: 10.23919/USNC/URSI49741.2020.9321670.